Vessel Motion Sensing

with Absolute Reference Measurement

S. ten Pas

Master of Science Thesis - Department of Precision and Microsystems Engineering

WWW.CAMPELMANN.NL

CONFIDENTIAL

Vessel Motion Sensing

with Absolute Reference Measurement

by

S. ten Pas

to obtain the degree of Master of Science
at the Delft University of Technology,
to be defended publicly on Tuesday May 9, 2017 at 13:00hr.

Student number:	1395904	
Project duration:	March 15, 2016 – May 9, 2017	
Thesis committee:	Prof. dr. ir. J. L. Herder,	TU Delft, Chair Examining Committee
	Ir. J. W. Spronck,	TU Delft, MSc-Thesis Advisor & Daily Supervisor
	dr. ir. B. A. J. Lenseigne	TU Delft, External Board Member
	Ir. J. W. de Vriend,	Ampelman Operations B.V., Daily Supervisor
	Ir. A. G. Verweij,	Ampelman Operations B.V., Daily Supervisor

This thesis is confidential and cannot be made public until May 9, 2022.

An electronic version of this thesis is available at `http://repository.tudelft.nl/`.

TU Delft

The work in this thesis was supported by Ampelmann Operations BV. Their cooperation is hereby gratefully acknowledged.

Copyright © Precision and Microsystems Engineering (PME)
All rights reserved.

Abstract

Offshore structures, like windmills and oil or gas platforms, require regular maintenance and operators to continue working. Rough seas and weather conditions caused a problem to get people on and off these offshore structures until in 2009 Ampelmann came with a solution to safely transfer people offshore. This people transfer is done by means of a motion compensating platform and gangway. With the Ampelmann solution workers are able to safely access these offshore platforms, even in rough weather and sea conditions.

The vessel motions must be known to allow compensation. Currently the vessel motions are measured by Ampelmann using a highly accurate and expensive fibre optic gyroscope called a Motion Reference Unit (MRU). The MRU measures translational change in velocity by means of accelerations and rotational change in position by means of angular velocity. These changes are used to determine the position and orientation of the vessel in six Degrees of Freedom (DoF). Using a rate of change measurement system to measure position and orientation is known to introduce drift. Over time this drift influence will grow and the position and orientation of the vessel with respect to the target platform becomes inaccurate.

A new vessel motion measurement system is introduced called the LiDAR Reference Unit (LRU), with Light Detection And Ranging (LiDAR). The LRU overcomes the drift problems by measuring the position of the offshore target with respect to the vessel. The LRU combines measurement information from multiple sensors to create a robust, accurate and cheaper solution. The system combines a scanning Laser Range Finder (LRF) and a micro-electromechanical Inertial Measurement Unit (IMU).

To determine the vessel motions, the position of the target platform is measured and followed in every consecutive LRF scan. Obstructions caused by moving people or small details on the target platform create measurement scan point outliers. These outliers could cause mismatching of LRF scan point clouds. To avoid mismatching a landmark detection algorithm is used. Common shapes on platforms are circles and straight lines. A RANdom SAmple Consesnsus (RANSAC) algorithm is used to extract lines and arcs from the LRF scan point cloud. Only the scan points of the arcs and lines are used to measure the vessel position and orientation to the target platform. The position and orientation are determined using an Iterative Closest Point (ICP) matching algorithm. The sensor measurement data of the LRF and IMU are combined with a model based Kalman filter.

The feasibility of the proposed LRU is tested with a simulation model for the system. To verify the results of the simulation model and determine the accuracy of the LRU a test setup is created. Simulated vessel motions are used to move the measurement system. The LRF scans the target platform and the measured results are compared to the position data of the measurement setup. The robustness of the motion extraction algorithm is tested by creating an obstruction of a person walking around the target platform while measuring.

The vessel motions and target platform position with respect to the vessel can be accurately measured with the proposed LRU. The LRU system does not experience drift and future innovations for the Ampelmann system could be integrated with the LRU, due to the known position and orientation of the vessel to the target platform.

Acknowledgements

This MSc. thesis research is carried out under the supervision of J.W. (Jo) Spronck from the Delft University of technology, J.W. (Jurjen) de Vriend and A.G. (Alexander) Verweij of Ampelmann Operations B.V. I would like to thank Jo for his guidance, knowledge and support throughout this research, by keeping the balance between research and industry clear. I want to thank Jurjen and Alexander for their guidance and support as my daily supervisors. Their idea's and overview of the research kept me going in the right direction. A special thanks to Alexander for putting everything aside and helping to get the test set-up working.

This thesis project is made possible by Amplemann Operations B.V. I would like to thank them for this opportunity. A vibrant working atmosphere and great colleagues. A special thanks to my fellow graduate students at Ampelmann, making this research even more enjoyable. Boris Lenseigne from the Delft university of technology helped me in understanding the difficulties and solutions when it comes to computer vision systems, thank you.

Finally A special thanks to my girlfriend Charlotte de Lange for all her love and support, and my parents Gertie Fleuren and Arjen ten Pas for their love and support.

S. ten Pas
Delft, April 2017

Contents

1 Introduction **1**
- 1.1 The Ampelmann System . . . 2
  - 1.1.1 Stewart Platform, Transfer Deck and Gangway. . . . 2
  - 1.1.2 Control System . . . 3
  - 1.1.3 Operation Modes . . . 4
  - 1.1.4 Operation States . . . 5
- 1.2 Laser Range Finder . . . 5
  - 1.2.1 Laser Pulse Time-of-Flight Distance Measurement. . . . 6
  - 1.2.2 1-Dimensional . . . 6
  - 1.2.3 2-Dimensional . . . 6
  - 1.2.4 3-Dimensional . . . 7
  - 1.2.5 Timing, Jitter, Walk and Drift . . . 8
- 1.3 Ship 2 Ship Solution . . . 9
- 1.4 Applications . . . 11
  - 1.4.1 Compensate Residual Tip Motion . . . 11
  - 1.4.2 Control Tip Force . . . 11
  - 1.4.3 Auto Land . . . 11
  - 1.4.4 Motion Reference Unit . . . 12
  - 1.4.5 Park Assist . . . 12
  - 1.4.6 Sensor Fusion . . . 12
- 1.5 Research Innovation . . . 12
- 1.6 Problem Statement . . . 13
- 1.7 Goal of This Research . . . 13
- 1.8 Research Approach . . . 13
  - 1.8.1 Literature & Further Reading . . . 13

2 Specifications **15**
- 2.1 L-Type V4 . . . 15
- 2.2 Vessel Motions . . . 16
- 2.3 Vessel Landing Procedure . . . 18
- 2.4 Current MRU Set-up . . . 18
- 2.5 Requirements . . . 19

3 The LiDAR Reference Unit **21**
- 3.1 Sensor Position . . . 21
- 3.2 The Laser Range Finder . . . 22
  - 3.2.1 Resolution . . . 22
  - 3.2.2 SICK LMS 511 PRO . . . 23
  - 3.2.3 LRF Scan Orientation . . . 23
- 3.3 Inertial Measurement Unit . . . 25
  - 3.3.1 BNO055 . . . 26

4 Algorithm **29**
- 4.1 Process Approach . . . 29
  - 4.1.1 Preprocessing . . . 30
  - 4.1.2 Landmarks . . . 30
  - 4.1.3 Matching . . . 32
  - 4.1.4 Filtering . . . 34

- 4.2 Motion Extraction Algorithm . . . 35
    - 4.2.1 Point Cloud . . . 35
    - 4.2.2 Static Bounding Box . . . 36
- 4.3 Landmark Detection . . . 37
    - 4.3.1 Line Detection . . . 37
    - 4.3.2 Arc Detection . . . 39
- 4.4 Matching Point Clouds . . . 40
    - 4.4.1 Iterative Closest Point . . . 40
- 4.5 Sensor Fusion . . . 43
    - 4.5.1 Kalman Filter . . . 43
- 4.6 LRF and IMU Data Fusion . . . 45
    - 4.6.1 State Vector. . . . 46
- 4.7 Measurement Loop. . . . 47

5 Simulation & Testing 51
- 5.1 Simulation Model . . . 51
    - 5.1.1 LRF Simulation . . . 51
    - 5.1.2 IMU Simulation . . . 52
    - 5.1.3 Combining the Simulations. . . . 53
- 5.2 Test Set-up . . . 53
    - 5.2.1 Rotation Swing . . . 54
    - 5.2.2 Translation Sled . . . 55

6 Results 59
- 6.1 Simulation Model . . . 59
    - 6.1.1 Simulated Motions . . . 59
    - 6.1.2 Vessel Motion. . . . 59
    - 6.1.3 Simulation Errors . . . 60
- 6.2 Rotation Swing . . . 61
- 6.3 Translation Sled . . . 62
    - 6.3.1 Motions . . . 62
    - 6.3.2 Measurement Error. . . . 62
    - 6.3.3 Obstruction . . . 64
    - 6.3.4 Final Results . . . 66
    - 6.3.5 Algorithm Compute Time. . . . 66

7 Conclusions & Recommendations 69
- 7.1 Conclusions. . . . 69
- 7.2 Recommendations . . . 70

Bibliography 71

List of Figures 75

List of Tables 79

A Appendix 81
- A.1 Algorithm code MATLAB . . . 81
- A.2 Simulation model . . . 82
- A.3 Test Set-up . . . 83
    - A.3.1 Rotational Swing . . . 83
    - A.3.2 Translational Sled . . . 83

1

Introduction

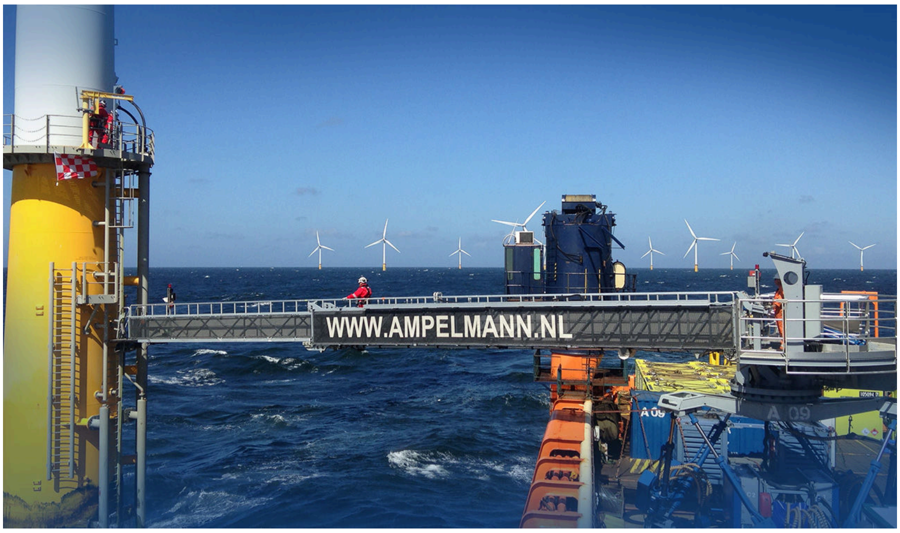

Figure 1.1: The Ampelmann system used to safely transfer people from a vessel to a offshore windmill.

Offshore structures, like Windmills and oil or gas platforms, require regular maintenance and operators to continue working. Rough sea and weather conditions caused a problem to get people on and off the structures, until Ampelmann came with a solution to safely transfer people between a vessel and offshore platforms. This people transfer is done by means of a motion compensating platform and gangway. With the Ampelmann solution workers are able to safely access these offshore platforms, even during rough weather and sea conditions.

To measure the vessel motions the Ampelmann system uses a highly accurate and expensive fibre optic gyroscope as their vessel motion measurement system called a Motion Reference Unit (MRU). The MRU consist of fibre optic gyroscopes and measures translational change in velocity by means of accelerations and rotational change in position by means of angular velocity. These changes are used to determine the displacements and angles of the vessel in six Degrees of Freedom (DoF). The use of a rate of change measurement system to measure displacement and orientation is known to introduce drift. Over time this drift influence will grow and the position and orientation of the vessel with respect to the target platform become unknown.

The Ampelmann system is also used to transfer people from one vessel to another vessel. This operation is called ship-2-ship transfer, where the Ampelmann system is located on the host vessel. The gangway of the Ampelmann system is used to connect to the target vessel so people can safely cross. In 2014 a proof of concept measurement setup was created by Verweij [43] to measure the target vessel motions. The measurement system consisted of a scanning Laser Range Finder (LRF) and was able to measure the motions of the target vessel,from the host vessel, without any added markers on the target vessel . The conceptual measurement system was able to accurately measure the motions of the target vessel. The extra measurement information available by measuring the distance to the target vessel could be used for other innovations within the Ampelmann system.

The Ampelmann system is mainly used to transfer people to offshore platforms instead of ship-2-ship transfer operations. As the measurement system designed by Verweij only measures the motions of the target vessel it has no added value during the people transfer operation to offshore platforms and is therefore not yet integrated in all Ampelmann systems.

A measurement system that uses the target as a reference has lot of potential for future innovations of the Ampelmann system. The added value of the LRF must be investigated for different applications within the Ampelmann system. Some information is required to discuss the possibilities and will be explained in the following sections: the current Ampelmann system setup and the working principle of a LRF. To get a better understanding of the interpretation difficulties of the measured data points the ship-to-ship solution is explained. The different applications are introduced using absolute reference measurement. The application with the most potential is chosen. Finally The problem statement and the goal of this research are stated.

1.1. The Ampelmann System

The motions of a vessel as a result of ocean waves introduce difficulties when accessing offshore structures or vessels. Access to these structures was mainly done by helicopter, a swing rope or lifting basket, until the Ampelmann system was introduced. Providing a safe solution by making *offshore access as easy as crossing the street*.

The main goal of the Ampelmann system is to provide safe access to offshore structures or vessels, by doing so the production and accordingly the revenue will increase. Ampelmann offers multiple solutions to accommodate a large range of safe offshore personnel and cargo transport. For smaller vessels the L-type system is used. large ships that support dynamic positioning the A-type Ampelmann system is used. For even more demanding jobs that can also include cargo lifting, the E-type is used. The specifications of these systems are shown in table 1.1 All these systems use the same three basic features as shown in figure 1.2: a transfer deck with gangway, a control system and a Stewart platform. Over the past years a lot of innovations have been implemented to extend the operations of the Ampelmann system. These subsystems and the operation modes will be briefly discussed in this section.

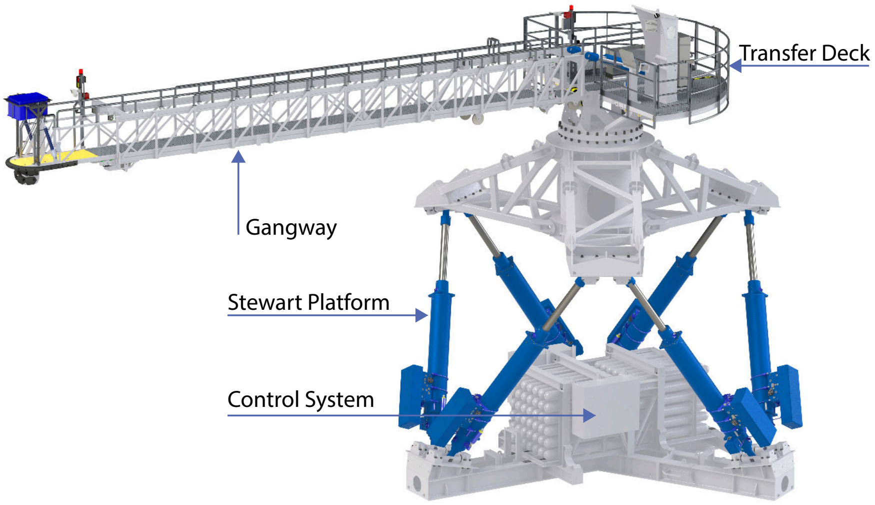

Figure 1.2: The Ampelmann E-Type System.

1.1.1. Stewart Platform, Transfer Deck and Gangway

A floating vessel has three translations (surge, sway and heave) and three rotations (roll, pitch and yaw). This results in six DoF as shown in figure 2.5. To compensate all these motions the Ampelmann

Table 1.1: Ampelmann systems

	Sea states up to H_s [m]	**Gangway range** [°]	**Height transfer deck** [m]	**Footprint** ∅ [m]
L-Type		-20 to $+22$	2.0	3.5
A-Type	3.0	-17 to $+17$	5.4	7.3
E-Type	4.0	-17 to $+17$	9.5	11.0

systems is derived from the motion platform used in flight simulators, a Stewart platform. This platform consist of a rigid base frame, six actuators and a rigid top platform used as a transfer deck (also called the Mercedes frame). Typical for a Stewart platform is its (nearly) octahedral configuration [6]. In the Ampelmann system hydraulic cylinders are used as actuators, these are driven by a Hydrolic Power Unit (HPU) which can be electrical or diesel powered.

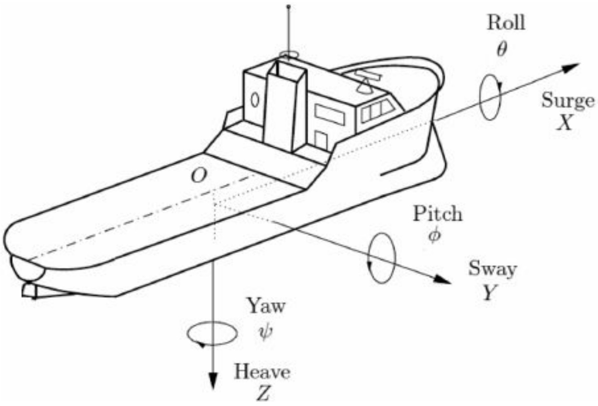

Figure 1.3: The six DoF's of a floating vessel.

1.1.2. Control System

Before any motion compensation can be done the motions need to be measured. In the current Ampelmann system's an Octans Fibre Optic Gyroscope, as shown in figure 1.4, is used as a measuring device and outputs the six motions of the vessel. This motion data is used to compensate for the vessel motions on the transfer deck of the Ampelmann.

Figure 1.4: The Octans fibre optic gyroscope six DoF's motion sensor.

The control system of the Ampelmann is a Programmable Logic Controller (PLC) which uses the output data to determine the length of each of the six cylinders, these cylinders form the Stewart platform regulated by valves, the position of the cylinders is send back to PLC via a feedback loop. A scheme of the control loop is shown in figure 1.5. The control loop is responsible for the correct execution of the following main tasks [43]:

- The movement of Stewart platform
- Control of the gangway
- Making sure the actuators do not saturate (cylinder reaches physical limit)
- Checking sensors for correct operation
- Control safety protocols and warnings

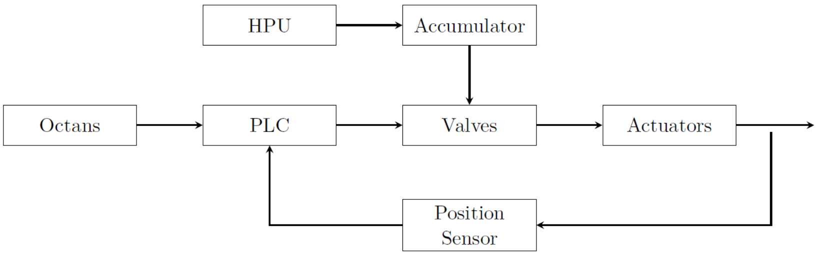

Figure 1.5: Ampelmann Control Model [43].

The complete Ampelmann system is redundant, meaning that every critical component has a second component which is immediately activated if the other component fails.

1.1.3. Operation Modes

The Ampelmann system is used for personnel and cargo transfer to seabed anchored or floating offshore structures. The Ampelmann system is designed to safely transport personnel from a floating vessel to a seabed anchored platform or windmill. Due to later innovations the Ampelmann system is these days also used for cargo transport or lifting. Small cargo is transferred using a KIB which is a motion compensated basket connected to the tip of the gangway as shown in figure 1.6a. For heavy lifting the CTS system is used which is a motion compensated crane as shown in figure 1.6b.

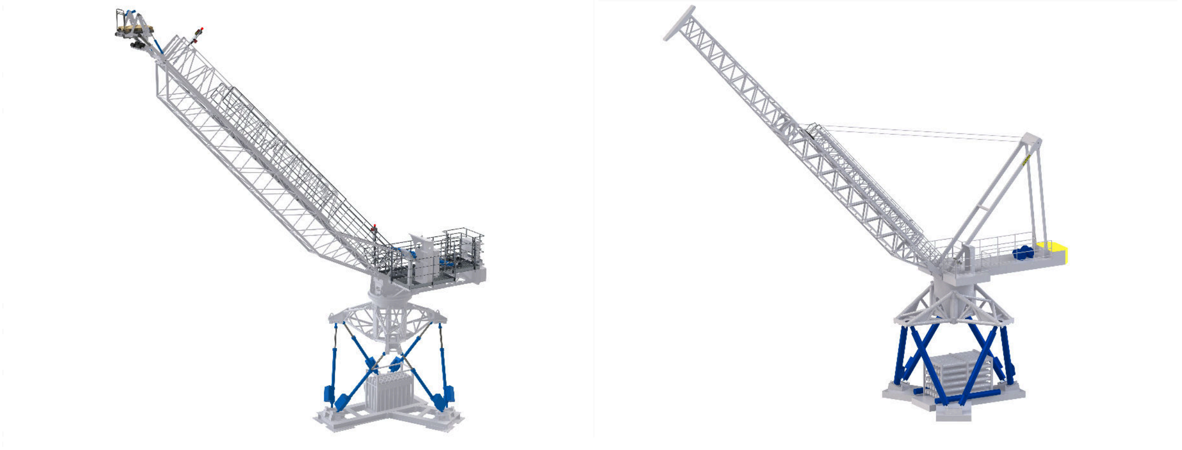

(a) KIB cargo system.

(b) CTS cargo crane.

Figure 1.6: Cargo and lifting additions for the Ampelmann system.

The Ampelmann is also used to transfer personnel or cargo to another vessel this is called Ship to Ship (S2S) operation. For this operation the motion of the target vessel is also compensated. This is done by the controllable motions of the gangway (telescoping ad luffing) combined with the rotation of the transfer deck (slewing), these motions are shown in figure 1.7. The motion information of the other vessel is measured by an extra Octans sensor and the output is transferred wireless to the Ampelmann. in 2014 a proof of concept master thesis research was conducted to use another measurement technique to measure the important motions of the target vessel [43]. in this research a scanning LRF is used measuring from the Ampelmann system. In the next section a more in-depth explanation about this measurement technique is given. The measurement technique using a scanning LRF has three main advantages over the Octans sensor:

- No need to put an extra sensor on each target vessel before performing the S2S operation.
- No wireless connection that is easily disrupted.
- No large latency delay, mainly caused by the wireless connection of the current measurement system.
- The used LRF is a SICK LMS 511 PRO and costs a fraction compared to an Octans sensor.

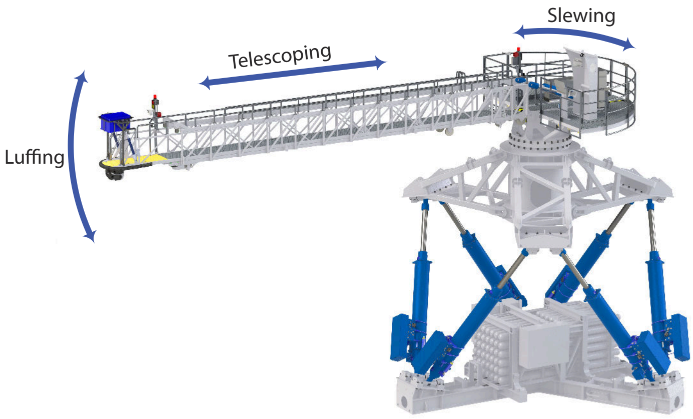

Figure 1.7: The controllable motions of the Gangway.

1.1.4. Operation States

To understand how the Ampelmann system is used the different states of the Ampelmann system during operation are explained in this section. The four states of the Ampelmann system are as follows:

1. **Safe Mode:** When the hydraulic pressure is turned on, the transfer deck will always be in safe mode. In this mode the hydraulic actuators are not actively controlled. Due to springs in the valves the cylinders are subjected to a small retracting force in the safe mode.
2. **Settled State:** After the hydraulic pressure system is turned on, the system does a short check of all the components and then goes into the settled state. In this state the platform is still retracted and not compensating any motion but now the PLC is controlling the valves.
3. **Neutral State**: defined as the elevation of the transfer deck at half of its maximum heave capacity. Vessel motions are still not compensated.
4. **Engaged State:** During the engaged state the Ampelmann system starts to compensate the measured ship motions, the control loop is active during this state to forward the valve information acquired from the inputs.

1.2. Laser Range Finder

A LRF is a non-contact absolute distance measuring technique also known as Light Detection And Ranging (LiDAR). In this section an introduction to this technique is given. The working principle is explained and the limitations. In the next part of this section the proof of concept system using a LRF is explained. The basic principle of active non-contact range finding devices is to project a signal (radio, ultrasonic or optical) onto an object and process the reflected signal to determine the distance. A high resolution range finder is required for positioning measurement, Therefore a range finder using an optical source is used [1].

1.2.1. Laser Pulse Time-of-Flight Distance Measurement

The Laser Pulse Time of Flight (ToF) distance measurement technique refers to the time it takes for an energy pulse to travel from its transmitter to an observed object and back to the receiver t_d. In the case where a light pulse is used as energy source the measured distance correlates to the speed of light $c \approx 3 \times 10^8 \mathrm{m/s}$. Because the light travels forth and back from the object the total distance is halved, resulting in the measured distance d

$$d = \frac{1}{2} t_d c \tag{1.1}$$

A schematic setup showing the working principle of the ToF LRF is shown in figure 1.8. This measurement technique is very useful when measuring distances longer than 1 m, systems where no reflectors are used and fast measurement applications such as scanning. The system works with centimetre precision and by averaging multiple measurements this can even be reduced to millimetre precision.

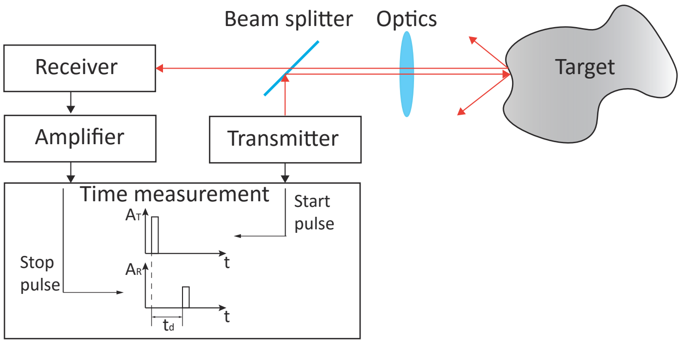

Figure 1.8: Block diagram of a time of flight laser range finder.

For the scanning capability the LRF is equipped with an angle encoder. For time critical scanning purposes a servo system is required to increase the measurement rate. These servo's drive a mirror to create a line scan, resulting in a 2-dimensional image or galvanometer-driven mirrors for 3-dimensional scans. Focal plane scanning is a technique that does not use mechanical beam scanning. Focal plane scanning uses the laser or an array of lasers to illuminate the total field of view on the target. The reflected image is received by a matrix of separate receivers [23].

To subtract motions from the measurement done by a LRF, a high measurement rate is required to extract these motions. The basic principle of motion extraction is based on the comparison of consecutive scans and a reference scan. The difference found between these scans is used to subtract the motion. In the following subsections the measurable motions are explained using the 1-,2- and 3-dimensional features of point cloud measurement scan.

1.2.2. 1-Dimensional

The most simple version of a LRF transmits a single laser pulse. With this single pulse the distance to the target is measured as shown in figure 1.9. When multiple pulses are transmitted and the target is moving, the only motion that can be measured over time is the translation in y-direction. A rotation, for example around the z-axis, could result in a measured motion in the y-direction. The 1-dimensional measurement does not give the information if the motion is a translation or a rotation, it only measures the motion of a point on the the target along the y-direction.

1.2.3. 2-Dimensional

When a line scanning feature is introduced in the LRF multiple distance measurements are taken resulting in a line cloud cloud of measured distance points, as shown in figure 1.10. The line scan measurement results in a 2-dimensional image or point cloud. When multiple line scans are taken over

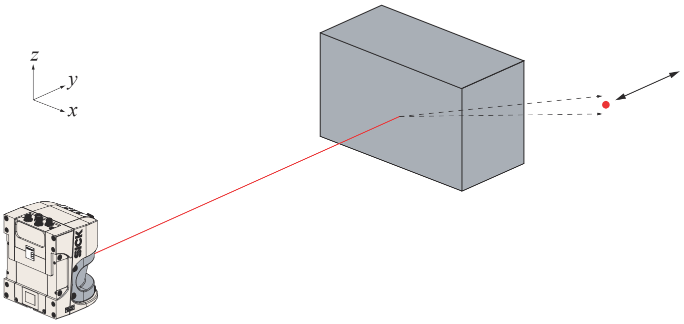

Figure 1.9: Schematic setup of a 1-dimensional measurement.

time of a moving target three motions can be measured: translation in y and z direction and the rotation around the x-axis.

The translation along the z-axis is measured by following the point cloud along the vertical line. The translation along y-axis is measured by the distance measurement of the measured points. And the rotation around the x-axis can be extracted with the information from the point cloud forming the lines, so that also the rotating point of the target is measured with the LRF.

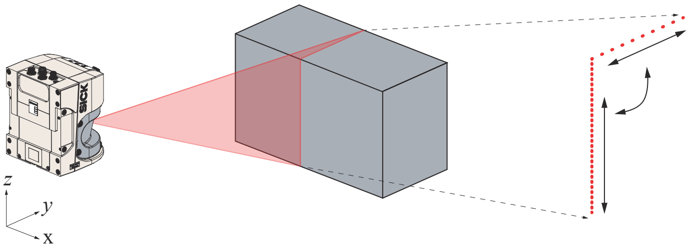

Figure 1.10: Schematic setup of a 2-dimensional measurement.

1.2.4. 3-Dimensional

Using a LRF with 2-DoF mirror, multiple mirror's, rotating a scanning LRF or a array of transmitters and receivers described in section 1.2.3 a 3-dimensional point cloud is created from the target as shown in figure 1.11. From this point cloud it is possible to extract all six DoF's when the target is moving and multiple measurements are done over time.

Compared to the line scan the extra measured motions are: rotation along the y- and z-axis and the translation along the x-axis. The translation along the x-axis is measured by following the horizontal line of the target or the begin and endpoint of the measured point cloud surfaces. The rotation about the z-axis can be gathered from the vertical surface of the point cloud and the rotation about the y-axis can be extracted from both point cloud surfaces.

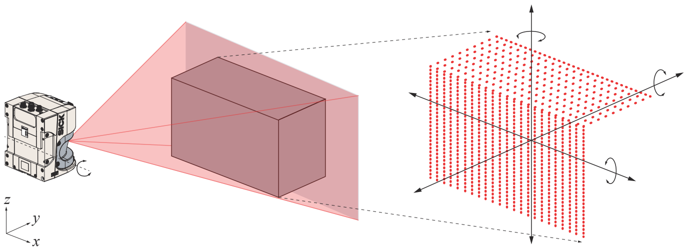

Figure 1.11: Schematic setup of a 3-dimensional measurement.

1.2.5. Timing, Jitter, Walk and Drift

The main sources of inaccuracy in laser range finders are noise-generated timing jitter, walk and non-linearity [26]. Most pulse measurement systems include a certain amount of electronic noise, introduced by the receiver, amplification of the pulse or the time discriminator. This noise causes uncertainty in the time at which the pulse cross the threshold as shown in figure 1.12. This is known as time jitter. The change in the amplitude of the pulse introduces a amplitude walk error in leading-edge timing system. Changing rise time of the pulses introduce a rise-time walk error. Both walk errors are illustrated in figure 1.13. Jitter and walk are both short-term introduced errors, Drift is a long-term introduced error. Drift can be caused by component ageing, changes in temperature during the measurement and so on.

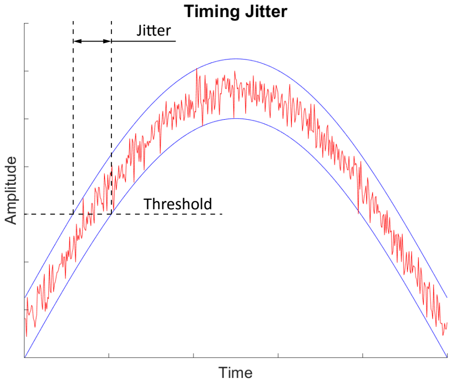

Figure 1.12: time jitter.

The time discriminator observes the time information from the electric pulse detector pre-amplifier and produce signal at the right moment. Commonly used principles for time discriminators are: leading-edge timing, zero-crossing timing and constant fraction timing. The choice for a discriminator is based on the desired time resolution, counting rate and dynamic range of the pulse. Constant fraction discrimination compensates with an attenuated signal which is created by a constant fraction that corresponds to the desired fraction of the full amplitude. This compensates for both amplitude and rise-time induced walk and is commonly used in the ToF measuring units of the LRF. Zero-crossing discrimination compensates only for amplitude variation and leading-edge does not compensate for any. The precision of distance measurement using the ToF principle can be greatly improved by averaging multiple measurements.

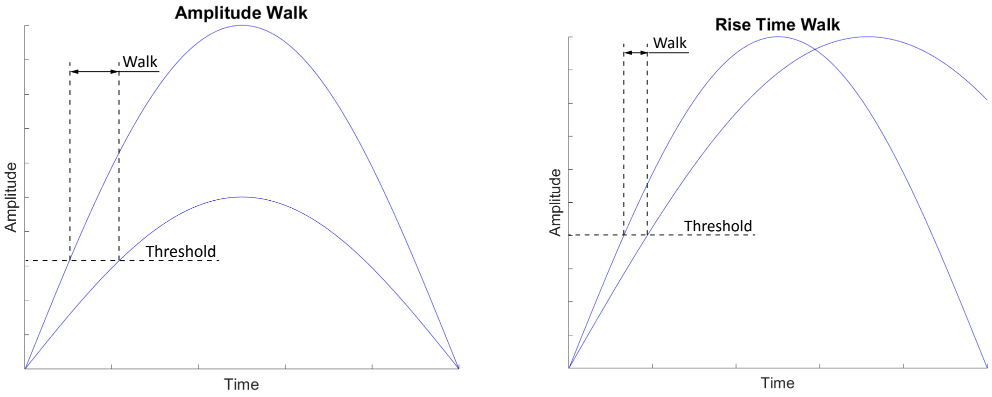

(a) Amplitude induced.

(b) Rise time induced.

Figure 1.13: Walk.

1.3. Ship 2 Ship Solution

Before the applications for a LRF measurement system for the Ampelmann are discussed in the next section a general understanding of the difficulties involved with position and motion extraction are highlighted. This is done trough the steps involved in the S2S LRF concept solution.

In S2S operation the target vessel is also moving. The motions of the target vessel that are compensated in this operation are: sway, heave and roll. To measure these motions with an LRF, a algorithm was produced by A.G. Verweij [43] to transform raw measurement data into target vessel motions that serve as input for the gangway control loop. This processing pipe-line is shown in figure 1.14.

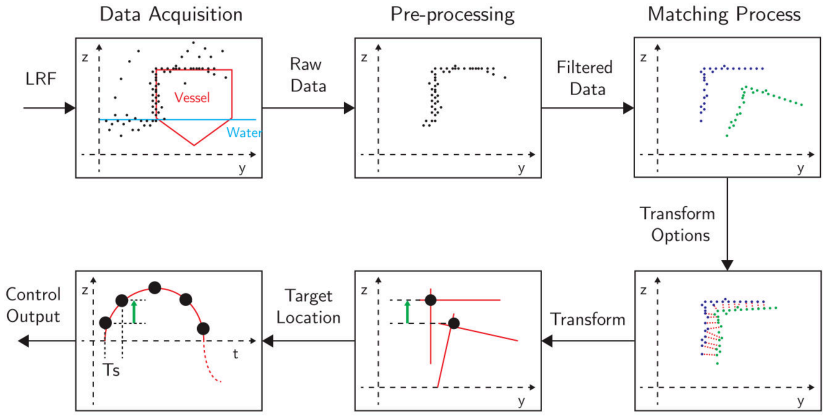

Figure 1.14: Data processing pipe-line [43].

Data acquisition
The data is acquired with an LRF, and a self made LRF scanning system called the AmpelScann.

Preprocessing
During the preprocessing block all irrelevant data is discarded. The scanner is able to make a line scan of 160° while the point of interest and the relevant edges of the target vessel can be contained by a smaller scan angle. during the preprocessing a bounding box is created around the target vessel, only the measurement points inside this bounding box are kept.

Outliers are data points that do not meet a certain expectations of the user. This does not mean an outlier is always bad, in fact they can help to determine weaknesses in the system and determine the sensitivity of the output. The outliers are found by calculating the velocity of the measurement points. When this velocity is higher then a certain threshold the data point is discarded.

The delay of the measurement output of the range finder and no delay on the angle encoder required that the data had to be synchronized before the scan measurement was correct.

Matching
To find the best matches between scans, both rotation and translation need to be determined. No active or passive markers are used in this process, therefore the matching algorithm is based on comparing a reference scan, in this case the first scan, with the next scans. The LRF measures multiple points in a scan and due to different disturbances these points are almost never exactly on the same line. For this reason the translational motions are calculated with an algorithm that makes use of a histogram to determine the x and y position of the points in the measured point cloud and there occurrence. This is shown in figure 1.15.

The histogram method to find the translational displacement was tested on measured data and concluded to be robust. The histogram method did require that both scans have the same orientation. Before the translational histogram method could be used the scan to be matched must be rotated to the same orientation as the reference scan.

The rotation of the target vessel is calculated by trying a range of angles on the measurement scan and compare it with the reference scan. The scans are rotated around their centroid, this is the mean location of all the scan-points of the measurement scan. The vector with angles to try for the best fit θ

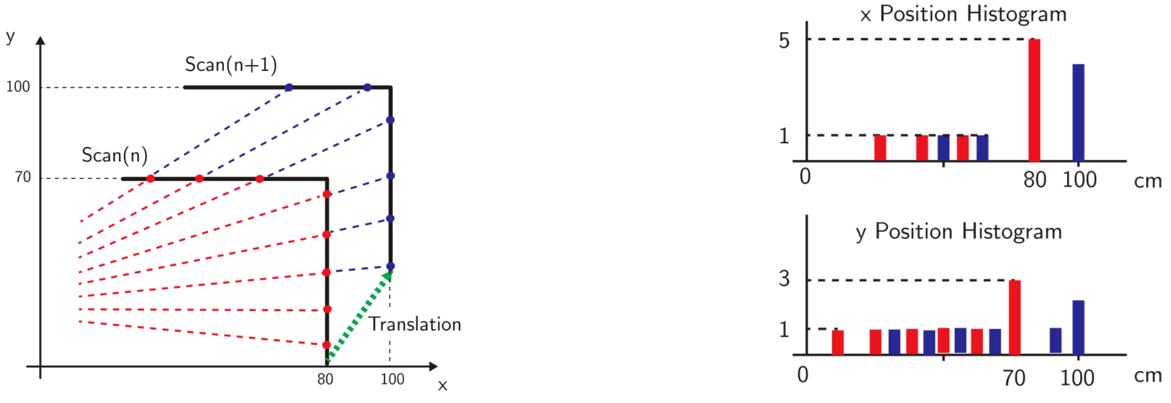

(a) Two scans [43].

(b) x and y translation histogram [43].

Figure 1.15: The point of two scans are used to create a histogram to find the translations with the use of a cross correlation.

goes from -10° to 10° with increments of 0.4. The rotation of the previous scan is used as a starting point for the next scan, because the solution will be close to the previous scan. During this procedure the resolution becomes better by changing the first and last value of θ to a value closer to the previous found angle solution. At the same time the length of θ stays the same and therefore the increments become smaller, increasing the resolution. This process of finding the rotations and translations is shown in figure 1.16.

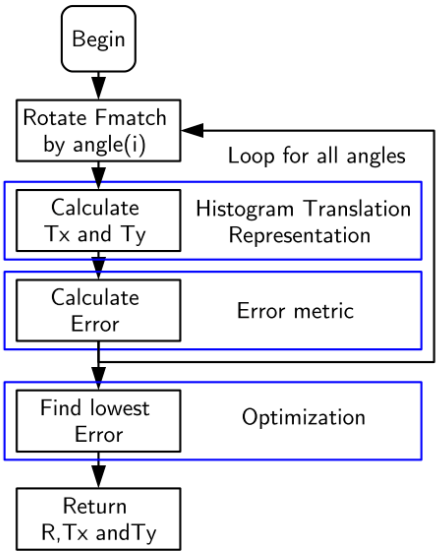
Begin
Rotate Fmatch by angle(i)
Loop for all angles
Calculate Tx and Ty
Histogram Translation Representation
Calculate Error
Error metric
Find lowest Error
Optimization
Return R,Tx andTy

Figure 1.16: Rotation an translation optimization algorithm [43].

Error metrics
To determine if the found match is the best possible match the error of the match is determined by calculating the distances between the points in the reference scan and measurement scan. The match that produces the smallest distance between the points of the reference and measurement scan is selected. The translations and rotations found are used as output of the measurement system

Smoothing
Every measurement step the position of the target vessel is determined by comparing the measurement with the reference scan. The reference scan is the first scan made. A match always has some error when compared to the target vessel motion. This error could be caused by overestimating or underestimation the target vessel motions, creating a output signal that jumps around the actual motion

of the target vessel and the output result does not describe a smooth motion. Filtering is applied to create a more usable output measurement signal of the position and motion of the target vessel.

1.4. Applications

The required information for applications of a absolute reference measurement system for the Ampelmann system is explained in the previous sections. In this section these different applications are explained. The potential of each application is determined in consensus with Ampelmann. The added value of the application is determined and a single application is chosen for this research.

1.4.1. Compensate Residual Tip Motion

The Stewart platform has a maximum range within it can compensate vessel motions. When this limit is reached safe transfer could still be possible if additional compensation is done with the 3 controllable DoF of the gangway. The LRF could for his application be mounted on the Ampelmann system transfer deck and immediately measure this residual motion. Using the controllable DoF Slewing, Luffing and Telescoping of the gangway to compensate. A sketch of the setup is shown in figure 1.17. Using a single LRF creates a measurement that can measure heave, sway and roll of the vessel. This system can therefore only compensate these residual motions with telescoping and luffing of the gangway. Residual motions in the surge direction can be compensated by slewing the gangway but are not measured in this setup.

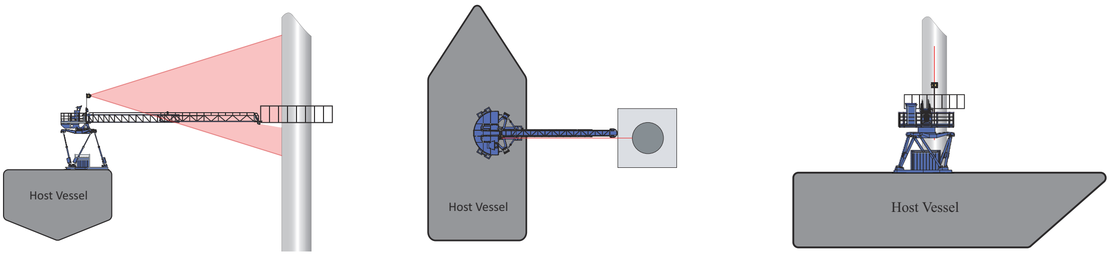

(a) side-view overview. (b) top-view overview. (c) rear-view overview.

Figure 1.17: A Measuring setup to extract Heave, Sway and Roll motions with a single LRF shown from different angels.

1.4.2. Control Tip Force

When the Ampelmann is in engaged mode and the gangway is landed to the target the tip of the gangway remains in place by a force that is induced by a constant pressure in the telescoping cylinder. This pressure is determined to make sure the tip stays connected to the target even during rough sea states. Undergoing transfer operations with milder sea states results in a force on the tip of the gangway that is much larger than the necessary force for safe transfer operation and can result in unnecessary wear of the gangway tip rubbers.

With the LRF reference measurement it is possible to control the force exerted by the gangway on the tip because the distance to the target is measured.

1.4.3. Auto Land

The Ampelmann system is currently controlled by two operators. They put the system in the different operations states and manoeuvre the gangway in the correct position for the transfer. When the LRF is rotated with a predefined angle and the position is followed with an encoder, it is possible to create a 3-Dimensional (3D) point map with the measurement. This map can be used by the operator to mark a landing point. The point can then be actively followed by the LRF and the landing of the gangway can be done with a control loop. It could even be possible to automatically detect a platform in the three dimensional point map and create a completely automated process. An example setup is shown in figure 1.18.

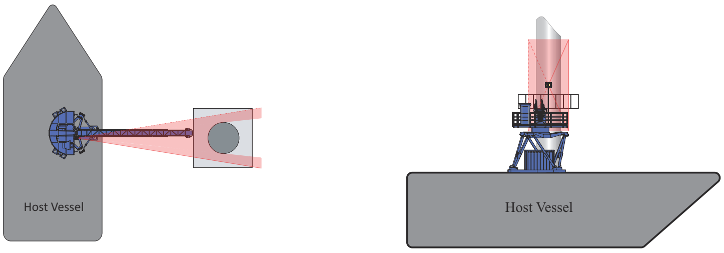

(a) top-view overview. (b) rear-view overview.

Figure 1.18: A Measuring setup to extract Heave, Sway, Surge, Yaw, Pitch and Roll motions with a single rotating LRF shown from different angels.

1.4.4. Motion Reference Unit

In section 1.1.2 the current motion reference unit, an Octans, is introduced. This sensor is sufficient as measurement input for the Ampelmann system to compensate vessel motions, but at high price. Secondly the position and orientations measurement suffer from drift.

3 Degree of Freedom
It is possible to extract three degrees of freedom with a single LRF as explained in section 1.2.3. The newly developed L-Type Ampelmann system, introduce in section 2.1, will not compensate all six degrees of vessel motions. This system is designed for small vessels that do not feature dynamic positioning. The smaller size of the sips requires that the Ampelmann system is placed at the back of the ship and transfer operation is only possible with the gangway and landing point in line with the long side of the ship and from the stern of the ship. The LRF could provide a cheap alternative as motion reference unit for a system where not all DoF have to be measured.

6 Degree of Freedom
Using two LRF's or a single rotating LRF with encoder creates a three dimensional measurement image from which all six DoF's of vessel motions can be extracted. This could not only replace the current motion reference unit, it has the capability of all the mentioned ideas in this section.

1.4.5. Park Assist

Before each transfer or lifting operation the vessel where the Ampelmann system is mounted on has to position itself in the correct place. For large vessels that feature dynamic positioning this is not a difficult task. Smaller vessels that lack dynamic positioning encounter difficulties when positioning the vessel. The vessels used with the Ampelmann L-Type system have to be positioned with the stern in the direction of the target. A horizontally scanning LRF could measure the distance and position of the target and can help the captain manoeuvre the vessel in the right place. Or even automate the entire process.

1.4.6. Sensor Fusion

Safety is one of the top priorities within Ampelmann. Al the Ampelmann systems are therefore designed redundant. The use of a LRF can ad to this redundancy by replacing the spare Octans. It can also contribute to the robustness of the system because a secondary measurement is done. The measured data of both sensors can be compared and the system can choose tot use the most logical measurement when one of the measurement systems makes a measurement error. In this setup both sensors can work together or the sensor can be used for error checking.

1.5. Research Innovation

The chosen application used in this research is the LRF as MRU. Designing a vessel motion measurement system based on a distance measurement to the target covers most aspects of the other suggested applications. The position of the target platform is known when using the LRF as MRU, if this position is known the implementation of innovations like: park assist, tip force control or automatic landing of the gangway could be implemented relatively easy afterwards.

The current Octans MRU is quite expensive, using the cheaper LRF sensor should result in a less expensive MRU for the Ampelmann system. Using a difference measurement sensor, like the currently used Octans, to determine the current position in time is prone to drift do to measurement noise. The current position of the measurement is based on the previous position, so over time this drift error will only grow. Using a measurement system that uses the target platform as reference to measure the vessel position and orientation over time does not tend to drift because each measurement update is done by measuring the distance to a target.

1.6. Problem Statement

The currently used sensor by the Ampelmann system to measure the vessel motions is based on velocity and acceleration sensing. Using changes in motion to measure current position is known to drift over time. Although the Octans measures very accurate, a small error will result in a larger error due to integration of the velocity and accelerations measured data to acquire the position and orientation. On top of this integration error is that the current position measurement is a summation of the previous position with the added displacements of the last measurements. In time this position drift could easily grow to distances larger then the workable area of the Stewart platform of the Ampelmann system.

With the current vessel motion measurement technique the location of the target is unknown. To allow for future innovations of the Ampelmann system knowing the position of the target with respect to the Ampelmann system could enable additional improvements to the system.

1.7. Goal of This Research

To solve the drift error with the current MRU, allow future innovations by knowing the location of the platform with respect to the moving vessel and reduce the total cost of the vessel motion sensor the goal of this research is:

Design a new vessel motion measurement system based on absolute reference sensing to measure vessel motions to replace the current MRU and allow for future innovations by measuring the position of the target with respect to the Ampelmann system. The system should not be sensitive to moving people on the target platform and must not rely on necessary additions, like markers, on the target platform.

1.8. Research Approach

To design a new vessel motion sensing system the requirements of the measuring system and specific Ampelmann system are determined in chapter 2. The sensors chosen to replace the Octans are depicted in chapter 3. Creating a robust computer vision based measuring system requires a smart way to interpret and combine the measured data as explained in chapter 4. To test the performance of chosen sensors and algorithm components a simulation model is created. To determine the performance of the new vessel motion sensing system a test setup is created. The simulation model and test setup are explained in chapter 5. The performance of the proposed vessel motion system called the LiDAR Reference Unit (LRU) and results of the simulation and testing are shown and discussed in chapter 6.

At last a conclusion on the performance and feasibility of the proposed measurement system is given. The conclusions and recommendations for future improvements and research are given in chapter 7.

1.8.1. Literature & Further Reading

The literature survey is embedded in this research Thesis work. For easy further reading, a summary of the substantiation and structure of the used literature is given.

To design different applications with the added benefit of absolute reference measurement for the Ampelmann system background knowledge of the influenced parts is required. In the introduction (chapter 1) the different, Ampelmann systems, their components and operation states are introduced [6]. A brief summary of the S2S transfer operation and innovations by Verweij [43] is given, where the principles for this research start. An introduction to the LRF ToF principles by Amann et al. [1] and common sources of noise for the LRF systems by Peiponen et al. [26]. The difficulties with a LRF measurement interpretation algorithm are briefly discussed for the S2S solution of Verweij [43]. This introduction results in applications and the problem statement for this research: replace the current

MRU that is expensive and suffers from drift in the position measurements. Measuring the target platform position with respect to the vessel enables future innovations for the Ampelmann system. These innovations could be introduced with the proposed absolute reference vessel motion measurement setup.

The specifications for the LRU (chapter 2) are determined. The motion is extracted by comparing consecutive LRF scans to a reference scan, in a sampling manner. Using a sampling based measurement system to measure motion requires a certain minimal sampling frequency to reproduce the measured motion [30]. The specifications of the current MRU, the Octans [16] play a large role in the requirements for the LRU.

The components used (chapter 3) to meet these requirements for the proposed LRU are selected based on the scan resolution [43]. The LRU requires the measurement of 3 translations and 1 rotation, this requires a 3D point cloud. This 3D point cloud could be produced with a LRF containing an array of transmitters and receivers as showed by Glennie and Lichti [12], a rotating 2-Dimensional (2D) scanner created by Wulf and Wagner [45] or the use of two 2D LRF's as used by Huhle et al. [15]. Different commercially available LRF scanner solution are listed in table 3.1, their corresponding data-sheets are cited in the table. The roll rotation measurement requires an additional sensor, the chosen Micro-Electro-Mechanical Systems (MEMS) Inertial Measurement Unit (IMU) and other commercially available rotation sensors and their specification are listed in table 3.3, their corresponding data-sheets are cited in the table.

The difficulty of LRF position, orientation and motion measurement lies in the interpretation of the measurement point cloud of the LRF scan. In robotics and autonomous vehicles this is often referred to as Simultaneous Localization and Mappaing (SLAM) [27]. The solutions chosen algorithms are explained in the algorithm for the proposed LRU (chapter 4).

To create an accurate and robust algorithm for the LRU the scan point cloud data is reduced. Less points make the algorithm more computational efficient [38] and the detection of unwanted walking people on the target platform can be avoided with landmark detection. RANdom SAmple Consesnsus (RANSAC) is a common used algorithm to detect lines and arcs [14, 18, 20, 24, 27]. To find mathematical relations for these landmarks on could use the book of Stewart [36]. In a 3D point cloud shapes could be detected with the offline solution by Schnabel et al. [31]. The trigonometric equations are used by Xavier et al. [46] for the detection of human legs. The polar coordinate system of the LRF measurement data is preserved by Noyer et al. [25] to detect lines.

Matching of consecutive scans to the reference scans extracts the rotations and translations of the compared point clouds used for the vessel motion measurement. The Iterative Closest Point (ICP) algorithm has improved in the last decade and the developments are summarized by Colas and Oswald [7]. On-line surface tracking with ICP is successfully achieved by Bergström and Edlund [2], Bergström et al. [3]. The steps taken by the ICP algorithm for the least-squares rigid motion extraction using Singular Value Decomposition (SVD) are summarized by Sorkine-Hornung and Rabinovich [35]. Part of the ICP algorithm is based on a nearest neighbour search [27]. A more conceptual matching algorithm that uses a sampling consensus is proposed by Kim et al. [18].

To combine the measurement data of both sensors and create a smooth the output results from the matching algorithm filtering is required. The Kalman filter is commonly used [44]. The filter is model based and can be extended to comply with non-linear systems [27, 38]. The Kalman filter can not be used in large environments for mapping, the Extended Information Form (EIF) algorithm [38]is able to map large environments due to the use of a information matrix, instead of the covariance matrix used in the Kalman Filter. The EIF algorithm only works in a offline batch manner. A solution for online use of the information matrix comes in the form of the Sparse Extended Information Filter (SEIF) [38]. Another online mapping solution for large maps is the Fast Incremental Mapping (FIM) algorithm. The FIM algorithm has a non-probabilistic core compared to the probabilistic nature of the other filtering algorithms mentioned. Due to the non-probabilistic core of the FIM algorithm problems could occur with cyclic motions of the LRF a solution is provided for this issue as well by Thrun et al. [38].

The literature introduced in the algorithm chapter is illustrated in an overview in figure 4.7.

2

Specifications

To design a Motion Reference Unit (MRU) the requirements of the measurement setup need to be determined. The goal is to design a MRU for the currently developed L-Type V4, which is currently still in a concept phase. One of the goals of the L-type V4 is to have more competitive price on the market. Though the L-type V4 is still under development, the maximum operating conditions are set. and explained in this section. The requirements are determined of the LiDAR Reference Unit (LRU), they are based on the currently used MRU and the limitations set by the Ampelmann L-type V4.

2.1. L-Type V4

To offer a solution to all the segments of the offshore personnel transfer industry Ampelmann created the L-Type system. This system was intended for smaller, so called Fast Crew Supplier (FCS), vessels. These vessels have a length between 30-55 m and therefore are not suited to accommodate an A-Type or the even larger E-Type Ampelmann system. The main purpose of these vessels is transferring people to offshore platforms oil and gas platforms and offshore windmills. The L-Type is placed at the stern of a vessel and the gangway is positioned in line with the vessel.

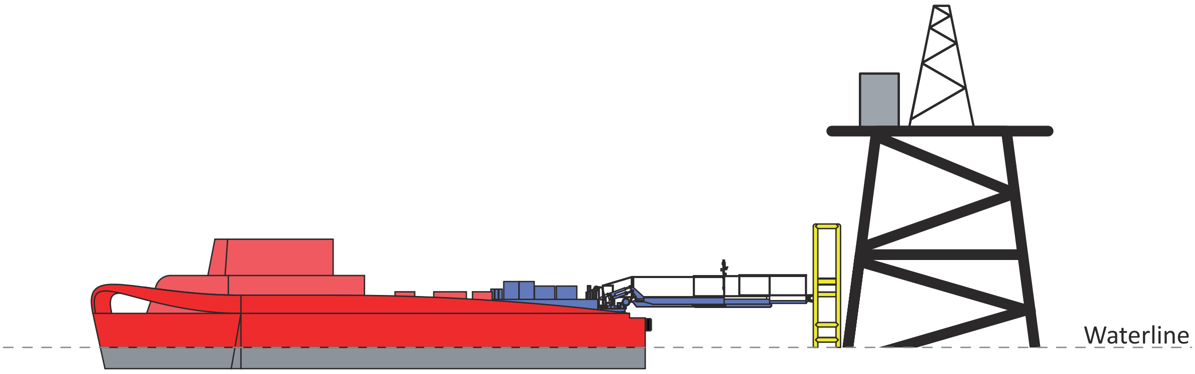

Figure 2.1: Example setup of the Ampelmann L-type V4 concept transfer operation is done from the stern of the vessel..

The previous versions of the L-Type use a Stewart platform to create 6-Degrees of Freedom (DoF) motion compensation during the landing of the gangway on the platform. During personnel transfer operation the Stewart platform is not used and the system could only passively compensate the vessel motions. This passive compensation is done by keeping the tip of the gangway attached to the platform by exerting a constant pressure. The gangway will follow the tip by using the three DoF's of the gangway system: Telescope length, luffing angle and slewing angle. This makes the expensive Stewart system unnecessary during transfer operation. In the first years of operation there was a lot downtime due to defect cylinders in the Stewart platform of the L-Type. So it was time for a new version of the L-Type, the L-Type V4.

The L-Type V4 is a new concept where not all 6-DoF's are compensated. It does not use the familiar Stewart platform. Instead it uses the gangway to compensate the motions at the tip of the gangway. The L-type is placed at the stern because at the stern there is no ridge. A typical transfer example on an FCS using the Ampelmann L-Type V4 is shown in figure 2.1. During the transfer operation, from the vessel to the platform, the intensity of the vessel motions are damped out along the length of the gangway. Making sure a safe transfer is conducted. The DoF's that are controlled and their range during landing and transfer operation of the L-Type V4 are: the telescope length 6.5 - 11.5 m, the luff angle −30 - 30°, the slew angle −45 - 45° and the roll angle of the gangway −20 - 20°. These controllable DoF's are illustrated in figure 2.2.

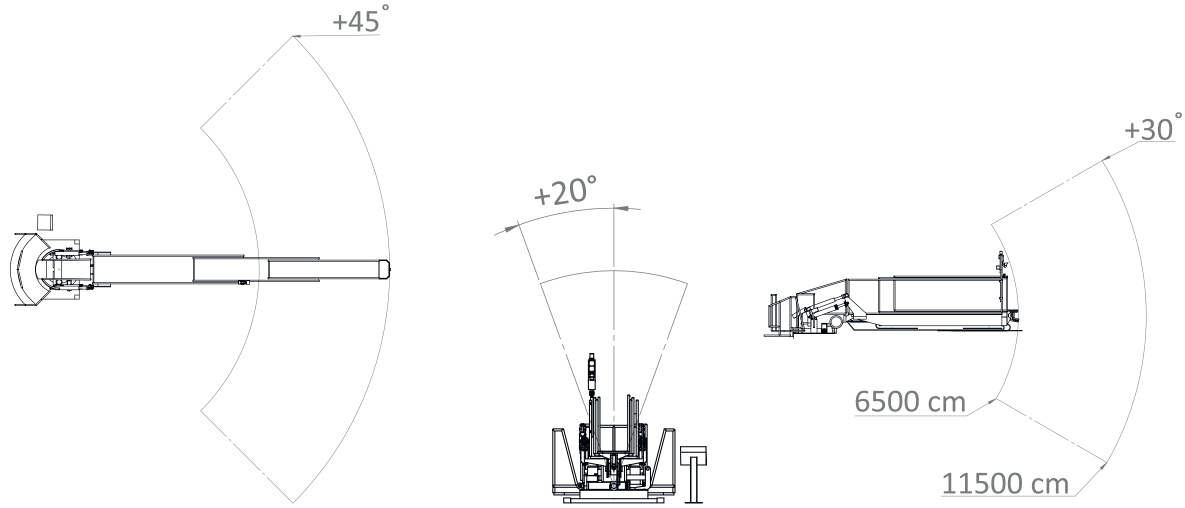

(a) Slew angle. (b) Roll angle. (c) Luff angle and telescope length.

Figure 2.2: The controllable angles and translation with their mechanical limit's on the L-type V4 concept.

2.2. Vessel Motions

To estimate the order of magnitude and dominant frequency's of the vessel motions. a simulation is done using the Ampelmann Workability Evaluation of ship Orientated Motions and Cylinder Excitations (AWESOME) software. This software uses a JONSWAP wave spectrum and simulates ocean waves based on *significant wave height* H_s and their *zero up-crossing wave period* T_z. In a common sea state these are $H_s = 2$ and $T_z = 5.5$, resulting in a modelled water surface elevation as shown in figure 2.3a. The Ampelmann L-Type V4 is designed to work till $H_s = 2$. In this figure the water surface elevation is plotted in the approach angle with respect to the vessel that induces the fastest and largest vessel motions of: $90°$. The water surface elevation is used to simulate vessel motions. To determine the the dominant frequencies of the sea waves a Power Specrtal Density (PSD) of the sea state is shown in figure 2.3b.

The Damen FCS, shown in figure 2.4a, is a small vessel in the offshore industry with a length of 50 m. The Aker Wayfarer, shown in figure 2.4b, is a large FCS vessel in the offshore industry with a length of 160 m. During the design of a ship or floating structure a Response Amplitude Operator (RAO) is calculated for al vessel hull designs and wave headings. A RAO is a set of statistics that are used to determine the motion response of that vessel at sea. The RAO information of the Damen FCS and the Aker Wayfarer are used to calculate their motion responses in their Centre of Gravity (CoG), these vessel motions as response to the water surface elevation for the Damen and Aker are plotted in figure 2.5.

The smaller Damen FCS is more influenced by the waves than the lager Aker Wayfarer. Resulting in larger vessel motions. To determine the frequency range in which these vessel motions operate a PSD analysis is computed using the vessel motion time series as simulated above. This results in the PSD shown in figure 2.6.

The frequency of the majority of motions of the larger Aker Wayfarer are between 0.1 Hz - 0.2 Hz. For the small Damen vessel most motions are in the frequency range of: 0.1 Hz - 0.4 Hz. The motions

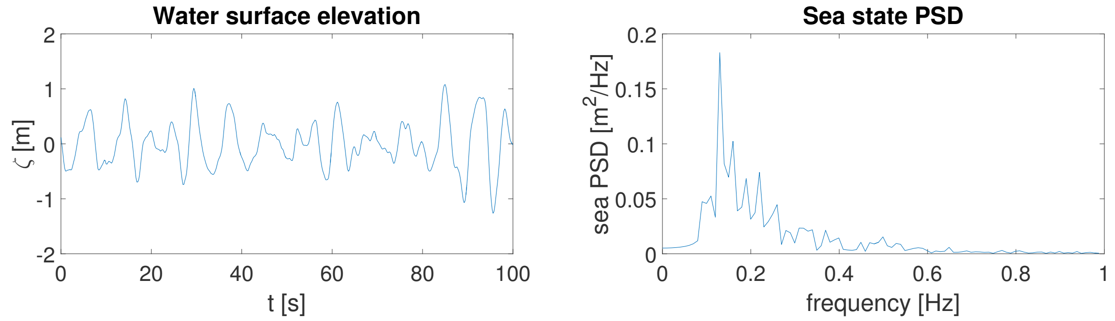

(a) Water surface elevation with 90° impact angle with respect to the vessel.

(b) Sea state frequency's in a PSD.

Figure 2.3: Water surface elevation with 90° impact angle with respect to the vessel and the corresponding frequency's in a PSD.

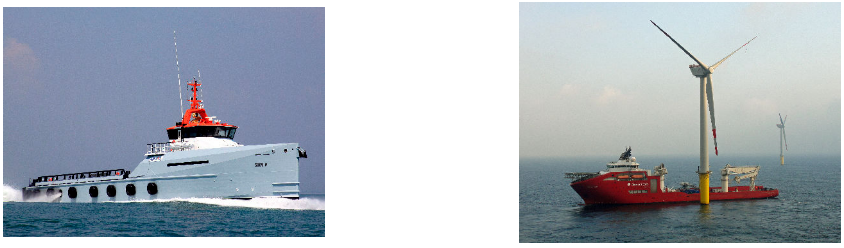

(a) Damen FCS.

(b) Aker Wayfarer.

Figure 2.4: Examples of a small and large offshore FCS vessel.

of the small vessel (Damen FCS) are faster than the large vessel (Aker Wayfarer), especially in the rotational DoF's of the vessel. The motions induced by the waves create larger movements in the small Damen vessel compared to larger Aker vessel.

The L-Type V4 is designed to operate on even smaller vessels than the Damen FCS, like the MEO Express 79 with a length of length of 38 m. The manufacturers of these smaller FCS vessels provide not all the RAO data required by the AWESOME simulation to calculate the vessel motions. The trend as shown in figure 2.6 is that the vessel motions are faster and of a larger amplitude then large vessels. The MEO Express will move with an even higher frequency than the Damen FCS. Taking a look at the PSD of the sea in figure 2.3b shows that the frequency's of the sea waves lie between 0.1 Hz - 0.6 Hz. For the calculation of the minimal required sampling frequency and bandwidth of the MRU 0.6 Hz is used.

To represent the analogue vessel motions in a control system sampling is required. the created discrete-time value can only approximate the continous-time value and has to comply with the rule: *'Any conversion is only perfect, when it can be reversed to reproduce the original input signal'* [30]. In signal analysis the minimal sampling frequency f_s is calculated using the Nyquist-Shannon theorem:

$$f_s > 2 \cdot f_n \tag{2.1}$$

where f_n is the Nyquist frequency and stands for the largest frequency present in the analogue signal. For the vessel motions this means that the minimal sampling frequency is

$$f_s = 2 \cdot 0.6 = 1.2\text{Hz} \tag{2.2}$$

In practice it is better to take a higher sampling frequency, especially in feedback controlled motion systems. The dynamic performance is determined by the phase margin and a closed loop system requires low pass filters which introduce a phase delay. The Ampelmann control loop uses a low-pass filter. Therefore at Ampelmann it is common to take a sampling frequency of $f_s = 50$Hz as the minimal output frequency of the MRU. This measurement output frequency will result in smooth operation of the motion compensating Ampelmann system.

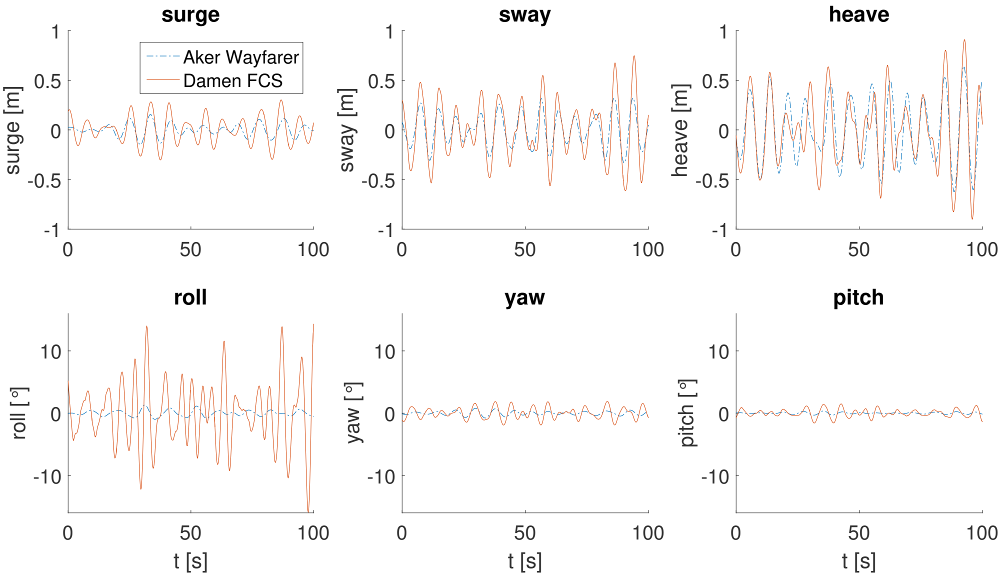

Figure 2.5: Simulated vessel motion.

2.3. Vessel Landing Procedure

The L-Type V4 system is placed at the stern of the vessel, meaning that the vessel has to turn around at some point for the transfer operation. In most cases the captains turn their vessel 100 m away from the platform. The vessel is then reversed in to place for the transfer operation.

When the Laser Range Finder (LRF) is mounted at the stern of the vessel, this reverse sailing allows to start measuring before the landing of the gangway or the transfer operation started. During the measurements, while the vessel is still getting in position, preprocessing parameters could already be defined, or a rough estimate of the vessel motions could be done to determine the current sea-state as illustrated in figure 2.7.

2.4. Current MRU Set-up

The Ampelmann systems are currently controlled with the control system explained in section 1.1.2. The input signal for the vessel motions is measured using the Octans Fibre Optic Gyroscope mounted to the base-frame of the Ampelmann system. The Octans sensor measures and generates real-time output for roll, pith, yaw, heave, surge and sway of the vessel at the location where the sensor is mounted: in the control cabinet on the base-frame of the Ampelmann system. The specifications of this Octans MRU are listed in table 2.1.

Table 2.1: iXblue Octans Motion Sensor Specifications [16]

Feature	**Value**	**Unit**	**Comment**
Accuracy *Heave/Surge/Sway*	$0.05, 5$	m, %	whichever is greater
Accuracy *Roll/Pitch/Yaw*	0.01	°	RMS
Resolution *Roll/Pitch/Yaw*	0.001	°	
Rotation rate	750	°/s	Up to
Acceleration rate	± 15	g	1g ≈ 9.81 $\mathrm{m/s^2}$
Rotation range *Roll/Pitch/Yaw*	0 to $360/\pm 180/\pm 90$	°	
Data Output Rate	0.1 to 200	Hz	
Timing	2.35	ms	Fixed latency
Price	$80,000$	€	Without bulk discount

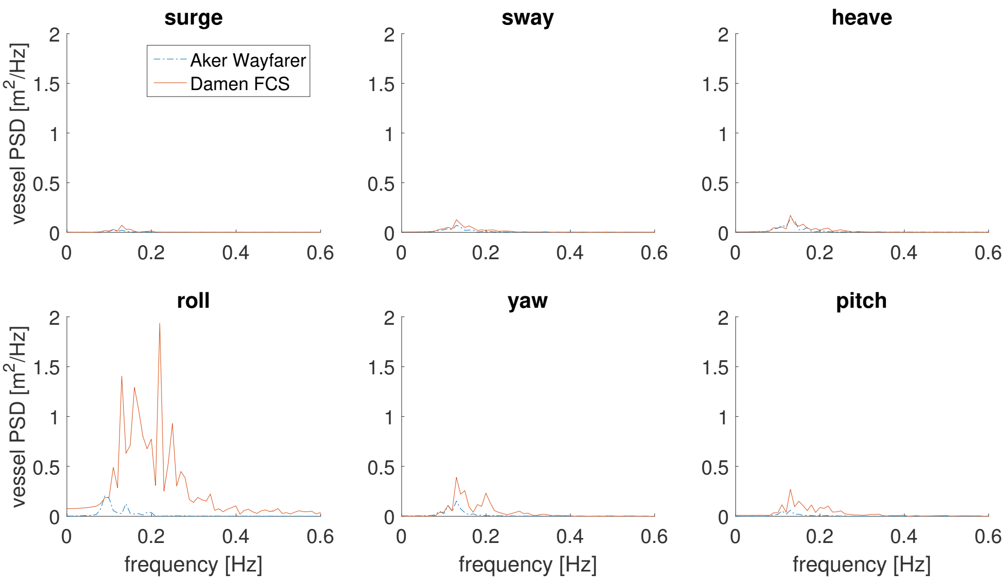

Figure 2.6: Vessel PSD.

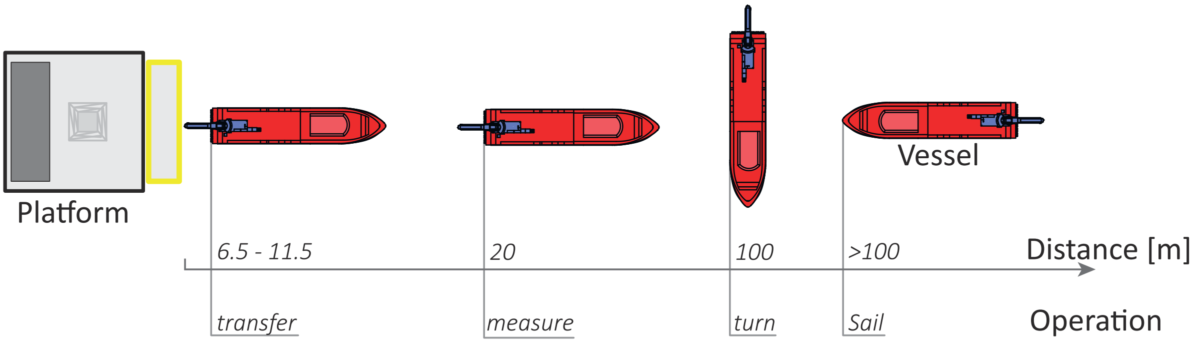

Figure 2.7: The normal landing procedure for small FCS vessels for people transfer.

2.5. Requirements

The final requirements for the LRU are based on the discussed sections of this chapter. The data output rate is based on the update rate of the current Ampelmann system control loop. The translational accuracy is equal to that of the Octans motion sensor. The rotational accuracy of the Octans sensor is better than the Ampelmann systems requires to function optimal, so an less accurate rotational accuracy is chosen for the LRU. The maximum measurement distance to the target is based on the landing procedure of the vessel and the maximum transfer distance of the L-Type V4. The requirements for the LRU are summarized in table 2.2.

Table 2.2: specifications

Feature	**Value**	**Unit**
Measuring distance	≤ 20	m
Measured output	Heave, Surge, Sway and Roll	m, °
Accuracy	$0.05, 0.1$	m, °
Data output rate	50	Hz

Suitable sensors and algorithm selection to achieve these requirements are discussed in the next chapter.

3

The LiDAR Reference Unit

The sensors used in the LRU to achieve the requirements stated in the previous chapter are chosen in this chapter. The position and orientation of LRF is defined and an extra sensor in the form of a micro-electromechanical Inertial Measurement Unit (IMU) is chosen to allow for fast measurement output and the measurement of roll.

3.1. Sensor Position

The placement of the LRU on the vessel depends on a list of requirements:

- Clear view from the LRF line of sight to the target platform.
    - This guarantees that the measurement of the LRF is not blocked by anything.
- Attached close to or on the Ampelmann L-Type V4.
    - To make the system compatible with most vessels and their deck configurations it is best to place the sensor in a location on the ship deck that is already used by the Ampelmann system.
    - The closer the sensor is placed to the location of the actuators, the less the measured data has to be mapped to these locations.

The current Ampelmann control system uses the motion measurement as an input or feedforward signal as stated in section 1.1.2. The measured motion is translated in platform cylinder lengths and the cylinder valve positions are determined via a lookup table. The length of the cylinders is measured and this is used to adjust the cylinder valves with a feedback loop.

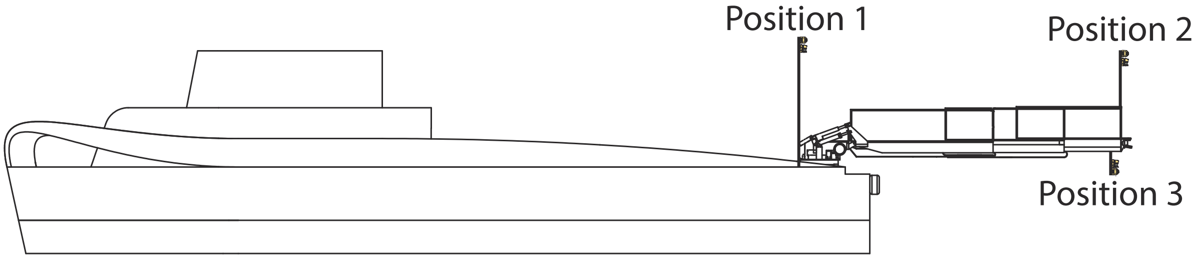

Figure 3.1: Placement positions for the LRU on the vessel/gangway.

From possible positions for the LRU in figure 3.1, only position 1 is suited to measure the vessel motions for feedforward control. From position 2 and 3 only the difference between the gangway and the target can be measured. This difference measurement would require a feedback loop to use the measurement data. This feedback loop would introduce a limited reaction speed because an error in the difference has to occur before the controller can correct for it [30].

Position 2 and 3 are close to the position of the gangway that needs to be controlled. Any undesired motions of the Ampelmann system, that can be introduced by the mechanics or dynamics of the L-Type V4, are measured when the sensor is placed in location 2 or 3. When using a feedback controller these undesired motions can also be compensated by the Ampelmann system.

During the transfer operation the tip of the gangway is in contact with the target platform. The closer the LRU is placed to the the platform the larger the scanning angle of the LRF needs to be to be able to scan the entire platform. It is easier to determine the location of the full platform when scanned from a far than being to close near the platform. To measure a translation perpendicular to the platform at least two distinct features of the platform need to be visible in the measurement point cloud. When the LRF is located at position 2 or 3 the possibility exist that all scan points get blocked by a single beam losing measured DoF's due to the loss of different shapes.

To make sure the LRU could be implemented easily in the current Ampelmann systems and the high demand for robustness is achieved, the LRU is placed at position 1 for this research. This guarantees direct vessel motion measurement and the ability to scan a larger portion of the platform compared to the other positions.

3.2. The Laser Range Finder

Previous research showed that accurate results could be achieved using a scanning LRF. In this section the specific LRF is chosen and the scan plane orientation is explained. To avoid the detection of unwanted obstacles on the target platform a landmark or feature detection algorithm is introduced that allows for the detection of straight lines and arcs in the measurement point cloud. To detect these landmarks a minimum amount of scan points of the shape of the landmark is required to successfully detect the landmarks.

3.2.1. Resolution

For feature extraction it is important to have enough measurement points to robustly determine the feature. In mathematics one can calculate a line formula of a straight line with only two points. Figure 3.2 shows that the noisy measurement data of a laser range finder makes this impossible. To correctly describe the line feature more measurement points are needed to correctly fit a line. To extract information about more difficult features like cylinders from an offshore platform even more points are required to robustly determine the arc.

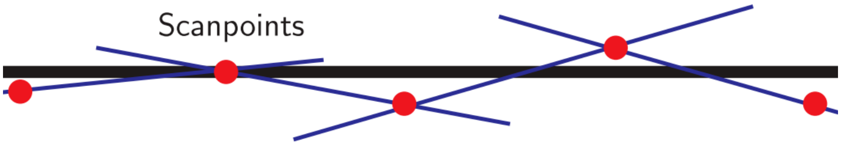

Figure 3.2: Noise makes it impossible to correctly describe a scanned line with only two points [43].

To determine the required resolution a simple example is shown in figure 3.3. To get eight measurement points $p = 8$ on a straight line with a length of $l = 0.5$ m from a distance of $d = 20$ m the total scan angle α and the required angular resolution $\Delta\alpha$ are calculated as follows:

$$\alpha = 2\sin^{-1}\left(\frac{l}{d}\right) = 1.432°, \quad \Delta\alpha = \frac{\alpha}{p} \leq 0.179° \tag{3.1}$$

The distance from the scanner to the target has a large influence on the required resolution as shown in the previous example. In this example other aspects that make it even harder to get a minimal amount of points to extract a feature are not even taken into account, like:

- Features with difficult shapes that require more scan points to extract correctly.
- The angle of attack from the LRF to the target feature.
- Blocking of certain parts of the target feature by other parts of the platform, for example a railing.
- Missing scan points on poorly reflecting material or due to a very large angle of incidence.

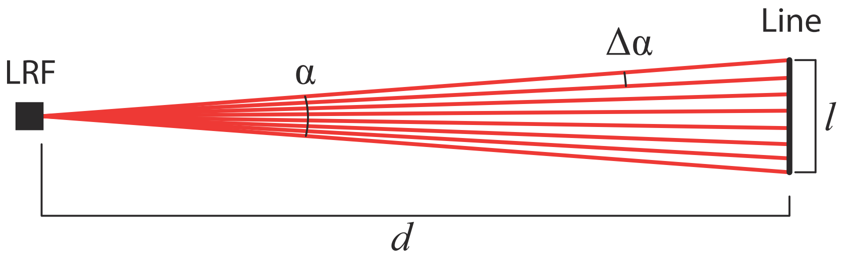

Figure 3.3: Simple example to determine the required resolution of the LRF.

The downside of a LRF with a high resolution is the larger amount of data that needs to be processed by the algorithm, this increases the computation time.

The amount of measurable translations and rotations for a point-, line- and surface scan as explained in section 1.2.1 help determine the required LRF configuration to measure the required translations and rotation for the LRU. All six DoF's of a vessel could be measured using a 3D surface laser scanner but the same data could also be measured using two or more of the cheaper 2D line scanners. In table 3.1 a couple of popular commercially available LRF's are listed.

All the 3D scanning LRF's have a high resolution in their scanning or horizontal plane and a low resolution in their vertical plane. This is due to the fact that all these 3D scanners don't use a scanning mirror or a rotation axis to acquire the vertical measurement points. Instead array's of laser transmitters and receivers are used [12], each transmitter receiver pair is called a channel. The SICK LD-MRS 8-L uses 8 channels, the Velodyne Puck 16 channels and the Velodyne HDL-32E and HDL-64E respectively 32 and 64 channels. This non-scanning technique in the vertical plane enables high output rate scanning to acquire a full 3D 360° point cloud. Though the vertical resolution is not enough for the challenge in this research.

One of the solutions to acquire a better resolution in the vertical plane is to introduce an extra scanning rotation axis with a 2D LRF. There are commercial products available that use this technique This, like the RIEGL LMS-Z210ii-S that has a vertical resolution of 0.01 - 0.75°. The downside is that a complete 360° scan takes 24 s, which is not fast enough for the LRU motion extraction. In an attempt to transform an 2D LRF by O. Wolf and B. Wagner [45] only takes 5 s to create a full 360° point cloud, this is still to slow and a low scan resolution of 1° is used. Adding a rotation axis to a 2D LRF is a solution for a better resolution in the horizontal and vertical plane, only the measurement time for a full point cloud take to long for the online motion measurement system.

Another solution is to combine two 2D LRF's with a perpendicular scanning plane orientation as proposed in [15]. In this research the LRF's can move in 6-DoF's while scanning and a matching process calculates the position and orientation of the LRF system. Using two LRF's with perpendicular scanning planes ensures a good resolution in both planes. A setup with two LRF's is chosen and the best 2-Dimensional (2D) LRF that meets the required resolution is the SICK LMS 511 PRO, which is the chosen LRF for this research.

3.2.2. SICK LMS 511 PRO

Combining two SICK LMS 511 PRO's with perpendicular scan planes provide the required resolution, range and accuracy in two planes. The SICK LMS also offers user defined settings like: angular resolution, field of view and data output rate. These settings can be used to optimize the algorithm required for the motion measurement extraction. To guarantee operation in outdoor environment the LRF is water and dust proof according to the IP67 rating. It can measure up to five echo's which enables measurement in rain, mist or dust, as illustrated in figure 3.5. The SICK LMS outputs the distance, scan angle and reflection level of every measurement point of a complete scan. The light emitted by the SICK LMS 511 PRO is invisible infrared light with a wavelength of 905 nm and is eye safe. The important specifications of the SICK LMS 511 PRO are summarized in table 3.2.

3.2.3. LRF Scan Orientation

With the use of two 2D LRF's the scan plane orientation needs to be chosen, perhaps a diagonal scan holds more important measurement information for the LRU than a vertical or diagonal scanning plane.

Table 3.1: LRF specifications

Manufacturer **Model**	**Type** **Range** [m]	**Horizontal Resolution [°]** **Field of view [°]**	**Vertical Resolution [°]** **Field of view [°]**	**Accuracy** [mm] **Scan rate** [Hz]	**Price [€]** **Units req.**
Velodyne	3D	0.08 - 0.35	0.4	±20	60.000
HDL-64E [42]	120	360	26.9	5 - 20	1
Velodyne	3D	0.1 - 0.4	1.33	±20	30.000
HDL-32E [41]	100	360	41.33	5 - 20	1
Velodyne	3D	0.1 - 0.4	2.0	±30	8.000
Puck [40]	100	360	30	5 - 20	1
SICK	3D	0.125 - 0.5	6.4	±100	16.000
LD-MRS 8-L [33]	300	110	0.8	12.5 - 50	1
SICK	2D	0.1667 - 1		14	5.000
LMS 511 [32]	80	190		25 - 100	2
Scanse	2D	1.4 - 7.2		40	350
Sweep [29]	40	360		2 - 10	2

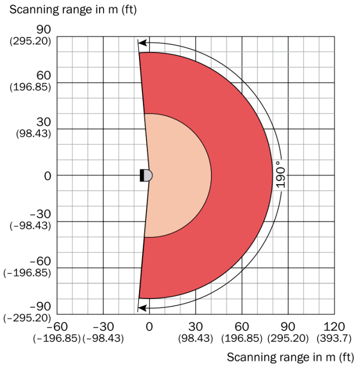

Figure 3.4: The maximum possible scan angle for the SICK LMS 511 Pro, dark red illustrates a scan range up to 40 m for 10% remission factor and dark red illustrates the maximum range of 80 m. [32]

To investigate the scan plane orientation a simple example with three different scanner orientations; horizontal, vertical and diagonal is shown in figure 3.6. This figure is intended to demonstrate the ability to measure displacements in the x, y-direction.

All three orientations are able to measure the in-plane distance because the LRF measures the distance to the target. Comparing the three scans of the horizontal scanner to the reference frame, it becomes clear that this scanner orientation is only able to measure the horizontal displacement. The same goes for the vertically orientated scanner, it can only measure vertical displacements. Could the diagonally orientated scanner provide information about the vertical and horizontal displacement in one solution? For all three displacements a difference is visible when the scans are compared to the reference scan. However the only displacement with a result that can be translated back to the original displacement is the diagonal displacement. The horizontally and vertically orientated scanners are able to measure the corresponding component of the diagonal displacement.

Due to the orientation of the vessel during the people transfer operation it is not possible Without a full 3D point cloud to measure the vessel's roll motion. An extra sensor that can measure roll accurately is required for the LRU to meet the requirements.

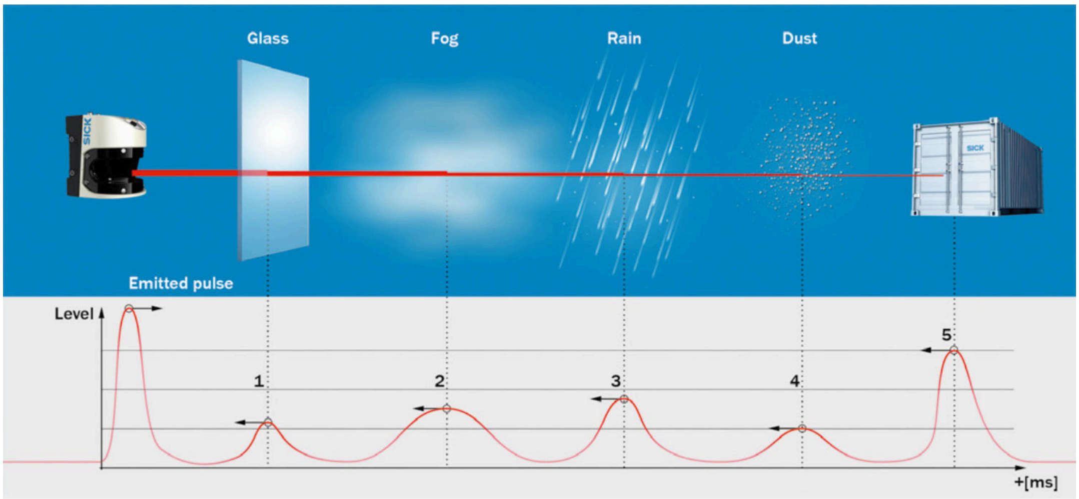

Figure 3.5: The SICK LMS 511 PRO can measure up to five echo's making the laser measurement less dependent on weather conditions [32].

Table 3.2: LMS 511 PRO LRF specifications [32]

Feature	Value	Unit	Comment
Field of view	190	°	adjustable
Angular resolution	0.1667/0.25/0.333/0.5/0.667/1	°	
Operating range	0 - 80	m	
Max. range	40	m	with 10% reflectivity
Accuracy	±25	mm	at 1 – 10 m
	±35	mm	at 10 – 20 m
	±50	mm	at 20 – 30 m
Data output rate	25/35/50/75/100	Hz	
Timing	≥ 10	ms	response time
Price	5,000	€	

3.3. Inertial Measurement Unit

To measure roll in the LRU an extra sensor is required. this sensor should be able to accurately measure roll. This extra sensor could add more measurement information when combining both sensor data, this is often referred to as *sensor or data fusion*. Sensor fusion of IMU sensors is often done with a Kalman filter [5, 28]. With sensor fusion a less accurate roll sensor could be used than required. Selecting a sensor that measures all six DoF's could improve the measured vessel motions of the LRU.

An overview of some of the currently available sensors is shown in table 3.3. To keep the ability to use the system for more then 4 DoF's for other applications a sensor that can measure in three axis is chosen. The field of Micro-Electro-Mechanical Systems (MEMS) IMU's is rapidly improving, these chips combine accelerometers and gyroscopes to measure the orientation and accelerations of the sensor. These MEMS IMU's are used in large quantity applications like: smartphones and the automotive industry. Due to the manufacturing procedure large quantity's can be produced making these MEMS IMU's very affordable. The downside is that these sensors are more sensitive to noise than the more expensive IMU sensors. Due to the sensor fusion the performance of the system is dependent on both sensor systems; the IMU provides a fast and rough measurement that gets updated using the slower but accurate LRF measurement. For the LRU the Bosch BNO055 MEMS IMU is chosen, this is a System in Package (SiP) that combines a accelerometer, gyroscope, magnetometer and micro-controller in a single package [4].

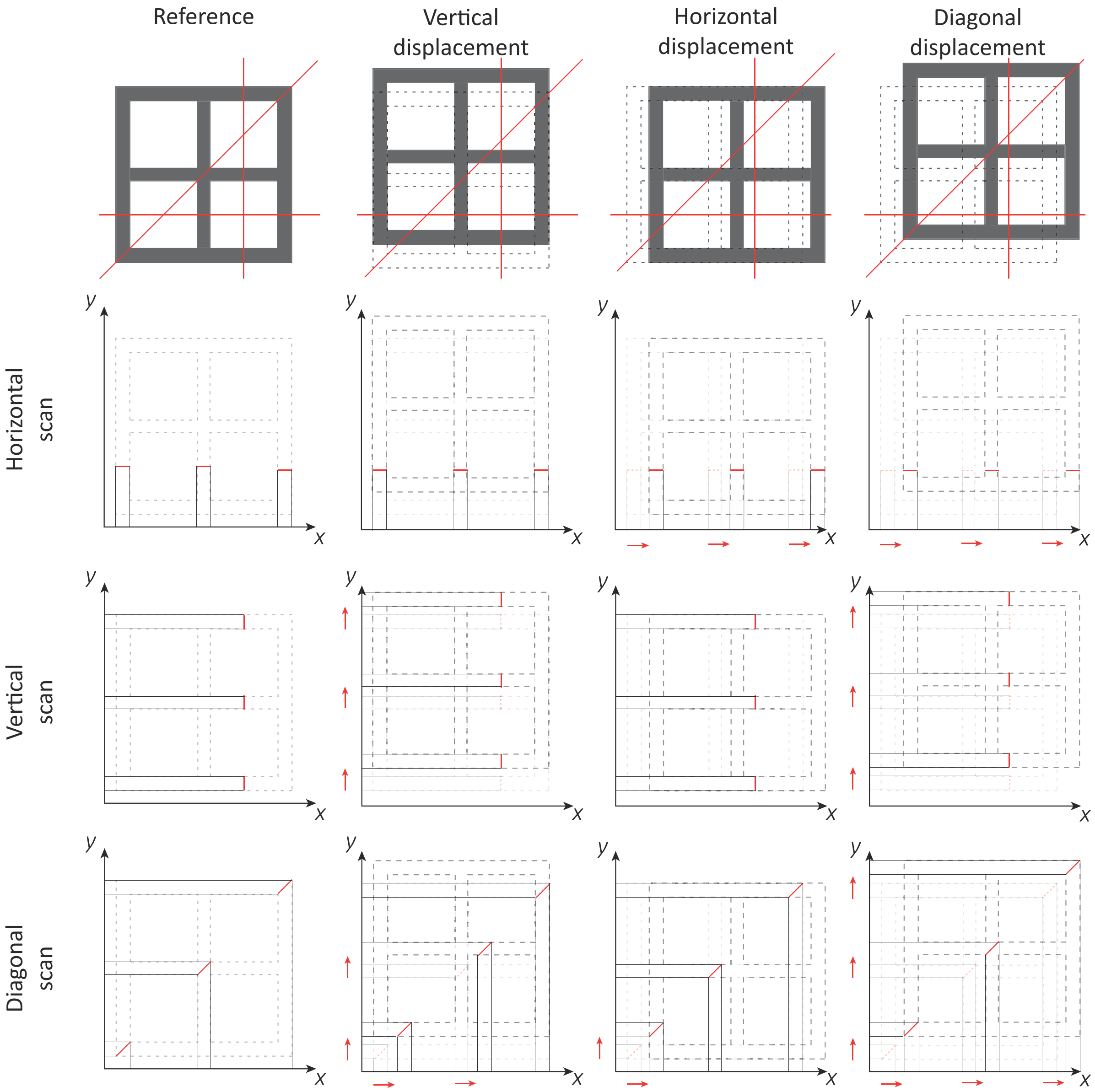
Reference
Vertical displacement
Horizontal displacement
Diagonal displacement
Horizontal scan
Vertical scan
Diagonal scan
y
x

Figure 3.6: 2D example of three scanner orientations: horizontal, vertical and diagonal scan orientations. The red lines indicate the scan lines and the red arrow indicate the motions on the x, y-axis of the different orientations.

3.3.1. BNO055

The Bosch BNO055 is an intelligent absolute orientation sensor that combines an tri-axial accelerometer, tri-axial Gyroscope and tri-axial geomagnetic sensor with a integrated micro-controller for sensor fusion in one package. This sensor fusion calculates the orientation of the IMU by means of Euler angles and the linear accelerations. Tests done by Ampelmann using the SBG Ekinox, which also uses a tri-axial geomagnetic sensor, when the magnetic field of the earth as an absolute reference, showed that the magnetic field on a steel vessel could not be used as reference. The Bosch BNO055 can also act as an IMU without using the information of the geomagnetic sensor.

Table 3.3: overview of roll sensor specifications.

Manufacturer	**Model**	**Axis** [#]	**Range** [°]	**Resolution** [°]	**Accuracy** [°]	**Output rate** [Hz]	**Orientation computated on-chip**	**Price** [€]
Vectornav	VN-100 [39]	3	±180	< 0.05	1.0	400	yes	750
LORD	3DM-GQ4-45 [21]	3	360	< 0.01	0.1	500	yes	
LORD	3DM-GX3-25 [22]	3	360	< 0.1	±2.0	1000	yes	
x-io Tech.	x-IMU [37]	3				512	yes	285
BOSCH	BNO055 [4]	3	360	14 bit	±4%	100	yes	35
InvenSense	GY-85 [13]	3	360	10 bit		1000	no	8
SignalQuest	SQ-GIX-0200 [34]	2	360	0.1	0.5	100	yes	
Kongsberg	MRU2 [19]	2	±25	0.001	0.1	200	yes	
Level Dev.	HPS-30 [8]	1	±30	0.001	0.1	16	yes	207
Level Dev.	LCH-A-S [9]	1	±180	0.05	0.05	inf.	no	48
Level Dev.	MAS-360-HA [10]	1	±180	0.01	0.2	40	no	
Level Dev.	SOLAR-30 [11]	2	±30	0.001	0.1	16	no	130

4

Algorithm

A large number of studies is done in the field localization and mapping. In the world of robotics this is usually referred to as Simultaneous Localization and Mappaing (SLAM), where it is used to determine the location of the robot in a world (localization) and building a map containing information of this world (mapping) at the same time (simultaneous). All research is done in the field of computer vision, as a computer cannot interpret the world around it with the same information we gather with our eyes. This chapter will explain research done in areas of robotics and autonomous vehicles. This knowledge is used to determine the best algorithm used for this research. At the end of this chapter the algorithms used to measure the vessel motions are explained.

4.1. Process Approach

To go from a point cloud as generated by the LRF to motion sensing with an absolute reference requires a application bounded algorithm. The motion is extracted by comparing scan data to a reference set of scan data. usually this reference set of scan data is the point cloud from the first scan. If the scan frequency is high enough the motion can be extracted by calculating the differences between scans and the reference scan with an fast algorithm. The approach for defining all individual process steps is shown in figure 4.1.

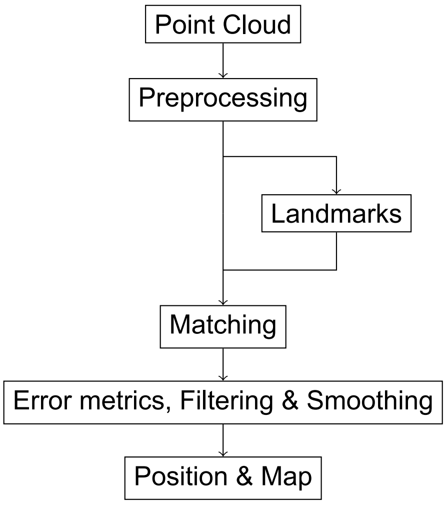

Figure 4.1: Process approach for an algorithm to go from a point cloud to motion measurement, using computer vision.

In the preprocessing part the LRF data is imported and converted to logical points with Cartesian coordinates. During the preprocessing process unwanted data could also be removed. After this step one could chose to make their algorithm work with the complete point cloud data set or try to reduce the amount of data points in the point cloud by finding recurring elements in a scan. These elements have a mathematical geometric property that makes it possible to find them in computer vision. These recurring points are called landmarks. The displacements are calculated during the matching step. New scans are compared with the first and previous scans to calculate the motions. If there is noise in the measurement or other disturbances, filtering and smoothing could be applied during the error metrics phase of the algorithm. For the LRU the filtering is also used to combine the measurement data of both sensor systems. This complete process results in the localization and motion measurement.

An exploded view of the process approach based on literature is found in figure 4.7. The mentioned techniques are briefly discussed in the next subsections. The algorithms used for the LRU are selected and explained in section 4.2.

4.1.1. Preprocessing

The communication between the LRF and the computer or Programmable Logic Controller (PLC) is via Ethernet. After each scan the data is sent in one packet. This data has to be translated to x, y positions of the measured points. The SICK LMS LRF can scan up to an angle of $190°$ with intervals of $0.167°, 0.25°, 0.0.333°, 0.5°, 0.667°$ and $1°$ and up till a distance of 80 m. Only the scan points of the target are interesting to use in the algorithm. Therefore the measurement angle of the LRF can be adjusted to only scan the area of interest. This can be done with a so called bounding box. This bounding box can alter the scan angle or could just delete measurement points that are outside the the area of interest. The bounding box can be predefined by the user and stay the same size during the measurement, in this case it is a static bounding box. During the scan the vessel and therefore the LRF moves. If the algorithm is already measuring the motions, the data could be used to move or adjust the bounding box as well. In this last case a dynamic bounding box is applied in the prepossessing process.

4.1.2. Landmarks

Most SLAM algorithms are more computationally efficient or have a certain limit when the amount of measurement points decreases [38]. Furthermore it becomes easier to match points using principles like nearest neighbour if the different points are further apart then their displacement is in consecutive scans. In computer vision these points are called landmarks. A Landmark is a natural or artificial feature that stands out from its environment. In the case of an offshore platform landmarks could be: lines, corners, edges, rectangles and poles. The features of different algorithms for marker-less landmark detection from literature are briefly discussed next. Since landmarks remove unwanted scan points, one of the landmark detection algorithms to be used in the algorithm for the LRU is selected.

Random Sampling Consensus

RANdom SAmple Consesnsus (RANSAC) is an algorithm that is used for robust model fitting if the data set contains a lot of outliers. Outliers are measurement points introduced by noise or measurement points that are outside the model preferred to measure. RANSAC can fit any model but it is mainly used to find lines, curves, planes, and shapes [14, 18, 20, 24, 27]. The RANSAC algorithm is proven to be a robust algorithm that can be adjusted to work with different shapes.

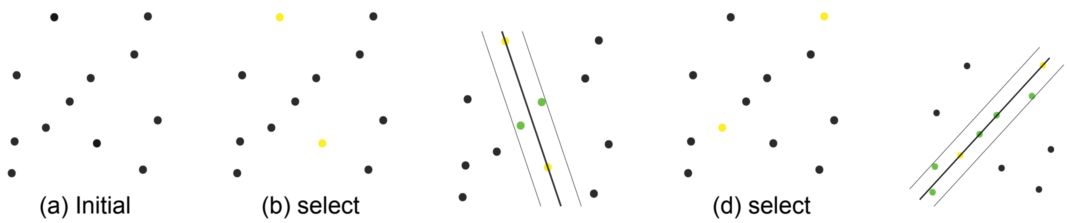
(a) Initial state. (b) select points. (c) inlier’s. (d) select points. (e) inlier’s.

Figure 4.2: The RANSAC algorithm illustrated. the initial point cloud is illustrated in (a), two points are randomly selected in (b) a line is drawn through these points and the distance from this line to the other points is computed, below a set limit these points become inlier’s in (c). If the line consists of enough inlier’s the line is recomputed using the inlier’s. In (d) and (e) two different points are selected resulting in the correct line detection.

In figure 4.2 the RANSAC algorithm is illustrated on a 2D example point cloud, figure 4.2a. In figure 4.2b two points are randomly selected from the point cloud. A virtual line is drawn trough these points and the perpendicular distance from the line to the remaining points is computed, if this distance is smaller then the user defined value, these points become inlier's, figure 4.2c and figure 4.2e. If this line consists of enough inlier's the line parameter will be recomputed using the inlier's, if there are not enough inlier's two new random points will be selected as shown in figure 4.2d and figure 4.2e where the found line is computed and a good line fit is found.

Point Cloud Shape Detection
In the previous landmark detection algorithm RANSAC is used for 2D line and arc fitting. The approach can also be used for 3D shape fitting [31]. Using this approach allows for the detection of for example: cylinders, boxes, spheres and planes. To correctly detect these shapes a dense or high resolution point cloud is required in a 3D space. The RANSAC algorithm does an excellent job at finding these shapes but does require more computing power than for a 2D line or arc detection. The point cloud shape detection is used in an offline environment where the time required by the algorithm plays no important role. Furthermore the LRF scanner combination does not provide a full 3-Dimensional (3D) point cloud.

Inscribed Angle Variance
Inscribed Angle Variance (IAV) is a recursive line fitting method to detect arc's/circles. It is developed for real-time detection of human legs [46]. The technique uses trigonometric features of an arc, all points in an arc have angles with equal values, congruent angles, with respect to the extremes. An example is shown in figure 4.3. The detection of circles is achieved by by calculating the average and standard deviation of the inscribed angles, with a standard deviation of $8.6°$ and average values between $90°$ and $135°$

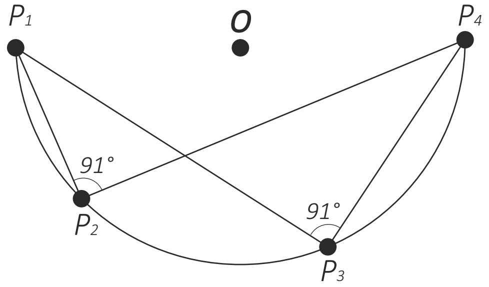

Figure 4.3: inscribed angles, with respect to the extremes(P_1, P_4), of an arc are congruent [46].

Range segmentation is used to produce clusters of consecutive scan points. The distance between consecutive points is calculated and if this is below a given threshold the scan points belong to the same cluster. These clusters are used to find the arcs.

Geometric Invariance
This algorithm works with the polar coordinate system to detect line segments in a scan. This preserves measurement noise statistics and the efficiency only depends of the angular resolution [25], as a LRF sensor delivers polar measurements. A line is described with two measurement parameters: the orthogonal distance to the sensor ρ_d and the related bearing θ_d. each point $P_i = (\rho_i, \theta_i)$ belonging to a line verifies the polar equation: $\rho_d = \rho_i \cos(\theta_d - \theta_i)$. The geometric invariant that only depends on the sensor parameter is the angular resolution α. The angular relation can now be expressed by: $\theta_j = \theta_i + \alpha(j - i)$ where i and j define measurement numbers in the same scan. This is used to define points that are on the same line in a scan. Probabilistic's are used to deal with noise in the measurement.

Concluding Remarks on Landmarks
There are multiple solutions to let a computer interpreted point cloud data and find different shapes that stand out from their surroundings. The detection of landmarks removes a lot of data points that are not necessary for a good match and make it easier to remove noisy data produced by the LRF or by other noise factors, for example a human walking around the scan target. people walking around on the scan target is an issue that will occur during the operation of the LRU. To avoid difficulties

concerning the movement on the scan target the choice is made to incorporate a landmark detection. The RANSAC algorithm is commonly used in the field of robotics and autonomous driving, the algorithm can be adjusted to detect certain shapes. Offshore structures contain mostly lines and arcs as shown in figure 4.10. The choice is made to incorporate a RANSAC landmark detection in the algorithm for the LRU to improve the robustness by avoiding unwanted scan points on the target platform.

4.1.3. Matching

At the heart of the motion, position and orientation measurement is the matching algorithm. This part of algorithm compares the measurement scan point cloud with the reference point cloud and tries to match these point clouds calculating the translations and rotations between them. In this section different matching algorithms from literature are explained and a choice is made for the matching algorithm used in the algorithm for the LRU.

Grid

A very basic matching algorithm is based on a grid that is applied over to the point cloud coordinate system. The number of points inside the cells of the grid are counted for the reference and the measurement scan. A histogram can be used to compare the grid information and a match is done based on the number of points in the locations of the grid. A simple example of the grid matching algorithm is illustrated in figure 4.4. The resolution of the match depends on the cell size of the grid.

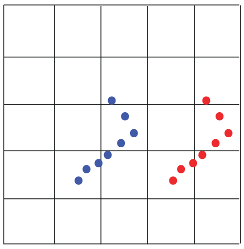

Figure 4.4: The grid matching algorithm. The reference point cloud in red and the scan to be matched in blue.

Iterative Closest Point

Iterative Closest Point (ICP) is a matching algorithm that works on entire point clouds but also work on reduces point clouds. The algorithm is illustrated in figure 4.5. The algorithm compares a scan point cloud to a reference point cloud and calculates the closest points from the scan point cloud to the reference point cloud and uses this information to transform the scan point cloud. This operations is repeated until the error is smaller than the given threshold ϵ, as described in figure 4.5.

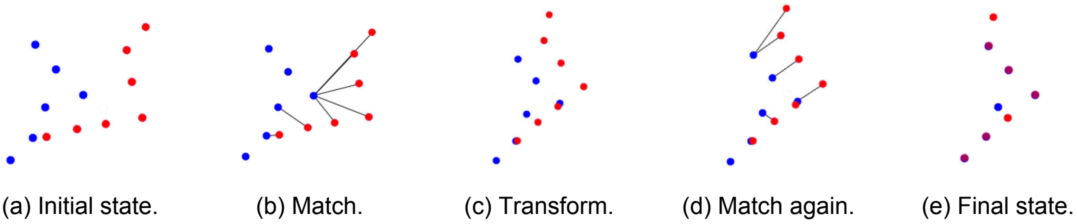

(a) Initial state. (b) Match. (c) Transform. (d) Match again. (e) Final state.

Figure 4.5: The ICP algorithm [7].

This algorithm can get stuck in a local minimum and in recent years the ICP algorithm is expanded using RANSAC and extended Kalman filtering to overcome this problem. To get a robust matching algorithm it is important to tune the parameters of the ICP algorithm correctly for the measurement situation and add filtering [7].

Corresponding Vector Fitting SAmpling Consensus

Corresponding Vector Fitting SAmpling Concensus (CVFSAC) is a matching algorithm based on the RANSAC algorithm for landmark detection. The algorithm uses raw data from the LRF and does not require any model information [18]. A corresponding vector pair is a point in both scans that lies on the same location in the world while the scanner has moved. When this point is found the tangential angle vectors are calculated and used to transform the scan point cloud, as illustrated in figure 4.6.

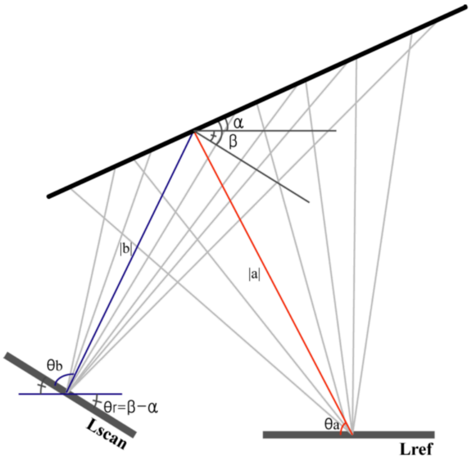

Figure 4.6: The CVFSAC algorithm [18]

The tangential angles α, β are determined using the next points in the point cloud. The transformation parameters are: $x = |a|\cos\theta_a - |b|\cos(\theta_b - \theta_r)$, $y = |a|\sin\theta_a - |b|sin(\theta_b - \theta_r)$ with $\theta_r = \beta - \alpha$. The pseudo code is found in algorithm 1. The algorithm leaves room for some error that is removed with the ICP algorithm.

Algorithm 1 CVFSAC

```
procedure cvfsac algorithm($pts, pts_{ref}, iterNum, threshold$)
    calculate the tangential angle vectors of each element in $pts$ and $pts_{ref}$
    for $p = 1 : iterNum$ do
        Randomly select two vector elements from each scan data $pts$ and $pts_{ref}$
        Estimate the transformation from the two selected vectors
        Transform $pts$
        calculate matching score from transformed $pts$ and $pts_{ref}$ by consensus ranking system
        if ranking score > $threshold$ then
            store transformation
        end if
    end for
    Find best transformation
    return translations and rotation
end procedure
```

Nearest Neighbour

Nearest neighbour is a basic matching algorithm. The principle is that for each point in the scan point cloud the closest point in the reference scan is computed. This closest point search is based on euclidean distance in a 2- or 3-D space [27]. An example is shown in figure 4.5b of the iterative closest point algorithm. This matching approach on its own is only used with landmarks instead of full point clouds. due to the fact that landmarks are further apart from each other and therefore more distinct, the chance of a mismatch between two scans is less likely. The fact that there are no additional steps in the algorithm to prevent any mismatching, nearest neighbour is used in multiple matching algorithms as one of the matching steps and not as a matching algorithm on its own.

Concluding Remarks on Matching

The Grid and neighbour algorithms are only suitable for certain situations, for this reason they are not as robust as the competition. The precision of the match, is due to the non iterative process, less accurate as can be achieved with ICP, on the other hand the chance of converging to local minimum/maximum could still occur for all three algorithms. The CVFSAC has only proven itself in research once instead of the ICP algorithm whit a more extensive research history. The ICP algorithm works on full point clouds but works better due to the fact of the nearest neighbour search if the points in the cloud are more spread out by means of landmarks. The choice for the matching part in the algorithm for the LRU is the ICP matching algorithm.

4.1.4. Filtering

After matching the measurement scans to the reference scan, the output motion must be filtered and fused with the measurement data from the IMU. This part of the algorithm is going to fuse the sensor data and produce a smoother and more accurate motion output than a non-filtered or single sensor motion measurement. Due to the complexity of the different filter algorithm only basic information about the filter is given in this section. This information is used to determine the choice of filter used in the in the algorithm for the LRU. The chosen filter will be explained in detail in section 4.5 where the chosen filter algorithm for the LRU is explained in depth.

(Extended) Kalman Filter

In point cloud algorithms the Extended Kalman Filter (EKF) is a commonly used filter, the EKF is based the Kalman Filter and extended to cope with non-linearity. The Kalman filter is a model based filter meaning that it relies on a model of the motion system. This model data is used to predict the next position in time. This prediction is than updated with the measurement data and corrected. The filter supports estimations of present, past and even future states of the system. The filter only requires the current and previous position and can therefore be used to filter and fuse the data online [27, 38, 44].

(Extended) Information Form

Extended Information Form (EIF) is a batch mapping filter that maintains a information matrix instead of the common covariance matrix used in the Kalman filter. The fact that this filter only works with batches of measurement information and can not be used online. The EIF is not a suitable filter for the algorithm of the LRU [38].

Sparse (Extended) Information Filter

in the Sparse Extended Information Filter (SEIF) algorithm the sparsity of the information matrix is used to create an online filter. Both the EIF and SEIF are SLAM filters used in large environments, for example on cars that ride around town. A lot of landmarks need to be added along the ride. The Kalman filter, due to the fact that its covariance matrix grows quadratic with respect to the size of the map, in practice can only cope with maps containing a couple hundred of features [38]. For the LRU which will only scan a single target this is not a problem.

Fast Incremental Mapping

The Fast Incremental Mapping (FIM) algorithm is able to generate maps in near real-time while simultaneously coping with the data association problem of the previous discussed filters. In comparison to the EKF, EIF and SEIF filters, which are all based on a probabilistic core, the FIM algorithm is based on a non-probabilistic core. The downside of the FIM algorithm for the LRU is that the core of the algorithm can not cope with cyclic environments [38]. The motion a vessel will make during transfer operation will encounter these cyclic motions and pass the same point with respect to the target platform multiple times.

Concluding Remarks on Filtering

For the LRU a filtering algorithm is required that does not have to cope with large environments and is able to work online to accurately determine the vessels current position. When the vessel is in position for people transfer the motions of the vessel induced by waves are cyclic. The Kalman filter is able to deliver on these points and has proven itself on more occasions than the other filters and is therefore chosen to be used in the algorithm for the LRU.

The different algorithm process steps discussed in this section are shown in figure 4.7. The chosen process approach is highlighted by the thick line. In the next section this chosen process approach is explained in depth.

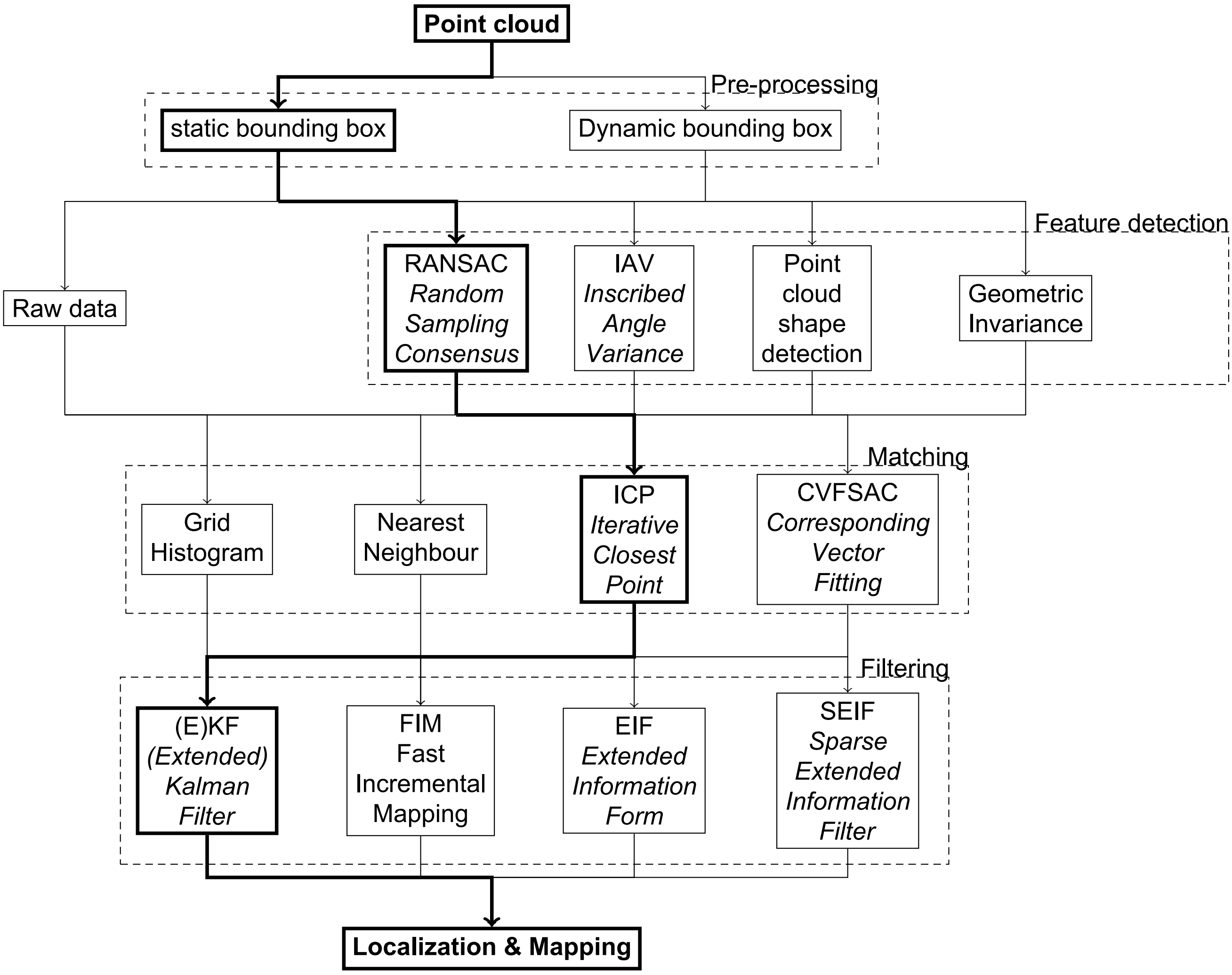
Point cloud
Pre-processing
static bounding box
Dynamic bounding box
Feature detection
Raw data
RANSAC
Random
Sampling
Consensus
IAV
Inscribed
Angle
Variance
Point
cloud
shape
detection
Geometric
Invariance
Matching
Grid
Histogram
Nearest
Neighbour
ICP
Iterative
Closest
Point
CVFSAC
Corresponding
Vector
Fitting
Filtering
(E)KF
(Extended)
Kalman
Filter
FIM
Fast
Incremental
Mapping
EIF
Extended
Information
Form
SEIF
Sparse
Extended
Information
Filter
Localization & Mapping

Figure 4.7: An overview based on different research done in the field of point cloud localization and mapping. The chosen algorithm items for the LRU are represented with a thick border/line.

4.2. Motion Extraction Algorithm

The working principles of the algorithm proposed for the LRU are explained in this section. A chronological order from raw LRF scan and IMU data is used to explain the steps. In this section the same route, from point cloud to localization and mapping, is followed as illustrated by the thick line in figure 4.7.

4.2.1. Point Cloud

The LRF produces a 2D point cloud of a planar scan. The user can define the scan resolution and scan angle, respectively between $0.1667° - 1°$and $-5° - 185°$. To obtain the required resolution of $0.1667°$the scan frequency is set to 25 Hz. The LRF sends the scan data over Ethernet via Transmission Control Protocol (TCP). The measurement data is formatted by a begin and end angle, based on the chosen scan angle. The scan resolution is given and the data array containing all the measured distances of the points. This polar coordinate data is converted to a Cartesian coordinate system by means of the trigonometric functions:

$$x = r\cos\phi \tag{4.1}$$

$$y = r\sin\phi \tag{4.2}$$

where r is the distance from the LRF to the measured point and ϕ is the corresponding scanner angles for the points. This conversion is done for all the points in a single scan and the Cartesian coordinates per scan are stored in an array. A simple example scan of a pillar with a wall in the background scanned in the horizontal plane is shown in figure 4.8.

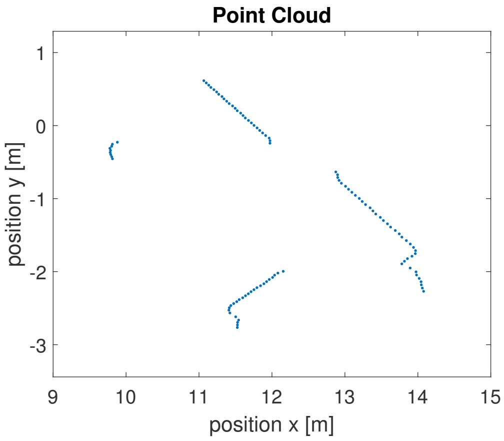

Figure 4.8: Point Cloud of a pillar with a wall in the background scanned with the SICK LMS 511 from a distance of 10 m. The Scanner is scanning in the horizontal plane and is placed in the origin $(0, 0)$ which is not shown in this plot.

4.2.2. Static Bounding Box

During people transfer operation the location of the vessel with respect to the target platform is reasonably well defined. During people transfer operation the distance to the target can vary between $6.5 - 11.5$m and the target platform is within a $\pm 45°$angle perpendicular to stern (aft or most backward point of the vessel). The LRF is able to scan larger distances and greater angles. To prevent unwanted measured points by objects not part of the target platform or noise points outside the mentioned area of the target platform use is made of static bounding box. A static bounding box is a user defined box, all points outside the box are discarded and only the measured points within the box are used in the algorithm. An example bounding box on the point cloud of the pillar is illustrated in figure 4.9.

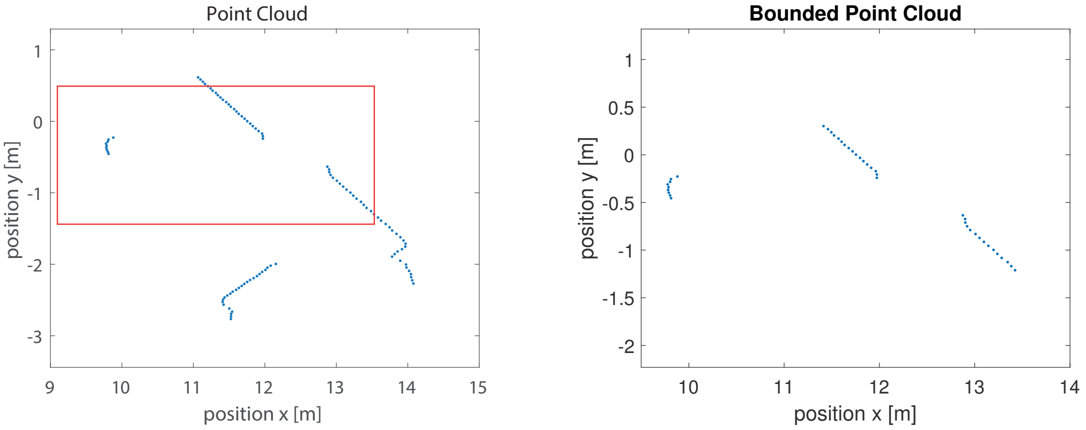

(a) Bounding box (b) Bounded point cloud

Figure 4.9: Illustration of a bounding box on the point cloud of a pillar with a wall in the background. In (a) the bounding box is shown in the original plot and in (b) the resulting point cloud,after discarding the points outside the bounding box

After an initial measurement the current vessel location with respect to target could be known from the measurement data, the bounding box could be made smaller. The bounding box could also be made dynamic by moving in the same way as the vessel during the people transfer operation. This dynamic bounding box is possible because the position of the vessel is updated every measurement moment in time. As a starting point only a static bounding box is used during the preprocessing phase in the algorithm.

4.3. Landmark Detection

The key robustness of the algorithm starts with landmark detection. To translate the point cloud data into vessel position the first scan is used as a reference scan. The next point clouds are then compared with the reference point cloud to determine the displacements and rotations between the two. This matching principle works best if in both point clouds only contain the same landmark measurement points. An offshore platform has a relative open structure but there are a lot of small obstacles, for example: stairs and rails, on these platforms as can be seen in figure 4.10. With the given scan resolution it is possible to scan such a railing in some of the measurement scans and not in others. Furthermore on the platform are machines and people moving. These moving parts and people on the target platform cannot be used during the matching of point clouds. Only the assumed static structure of the platform can be used for a robust motion sensing algorithm. Offshore platforms are mostly constructed with pillars connected to the sea floor. These pillars elevate different decks above sea level. When a horizontal and vertical planar scan are made from these platforms the distinctive shapes found are lines and arcs. The arcs are created by scanning the round pillars. The lines are created by the scanning of the decks and structures commonly placed on top of the platform decks. To use the lines and arcs as landmarks for the algorithm the scan points creating the landmarks need to be extracted from the full scan point cloud. This extraction is done with the help of the previously introduced RANSAC algorithm.

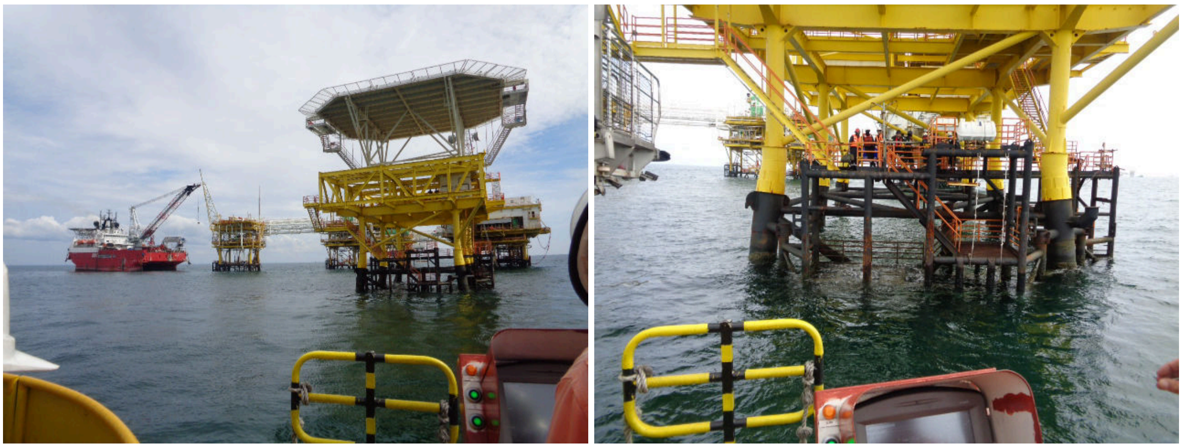

(a) Offshore platforms

(b) People transfer landing point

Figure 4.10: Pictures of platforms in the offshore fields of Asian Marine Professionals (AMPA) taken from a vessel with the older L-Type V3 on-board. (a) a cluster of platforms, (b) a close by picture off the people transfer landing point.

The basic steps in the RANSAC algorithm are already explained in section 4.1.2. An explanation on how the lines and arcs are defined within this algorithm can be found in this section. preliminary user defined variables like the number of iterations done, the inlier distance and the required amount of inlier's are also explained in this section. To avoid mismatching in a dynamic environment boundary conditions, for example: minimal or maximum line length, are implemented and explained.

4.3.1. Line Detection

The RANSAC line detection starts by randomly selecting two points from the points in the point cloud p_i, where i is the point number. A line is created using these two random points. A unit normal vector n of this line is constructed and used to calculate the euclidean distance $\mathrm{D_i}$ to the other points perpendicular to the line [36]:

$$\mathrm{n} = \frac{\mathrm{p}_2^r - \mathrm{p}_1^r}{|\mathrm{p}_2^r - \mathrm{p}_1^r|}, \quad \text{with} \quad \mathrm{p}_j^r = \begin{bmatrix} x_j \\ y_j \end{bmatrix} \quad \text{for } j = 1, 2 \tag{4.3}$$

$$\mathrm{D}_i = \mathrm{n}\left(\mathrm{p}_i - \mathrm{p}_{\mathrm{1V2}}^r\right) \tag{4.4}$$

where p_j^r indicate the random selected points and i is the point number of the points in the point cloud without the two randomly selected points by the RANSAC algorithm. For the distance calculation it does not matter which of the two random points is used in equation 4.4.

From this distance vector the inlier's are created by bounding the maximum allowed perpendicular distance that points may lay from the line named $thDist$. All measurement points within $thDist$ distance to the line become inlier's. If the number of inlier's is larger or equal then the user defined amount of required inlier's, called $thInlr$ then the line is stored.

This process is repeated with other non-identical randomly selected points until the user defined number of maximum loops is reached, named $iterNum$. All the stored lines are then compared and the line which consist of the most inlier's is selected and the begin and end points of the lines x, y-coordinates are returned with the corresponding inlier's. This process is shown in pseudo code in algorithm 2, here pts stands for the points in the point cloud.

Algorithm 2 RANSAC line [24]

```
procedure ransac line($pts, iterNum, thDist, thInl, maxLength$)
    for $p = 1 : iterNum$ do
        Choose sample of $2$ random points
        Fit a line through the $2$ points
        Compute the distances $d$ of other point to the line
        for $d < thDist$ do
            create set of inlier's $nInliers$
            if $nInliers > thInt$ then
                Store the line
            end if
        end for
    end for
    Find line with most inlier's and shorter than $maxLength$
    return line parameters $(X, Y)$ and inlier's
end procedure
```

In the algorithm for the LRU during testing and simulation the RANSAC line algorithm is repeated multiple times. In this repeated process the found line inlier's are removed from the point cloud during each consecutive line search and a reduced point cloud remains. This reduced point cloud is then used to find arcs in the point cloud, instead of the full point cloud. The result of the RANSAC line algorithm on the pillar example point cloud with settings: $iterNum = 30$, $thDist = 0.01$ m, $thInl = 10$ and $maxLength = 3$ m is shown in figure 4.11. A link to the Matlab code can be found in appendix A.1.

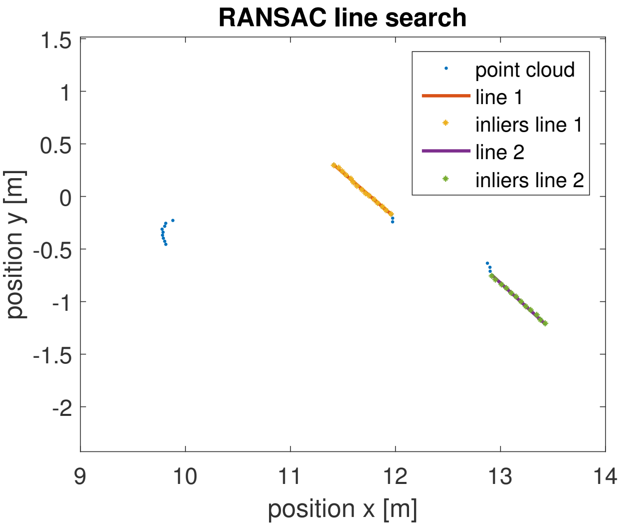

Figure 4.11: RANSAC line algorithm result on the bounded point cloud of a pillar with a wall in the background.

4.3.2. Arc Detection

The method to find arcs uses the same approach as the RANSAC line algorithm. The goal is to find the centre coordinates and the radius of the arc. To find an arc in a point cloud three points on the arc are required to determine the centre and radius. The algorithm starts by selecting three random points. The general quadratic equations of circle is used with these three points [36]:

$$(x_j^r - x_c)^2 + (y_j^r - x_c)^2 - r^2 = 0 \text{ with} j = 1..3 \tag{4.5}$$

by subtracting the second from the first and the third from the first two linear equations follow

$$(x_1 - x_c)^2 - (x_2 - x_c)^2 + (y_1 - y_c)^2 - (y_2 - y_c)^2 = 0 \tag{4.6}$$

$$(x_1 - x_c)^2 - (x_3 - xc)^2 + (y_1 - y_c)^2 - (y_3 - y_c)^2 = 0 \tag{4.7}$$

solving for the centre x_c, y_c results in.

$$x_c = \frac{{x_1}^2 y_2 - {x_1}^2 y_3 - {x_2}^2 y_1 + {x_2}^2 y_3 + {x_3}^2 y_1 - {x_3}^2 y_2 + {y_1}^2 y_2 - {y_1}^2 y_3 - y_1 {y_2}^2 + y_1 {y_3}^2 + {y_2}^2 y_3 - y_2 {y_3}^2}{2\,(x_1 y_2 - x_2 y_1 - x_1 y_3 + x_3 y_1 + x_2 y_3 - x_3 y_2)} \tag{4.8}$$

$$y_c = \frac{-{x_1}^2 x_2 + {x_1}^2 x_3 + x_1 {x_2}^2 - x_1 {x_3}^2 + x_1 {y_2}^2 - x_1 {y_3}^2 - {x_2}^2 x_3 + x_2 {x_3}^2 - x_2 {y_1}^2 + x_2 {y_3}^2 + x_3 {y_1}^2 - x_3 {y_2}^2}{2\,(x_1 y_2 - x_2 y_1 - x_1 y_3 + x_3 y_1 + x_2 y_3 - x_3 y_2)} \tag{4.9}$$

and the radius r is found by plugging in the values of the found arc centre in one of the three quadratic equations 4.5 and solving for r

$$r = \frac{1}{3} \sum_{j-1}^{3} \sqrt{(x_j - x_c)^2 + (y_j^r - x_c)} \tag{4.10}$$

To reduce the noise factor on the calculation of the radius of the arc, the radius is calculated using the mean of all three found radii on the random points.

The found arc must comply with the user defined boundary's implemented in the algorithm. these boundary's are the minimal and maximum radius of the arc named $minRadius$ and $maxRadius$. If the found arc complies with these boundary's the distance of the arc to the points in the point cloud is calculated:

$$\mathrm{D}_i = \sqrt{\mathrm{p}_i - \mathbf{c}^2} - r \text{ with } \mathrm{p}_i = \begin{bmatrix} x_i \\ y_i \end{bmatrix} \text{ and } \mathbf{c} = \begin{bmatrix} x_c \\ y_c \end{bmatrix} \tag{4.11}$$

Where i is the point number containing all the points in the point cloud except the random selected ones to construct the arc. The inlier's are determined. If the found arc consists of enough inlier's $thInl$ the arc is recomputed using all the inlier's. Small differences in point position caused by noise create a large difference in the arc's centre coordinates and radius. The boundary's on the radius of the arc are critical to detect smaller pillars and not for example the human body or legs. For this reason the arc parameters are recomputed with all the found inlier's. The recomputed arc parameters are again checked checked to comply with the set boundaries of the arc radius and, only if they comply, stored as an arc. Finally the arc with the most inlier's is returned by the algorithm. The pseudo code is shown in algorithm 3. A link to the MATLAB code can be found in appendix A.1.

In the algorithm for the LRU during testing and simulation the RANSAC arc algorithm is also repeated multiple times. In this repeated process the found arc inlier's are removed from the point cloud during each consecutive arc search and a reduced point cloud remains. The result of the RANSAC arc algorithm on the example point cloud with settings: $iterNum = 30$, $thDist = 0.005$ m, $thInl = 4$, $maxRadius = 0.2$ m and $minRadius = 0.15$ m is shown in figure 4.12.

In figure 4.12 it seems that perhaps not all the points should be found that are on the half-circle in the eye of sight of the LRF. To investigate if the case is that not all points are found by the LRF, a scan is made from a concrete pillar with a radius of 0.165 m from a distance of 2.2 m to the centre of the pillar. This is illustrated in figure 4.13, where the red lines are drawn from the origin of the LRF scanner to the far most top and bottom part of the pillar.

The number of scan points possible with the scan resolution of $0.1667°$and the amount of successive scan points on the pillar of 251 scans is compared. From this study is found that for 16% the difference

Algorithm 3 RANSAC arc

```
procedure ransac arc($pts, iterNum, thDist, thInl, minRadius, maxRadius$)
    for $p = 1 : iterNum$ do
        Choose sample of $3$ random points
        Fit a arc through the $3$ points
        Compute the distances $d$ of other point to the arc
        if $minRadius < r < MaxRadius$ then
            for $d < thDist$ do
                create set of inlier's $nInliers$
                if $nInliers > thInt$ then
                    Recompute the arc parameters
                    if $minRadius < r < MaxRadius$ then
                        Store the line
                    end if
                end if
            end for
        end if
    end for
    Find arc with most inlier's
    return Arc parameters ($c_x, c_y, r$) and inlier's
end procedure
```

is a single point less scanned than possible. There is no scan where more points are found by the scanner than possible on the pillar and no scans where the difference in points found is larger than one. Taking the total number of points scanned on the pillar and the number of missing points for all 251 scans into account results in the percentage of missed points by the LRF on the pillar of 0.32%. This is such a small amount that we can conclude that the LRF does find all the points on a pillar. Keep in mind when the scanner is further away from the pillar this percentage increases. Take the pillar in the example point cloud at a distance of 10 m the chance of finding one point less than possible on the pillar is 1.6%.

In figure 4.13 the pillar is standing in front of a wall that is not visible in the figure. Between the wall and the pillar some scan points that appear to be floating in mid air are visible. This is a known phenomenon with a LRF measurement system. This phenomenon occurs when the LRF hits two surfaces at the same time [43]. This situation is not difficult to achieve when scanning a circular pillar. At the most outer parts indicated by the red lines in figure 4.13 more light will be reflected towards the wall instead of back to the LRF. The RANSAC arc algorithm makes sure that these points are not taken into account during the matching part of the algorithm. These floating points are not used during matching as they are not part of the inlier point set created by the both RANSAC algorithms used during matching.

4.4. Matching Point Clouds

During matching the actual translations and rotations of the vessel are computed. The first scan made by the LRF is the reference scan called pts_{ref}. This reference scan is used to compare and match all successive scans called pts_{scan}. This matching is done in an iterative manner using the ICP algorithm. First a match is done where the scan point cloud is matched to the reference scan. The found rotations and translations are used to transform the measurement scan. After this transformation a new match an transformation is done until a user defined minimal error limit is reached or the number of maximum iterations is reached. This process is already illustrated in figure 4.5. In this section the methods used to match and transform the successive scans to obtain the current vessel position and orientation are explained.

4.4.1. Iterative Closest Point

Matching is based on the nearest neighbour principle. For al the scan points pts_{scan}, the nearest neighbour in the reference scan pts_{ref}, is computed as shown in figure 4.15a. This nearest neighbour

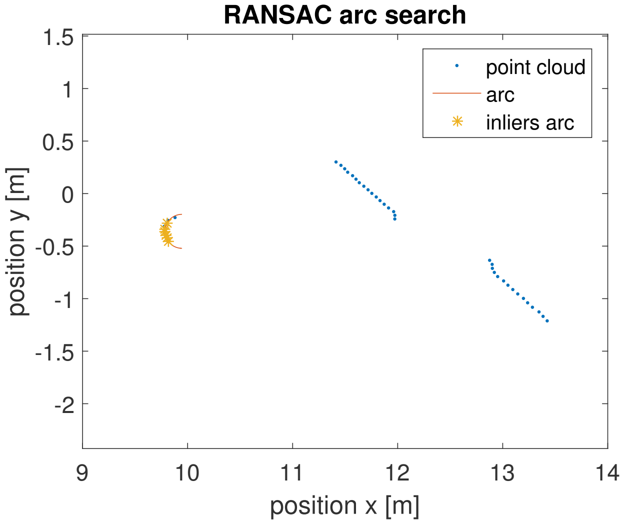

Figure 4.12: RANSAC arc algorithm result on the bounded point cloud of a pillar with a wall in the background.

search is based on euclidean distance. The mean of the distances, between the points in the two scans compared, squared is the residual in the algorithm. The found nearest neighbours in the reference scan are used to find the rigid body transformation. The process that searches for the optimal rotation and translation is done with Singular Value Decomposition (SVD). This process and the algorithm used are explained by Bergström and Edlund [2], Bergström et al. [3]. A summary of the steps provided by Sorkine-Hornung and Rabinovich [35] is explained in the next part of this section to get a better understanding of the ICP algorithm.

The goal is to find a rotation R and a translation T that minimizes the euclidean distances between the points of the reference scan $pts_{ref} = \mathrm{q}$ and the rotated and/or moved, due to vessel motions scan, later in time $pts_{scan} = \mathrm{p}$.

$$(\mathrm{R}, \mathrm{T}) = argmin \sum_{i=1}^{n} w_i \left\|(\mathrm{R}\mathrm{p}_i + \mathrm{t}) - \mathrm{q}_i\right\|^2, \ \ w_i > 0 \tag{4.12}$$

where w_i are the weights and n is the amount of points in the scan. q_i is filled with the same amount of points created by the nearest neighbour algorithm. This allows for the matching of point clouds consisting of a different amount of points. w_i is in this algorithm is set the same for every point. Next the centroids of both point clouds are calculated.

$$\bar{\mathrm{p}} = \frac{\sum_{i=1}^{n} w_i \mathrm{p}_i}{\sum_{i=1}^{n} w_i}, \quad \bar{\mathrm{q}} = \frac{\sum_{i=1}^{n} w_i \mathrm{q}_i}{\sum_{i=1}^{n} w_i} \tag{4.13}$$

with these centroids the centred vectors of the points are calculated

$$\mathbf{x}_i = \mathrm{p}_i - \bar{\mathrm{p}}, \quad \mathbf{y}_i = \mathrm{q}_i - \bar{\mathrm{q}}, \quad i = 1, 2, .., n. \tag{4.14}$$

With this information the $d \times d$ covariance matrix S is computed

$$\mathrm{S} = \mathrm{X}\mathrm{W}\mathrm{Y}^{\mathrm{T}} \tag{4.15}$$

where X and Y are the $d \times n$ matrices that have $\mathbf{x}_i$ and $\mathbf{y}_i$ as their columns, respectively. $\mathrm{W} = \mathrm{diag}\,(w_1, w_2, ..., w_n)$. Computing the SVD $\mathrm{S} = \mathrm{U}\Sigma\mathrm{V}^T$ is illustrated in figure 4.14. The rotation and optimal

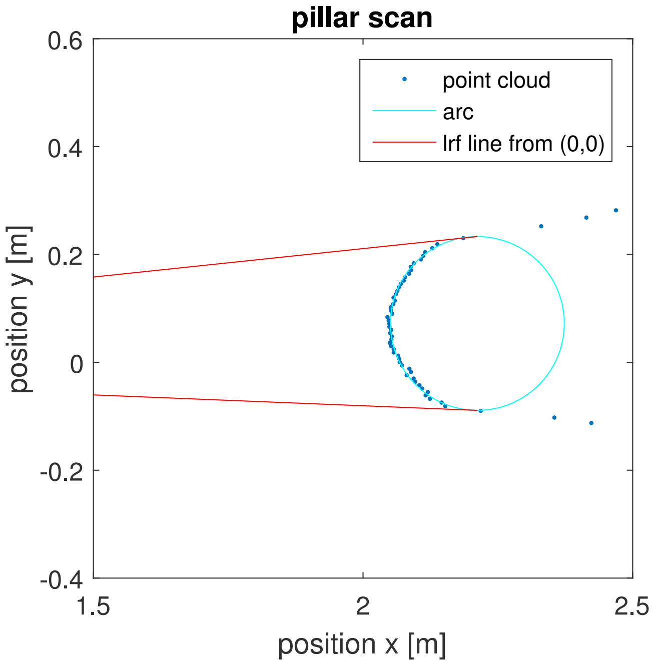

Figure 4.13: A scan by the LRF of a pillar from a distance of 2.2 m to the centre of the pillar. The red lines indicate the maximum line of sight of the LRF on part of the pillar.

translation can then be calculated.

$$R = V\begin{bmatrix} 1 & & & & & \\ & 1 & & & & \\ & & \cdot & & & \\ & & & \cdot & & \\ & & & & \cdot & \\ & & & & & 1 & \\ & & & & & & \det\left(VU^{T}\right) \end{bmatrix}, \quad t = \bar{q} - R\bar{p} \tag{4.16}$$

The found transformation is applied to the point cloud of pts_{scan}, as shown in figure 4.15b. The transformation data is stored. The nearest neighbour algorithm is recomputed to calculate the new residual.

Algorithm 4 ICP

```
procedure ICP($pts, pts_{ref}, maxIter, minIter, \epsilon$)
    while residual> $\epsilon$) AND ($maxIter \geq iterNum$) AND ($minIter \leq iterNum$) do
        for each point in $pts$ find closest point to $pts_{ref}$
        Estimate combination of rotation and translation using SVD
        Transform $pts$ with the found values in the previous step
        Calculate residual between $pts$ and $pts_{ref}$
    end while
end procedure
```

The previously explained process is repeated until the user defined maximum number of iterations is reached or the residual is smaller than the user defined value. The ICP algorithm returns the rotation R, translation T and transformed pts_{scan} point cloud. In figure 4.15 the first nearest neighbour search and transformation on the example pillar point cloud are shown. The pillar example point cloud pts_{scan} is rotated by $10°$counter clockwise around its centroid and translated 0.5 m in the positive x and y direction. The pseudo code of the ICP algorithm is shown in algorithm 4. The final result after all iterations is

---

[1] Georg-Johann, `https://commons.wikimedia.org/wiki/File:Singular-Value-Decomposition.svg`

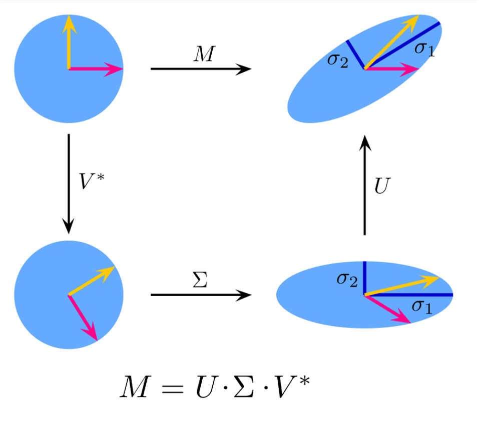

Figure 4.14: Illustration of the single value decomposition on a unit disk. The upper left shows the unit disc in blue together with the two canonical unit vectors. The upper right shows the action of M on the unit disc: it distorts the circle to an ellipse. The SVD decomposes M into three simple transformations: a rotation V^*, a scaling Σ along the coordinate axes and a second rotation U. The SVD reveals the lengths σ_1 respectively σ_2 of the semi-major axis respectively semi-minor axis of the ellipse; they are just the singular values which occur as diagonal elements of the scaling Σ. The rotation of the ellipse with respect to the coordinate axes is given by U [1].

shown in figure 4.15c. The settings for the ICP algorithm are: maximum allowed residual $\epsilon = 1e^{-5}$, minimal number of iterations $minIter = 1$ and the maximum amount of iterations $maxIter = 100$.

A problem with the ICP algorithm is that it does not find a good fit if landmarks disappear or extra landmarks are added. This result in a completely different centroid of the scan point cloud. The scan point cloud is rotated around the centroid to find the best match. Due to this shift in the centroid of the point cloud other matches than the correct one could be the result. In the main LRU algorithm this situation is avoided by setting boundary's on the ICP algorithm output displacements. If one of the displacements between two consecutive scans is larger than the user defined translation of 0.07 m then:

- A check is done on how many landmarks are found in the reference and scan point cloud.
- If there is a difference in the amount of lines or arcs found, the inlier's of only one of the two is used: If there is a difference in the amount of arcs in the current and the reference scan than only the inlier's of the lines are used from both scans for the matching algorithm.
- If the amount of lines and arcs both differ between the current and the reference scan the position of the last match is used.
- After this process the difference between the consecutive scans is rechecked. If the displacement is still larger than 0.07 m, then the position of the previous match is used and the LRF measurement data is not used in the update phase of the Kalman filter.

4.5. Sensor Fusion

To combine the information from both sensors in a efficient way a Kalman filter is used. The Kalman filter is a set of mathematical equations that provides an efficient computational means to estimate the state of a process, in a way that minimizes the mean of the squared error [44]. The filter supports estimations of past, present and even future states, even when the precise nature of the modelled system is unknown.

4.5.1. Kalman Filter

The kalman filter produces a probability of a predicted state, based on a user defined model of the system. And combines this with the the probability of the measurement state to produce a combined probability to correct the prediction state. This cycle is illustrated in figure 4.16 and the different steps of the process are explained below [5, 27, 38, 44].

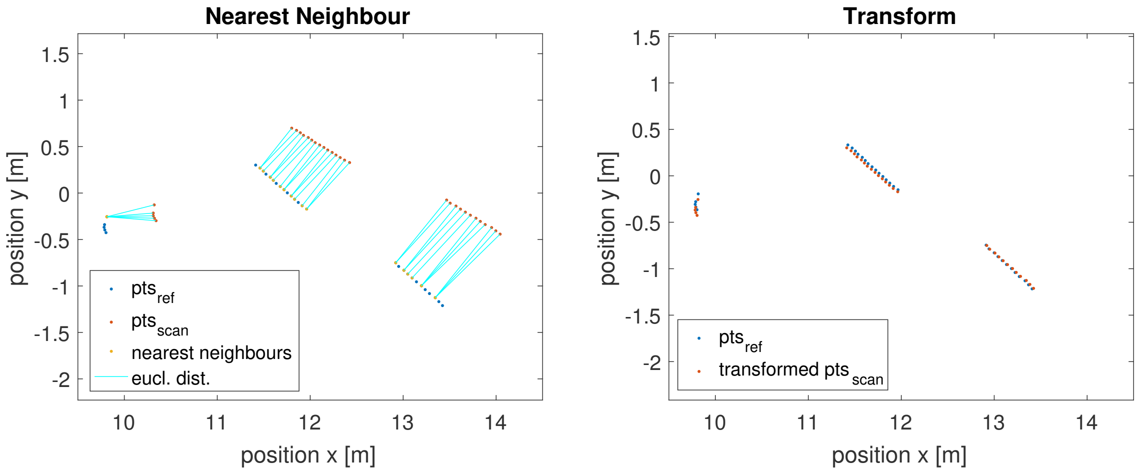

(a) first nearest neighbour search (b) first transformation

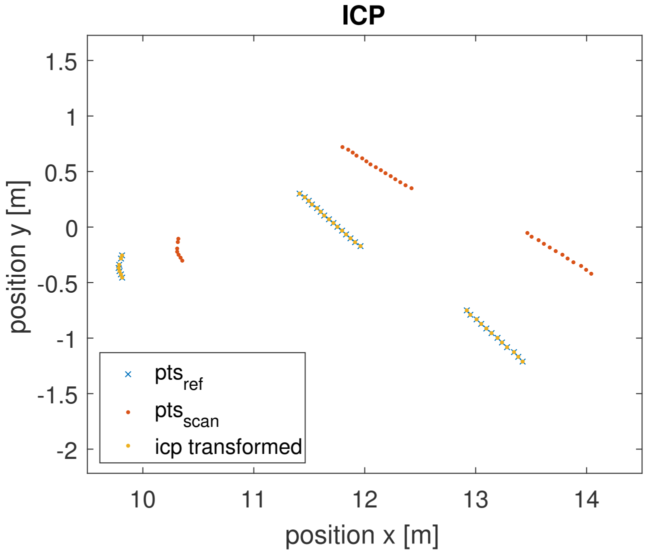

(c) The final result

Figure 4.15: Iterative closest point algorithm on the example pillar point cloud. The pts_{scan} point cloud is rotated by $10°$counter clockwise around the centroid and translated 0.5 m in the positive x and y direction. In (a) the nearest neighbours in the first iteration step are computed. In (b) the result of the first iteration step transformation are shown. In (c) the final result after matching and transforming is shown, the transformed points lay on top of the reference points.

The Kalman filter tries to estimate the state $\mathrm{x}_k \in \mathbb{R}^n$ of a discrete-time linear stochastic difference equation for each time step k:

$$\mathrm{x}_k = \mathrm{A}\mathrm{x}_{k-1} + \mathrm{B}\mathrm{u}_k + \mathrm{w}_k \tag{4.17}$$

where

- A is the state transition model, which is applied to the previous state x_{k-1}
- B is the control-input model which is applied to the control vector u_k
- w is a sequence of zero mean white gaussian system noise of assumed known covariance matrix Q_k

For each time step a measurement $\mathrm{z}_k \in \mathbb{R}^n$ of the true state x_k is made described as:

$$\mathrm{z}_k = \mathrm{H}\mathrm{x}_k + \mathrm{v}_k \tag{4.18}$$

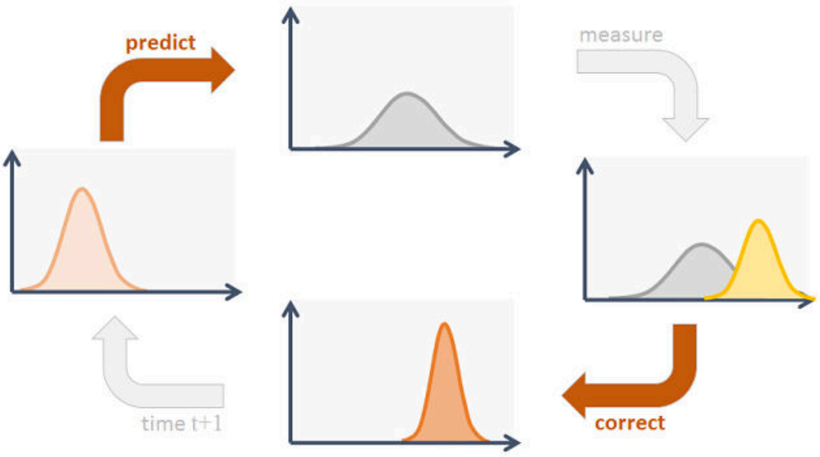

Figure 4.16: What the Kalman filter does is propagating and updating Gaussian's and updating their covariances. First the next state is predicted from the provided state transition, then the (noisy) measurement information is incorporated in the correction phase [17].

- where H is the observation model mapping the state space into observed space
- v_k is a sequence of zero mean white gaussian measurement noise of assumed known covariance matrix R_k

The Kalman filter uses a form of feedback control to estimate the process: the filter estimates the process state at some time and obtains feedback in the form of measurement. The Kalman filter equations therefore fall in two stages: the predict stage and the update (measurement) stage.

The state estimates are given as $\hat{\mathrm{x}}_{k|k-1} \in \mathbb{R}^n$ the a priori state estimate at time step k given knowledge of the proces prior to time step k. $\hat{\mathrm{x}}_{k|k} \in \mathbb{R}^n$ is the posterior state estimate at time step k given measurement z_k. The a priori and a posteriori errors are defined now defined as:

$$\mathrm{e}_{k|k-1} = \mathrm{x}_k - \hat{\mathrm{x}}_{k|k-1} \text{ and } \mathrm{e}_{k|k} = \mathrm{x}_k - \hat{\mathrm{x}}_{k|k} \tag{4.19}$$

which result in the a priori and a posteriori estimate error covariance

$$\mathrm{P}_{k|k-1} = \mathrm{E}\left[\mathrm{e}_{k|k-1} \quad \mathrm{e}^{\mathrm{T}}_{k|k-1}\right] \text{ and } \mathrm{P}_{k|k} = \mathrm{E}\left[\mathrm{e}_{k|k} \quad \mathrm{e}^{\mathrm{T}}_{k|k}\right] \tag{4.20}$$

where $\mathrm{E}[\epsilon]$ is the expected value of ϵ.

The equation to find the a posteriori state estimate $\hat{\mathrm{x}}_{k|k}$ for the Kalman filter is given by

$$\hat{\mathrm{x}}_{k|k} = \hat{\mathrm{x}}_{k|k-1} + \mathrm{K}_k \left(\mathrm{z}_k - \mathrm{H}\hat{\mathrm{x}}_{k|k-1}\right) \tag{4.21}$$

It describes a linear combination of the a priori estimate $\hat{\mathrm{x}}_{k|k-1}$ and a weighted K difference $\left(\mathrm{z}_k - \mathrm{H}\hat{\mathrm{x}}_{k|k-1}\right)$ between the actual measurement z_k and the measurement prediction $\mathrm{H}\hat{\mathrm{x}}_{k|k-1}$. This difference is called the measurement innovation or residual. K is the Kalman gain it is chosen to minimize the a posteriori error covariance $\mathrm{P}_{k|k}$. This is achieved by substituting equation 4.21 into the definition for e_k 4.19 and substituting the result in equation 4.19. Resulting in [44]

$$\mathrm{K}_k = \mathrm{P}_{k|k-1}\mathrm{H}^{\mathrm{T}} \left(\mathrm{H}\mathrm{P}_{k|k-1}\mathrm{H} + \mathrm{R}_k\right)^{-1} \tag{4.22}$$

If the measurement error covariance R_k approaches zero the Kalman gain will increase and the residual will be weight more heavily. If the a priori estimate error covariance $\mathrm{P}_{k|k-1}$ approaches zero the Kalman gain will decrease and the residual is weight less heavily.

The cycle of the Kalman filter including the equations and input/output is illustrated in figure 4.17.

4.6. LRF and IMU Data Fusion

To fuse the measurement data with the Kalman filter the state transition and measurement or observation model need to be defined by the user. these will map the state and measurement information to the correct states and produce the prediction with the state from the previous time step.

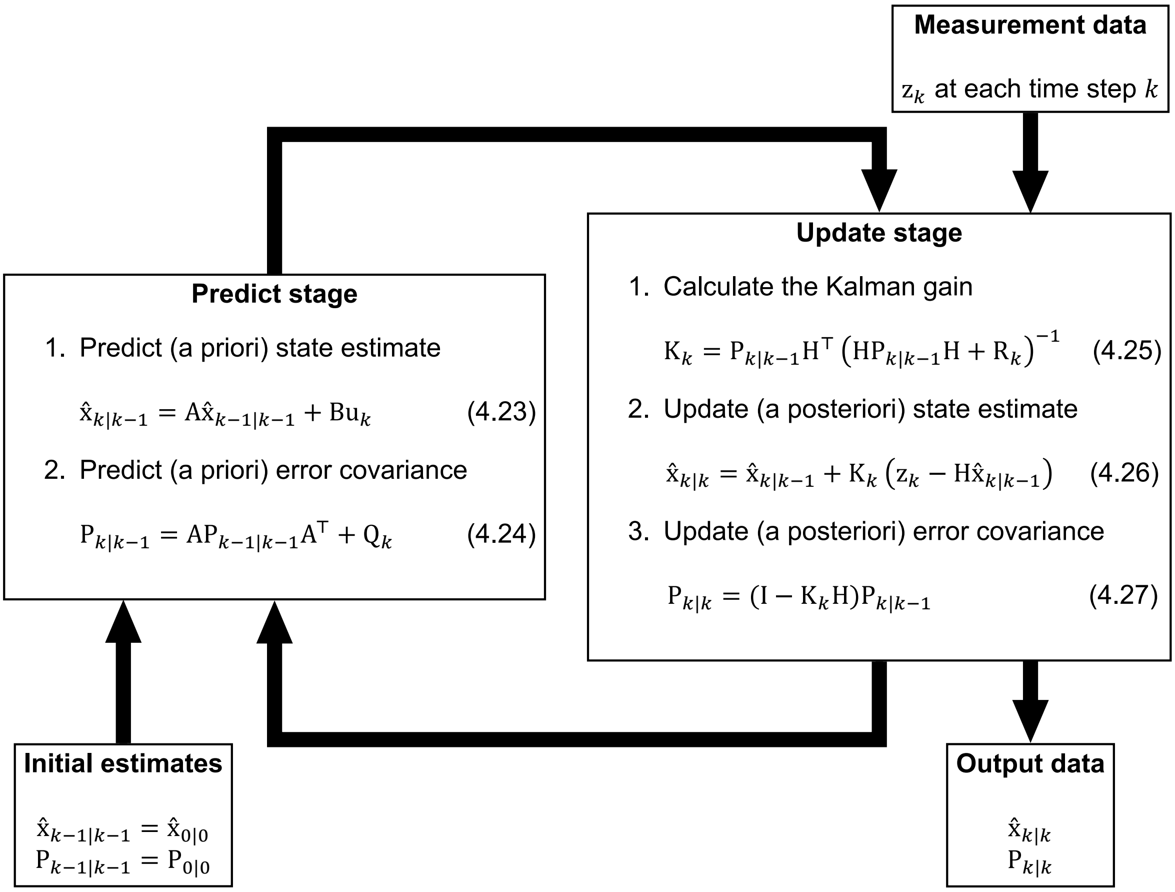
Measurement data
z_k at each time step k
Update stage
1. Calculate the Kalman gain
$\mathrm{K}_k = \mathrm{P}_{k|k-1}\mathrm{H}^\mathrm{T}\left(\mathrm{HP}_{k|k-1}\mathrm{H} + \mathrm{R}_k\right)^{-1}$ (4.25)
2. Update (a posteriori) state estimate
$\hat{\mathrm{x}}_{k|k} = \hat{\mathrm{x}}_{k|k-1} + \mathrm{K}_k\left(\mathrm{z}_k - \mathrm{H}\hat{\mathrm{x}}_{k|k-1}\right)$ (4.26)
3. Update (a posteriori) error covariance
$\mathrm{P}_{k|k} = (\mathrm{I} - \mathrm{K}_k\mathrm{H})\mathrm{P}_{k|k-1}$ (4.27)
Predict stage
1. Predict (a priori) state estimate
$\hat{\mathrm{x}}_{k|k-1} = \mathrm{A}\hat{\mathrm{x}}_{k-1|k-1} + \mathrm{Bu}_k$ (4.23)
2. Predict (a priori) error covariance
$\mathrm{P}_{k|k-1} = \mathrm{AP}_{k-1|k-1}\mathrm{A}^\mathrm{T} + \mathrm{Q}_k$ (4.24)
Initial estimates
$\hat{\mathrm{x}}_{k-1|k-1} = \hat{\mathrm{x}}_{0|0}$
$\mathrm{P}_{k-1|k-1} = \mathrm{P}_{0|0}$
Output data
$\hat{\mathrm{x}}_{k|k}$
$\mathrm{P}_{k|k}$

Figure 4.17: Operation overview of the Kalman filter. The filter requires the initial estimates and measurement data at each time step to update. The filter outputs the updated state estimate and error covariance.

4.6.1. State Vector

To accomodate all the measurement data and filter the data to acquire the position measurement the state vector is

$$\mathrm{x}_k = \begin{bmatrix} x_k \\ \dot{x}_k \\ y_k \\ \dot{y}_k \\ z_k \\ \dot{z}_k \\ \theta_k \end{bmatrix} \tag{4.28}$$

Where x, y, z and θ correspond respectively to surge, sway, heave and roll position at time step k of the vessel at the sensor location and $\dot{x}$, $\dot{y}$ and $\dot{z}$ correspond the velocity at time step k. The measured accelerations, and angular velocity of the IMU are used as control input resulting in the control vector

$$\mathrm{u}_k = \begin{bmatrix} \ddot{x}_k \\ \ddot{y}_k \\ \ddot{z}_k \\ \dot{\theta}_k \end{bmatrix} \tag{4.29}$$

The state model chosen is a Wiener process acceleration model [5]. Combining this with standard state model of the kalman filter 4.17 and 4.23 results in the transition model A and control input model B

$$\underbrace{\begin{matrix} \begin{bmatrix} x_k \\ \dot{x}_k \end{bmatrix} \\ \begin{bmatrix} y_k \\ \dot{y}_k \end{bmatrix} \\ \begin{bmatrix} z_k \\ \dot{z}_k \end{bmatrix} \\ \begin{bmatrix} \theta_k \end{bmatrix} \end{matrix}}_{\mathrm{x}_k} = \begin{matrix} \begin{bmatrix} x_{k-1} + \Delta t \dot{x}_{k-1} + \frac{1}{2}\Delta t^2 \ddot{x}_k \\ \dot{x}_{k-1} + \Delta t \ddot{x}_k \end{bmatrix} \\ \begin{bmatrix} y_{k-1} + \Delta t \dot{y}_{k-1} + \frac{1}{2}\Delta t^2 \ddot{y}_k \\ \dot{y}_{k-1} + \Delta t \ddot{y}_k \end{bmatrix} \\ \begin{bmatrix} z_{k-1} + \Delta t \dot{z}_{k-1} + \frac{1}{2}\Delta t^2 \ddot{z}_k \\ \dot{z}_{k-1} + \Delta t \ddot{z}_k \end{bmatrix} \\ \begin{bmatrix} \theta_{k-1} + \Delta t \dot{\theta}_k \end{bmatrix} \end{matrix} + \mathrm{w}_k = \underbrace{\begin{matrix} \begin{bmatrix} 1 & \Delta t \\ 0 & 1 \end{bmatrix} \\ \begin{bmatrix} 1 & \Delta t \\ 0 & 1 \end{bmatrix} \\ \begin{bmatrix} 1 & \Delta t \\ 0 & 1 \end{bmatrix} \\ \begin{bmatrix} 1 & 0 \end{bmatrix} \end{matrix}}_{\mathrm{A}} \underbrace{\begin{matrix} \begin{bmatrix} x_{k-1} \\ \dot{x}_{k-1} \end{bmatrix} \\ \begin{bmatrix} y_{k-1} \\ \dot{y}_{k-1} \end{bmatrix} \\ \begin{bmatrix} z_{k-1} \\ \dot{z}_{k-1} \end{bmatrix} \\ \begin{bmatrix} \theta_{k-1} \end{bmatrix} \end{matrix}}_{\mathrm{x}_{k-1}} + \underbrace{\begin{matrix} \begin{bmatrix} \frac{\Delta t^2}{2} \\ \Delta t \end{bmatrix} \\ \begin{bmatrix} \frac{\Delta t^2}{2} \\ \Delta t \end{bmatrix} \\ \begin{bmatrix} \frac{\Delta t^2}{2} \\ \Delta t \end{bmatrix} \\ \begin{bmatrix} \Delta t \end{bmatrix} \end{matrix}}_{\mathrm{B}} \underbrace{\begin{matrix} \begin{bmatrix} \ddot{x}_k \end{bmatrix} \\ \begin{bmatrix} \ddot{y}_k \end{bmatrix} \\ \begin{bmatrix} \ddot{z}_k \end{bmatrix} \\ \begin{bmatrix} \dot{\theta}_k \end{bmatrix} \end{matrix}}_{\mathrm{u}_k} + \mathrm{w}_k \tag{4.30}$$

where Δt is the time between the previous and the current step in this case $\Delta t = k - (k-1)$. For the measurement state the observation mapping model can be found in a simular manner:

$$\mathrm{z}_k = \begin{matrix} \begin{bmatrix} x_k \\ 0 \end{bmatrix} \\ \begin{bmatrix} y_k \\ 0 \end{bmatrix} \\ \begin{bmatrix} z_k \\ 0 \end{bmatrix} \\ \begin{bmatrix} \theta_k \end{bmatrix} \end{matrix} = \underbrace{\begin{matrix} \begin{bmatrix} 1 & 0 \end{bmatrix} \\ \begin{bmatrix} 1 & 0 \end{bmatrix} \\ \begin{bmatrix} 1 & 0 \end{bmatrix} \\ \begin{bmatrix} 1 \end{bmatrix} \end{matrix}}_{\mathrm{H}} \underbrace{\begin{matrix} \begin{bmatrix} x_k \\ \dot{x}_k \end{bmatrix} \\ \begin{bmatrix} y_k \\ \dot{y}_k \end{bmatrix} \\ \begin{bmatrix} z_k \\ \dot{z}_k \end{bmatrix} \\ \begin{bmatrix} \theta_k \end{bmatrix} \end{matrix}}_{\mathrm{x}_k} + \mathrm{v}_k \tag{4.31}$$

with the measurement noise and the respective covariance matrices for the translations:

$$\mathrm{w}_k = \gamma \begin{bmatrix} \Delta \frac{t^2}{2} \\ \Delta t \end{bmatrix}, \quad \mathrm{Q}_k = \gamma^2 \mathrm{BB}', \quad \mathrm{v}_\mathrm{k} = \zeta \begin{bmatrix} 1 \\ 0 \end{bmatrix}, \quad \mathrm{Q}_k = \zeta^2 \mathrm{HH}' \tag{4.32}$$

Where γ is the magnitude of the IMU acceleration noise and ζ is the magnitude of the LRF measurements after the ICP process. The covariance matrices for the roll rotation are computed in the same manner. The IMU and LRF measure at a different measurement output rate, therefore The Kalman filter predicts at the frequency of the IMU of 100 Hz. The update stage is only done when there is a new measurement from the LRF at 25 Hz. For the Kalman filter no pseudo code is given because figure 4.17 tells the complete working principle of the algorithm. A link to the Matlab code of the Kalman filter can be found in appendix A.1.

The noise levels for the IMU and LRF are set respectively to $\gamma = 1$ and $\zeta = 0.1$. The result of a simple simulated sine motion, with a amplitude of 0.69 m and frequency of 0.2 Hz, is shown in figure 4.18. The red line indicates the position based on only the Wiener model and IMU acceleration data. Due to the noisy IMU acceleration measurement data that is integrated twice, the position measurement experiences drift. The LRF data does not drift, however the measurement data alone is to noisy to use as output for the LRU. The output position of Kalman filter, showed by the green line, takes about 1.5 s to converge to the input motion showed by the yellow line. The result is a relatively smooth curve following the input motion very well without any unwanted behaviour, for example delay. The figure also shows low pass filtered acceleration data. This low pass filter has a cut off frequency of 10 Hz. In this example the low pass filtered data is not used, the low pass filtered data might come in handy during testing.

4.7. Measurement Loop

The parts of the algorithm explained in previous sections come all together in the main measurement loop. This loop is active until the user disables it. Other handles could be used to stop the measurement loop, for example the gangway position could trigger a stop signal if it is retuning to the stowed position on the deck of the vessel in the main measurement loop.

First the measurement data is read from the IMU and LRF, both sensors are connected via Ethernet. The IMU is connected to a Raspberry Pi that runs a Python script set to always sent the translational

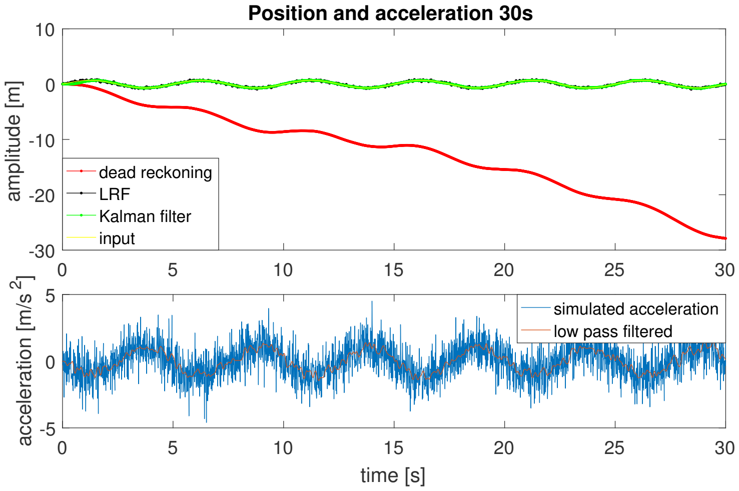

(a) 30 s motion

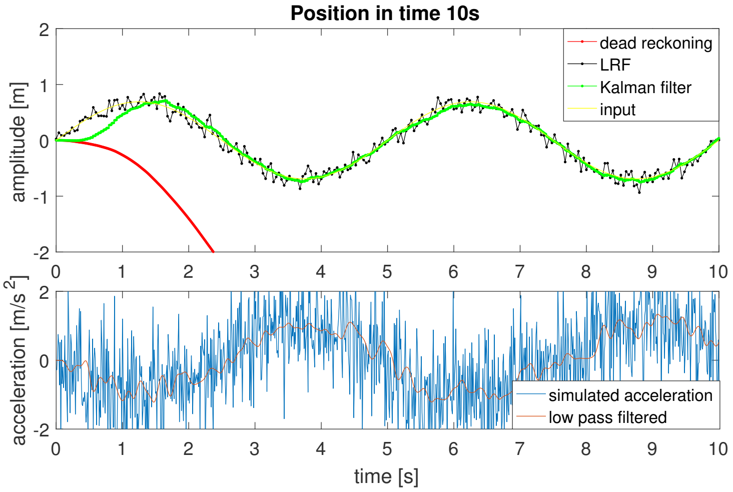

(b) 10 s motion

Figure 4.18: The Kalman filter in action on simulated sine motion with an amplitude of 0.69 m with a frequency of 0.2 Hz. With added Gaussian noiseon the acceleration and LRF position data. The simulated LRF data is updated with a frequency of 25 Hz the Kalman filter and simulated IMU data predict at a frequency of 100 Hz. In (a) the motion is showed for a duration of 30 s, in (b) a zoomed view of the first 10 s is shown.

accelerations, rotational velocity and the orientation by means of Euler angles via an UDP protocol. The LRF settings can be changed in a separate Matlab file that is used to read and translate the LRF measured data. The LRF communicates via a TCP protocol. This read-out script is also used to activate the LRF. The measurement loop runs at the same frequency as the IMU sensor sends data at a rate of 100 Hz. The acceleration data is filtered with a low-pass filter and a prediction is done by the Kalman filter. Once every four loops there is also new measurement data available from the LRF.

If a new measurement of the LRF is available, then the algorithm switches to the required steps to translate this measurement data, find landmarks and match the data for the update step in the Kalman filter. All the user defined settings and boundaries used during simulation and testing are listed in table 4.1. The main measurement loop algorithm is summarized with pseudo code in algorithm 5. A link to the Matlab code can be found in appendix A.1.

Table 4.1: All user defined algorithm settings used during simulation and testing.

name	value	unit	explanation
Measurment loop			
$boundingBox$	$[6.5, 13, -15, 15]$	m	$[x_{min}, x_{max}, y_{min}, y_{max}]$
$inlierSelection$	$allpoints, inliers$	-	select points to be taken as inliers: $allpoints$: all the point in the bounding box. $inliers$: uses the inlier's found by the landmark detection
n_{lines}	3	#	the number of maximum lines to search
n_{arcs}	3	#	the number of maximum arcs to search
$low-pass$	$0/1$	boolean	use low-pass filter on acceleration data (1)
$accNoiseMag$	1	$\mathrm{m\,s^{-2}}$	acceleration noise magnitude for the Kalman filter γ
$lrfNoiseMag$	0.1	m	position noise magnitude for the Kalman filter ζ
RANSAC line			
$iterNum$	30	#	maximum number of iterations
$thDist$	0.02	m	inlier distance
$thInl$	25	#	minimum amount of required inlier's
$maxLength$	2	m	maximum length of line
RANSAC arc			
$iterNum$	200	#	maximum number of iterations
$thDist$	0.005	m	inlier distance
$thInl$	6	#	minimum amount of required inlier's
$minRadius$	0.15	m	minimum radius of arc
$maxRadius$	0.20	m	maximum radius of arc
ICP			
$maxIter$	100	#	maximum number of iterations
$minIter$	1	#	minimum number of iterations
ϵ	$1e^{-5}$	m	maximum residual mean squared euclidean distance error

Algorithm 5 New MRU main loop

```
procedure LRU($boundingBox, inlierSelection, n_{lines}, n_{arcs}, lowPass, accNoiseMag, LrfNoiseMag$)
    while Measuring do
        $t$ = time stamp
        Get $imu$ measurement data at 100 Hz and $lrf$ measurement data at 25 Hz
        if new LRF measurement then
            $newLrfMeasurement = 1$
            if BoundingBox $isnot$ empty then
                Remove scan points outside bounding box
            end if
            if $inlierSelection = endpoints$ OR $inliers$ then
                for $i = 1$ to $n_{lines}$ do
                    function ransac line($pts, iterNum, thDist, thInl, maxLength$)
                    remove found line inliers from $pts$ and store line data $icp_{points}$
                end for
                for $i = 1$ to $n_{arcs}$ do
                    function ransac arc($pts, iterNum, thDist, thInl, minRadius, maxRadius$)
                    remove found arc inliers from $pts$ an store arc data $icp_{points}$
                end for
            elseselect
                store all point cloud points in $icp_{points}$
            end if
            function ICP($pts, pts_{ref}, maxIter, minIter, \epsilon$)
            if abs($Translation_t - Translation_{t-1}) \geq 0.007$) then
                recompute ICP with only lines or arcs
                if abs($Translation_t - Translation_{t-1}) \geq 0.007$) then
                    $Translation_t = Translation_{t-1}$
                    $Rotation_t = Rotation_{t-1}$
                    $newLrfMeasurement = 0$
                end if
            end if
        end if
        if $lowPass = 1$ then
            function lowPass($imu_{acc}, bandPass = 0.5\text{Hz} cutOff = 10\text{Hz}$)
                store low-pass filtered $imu$ acceleration data for Kalman Filter
        end if
        Create Kalman model based on $\Delta t = time_t - time_{t-1}$
        function Kalman Filter($x_k(t-1), P_k(t-1), newLrfMeasurement$)
        Output current position, clean data
    end while
end procedure
```

5

Simulation & Testing

To determine how well the proposed LRU performs a software simulation model is created. This model is used to test the LRU on different user defined target platform structures and input motions. The model and the algorithm are verified by means of testing. The test setup created is also discussed in this chapter. Both the simulation and test results will be discussed in the next chapter.

5.1. Simulation Model

The simulation model is created to test different vessel motions and target structures. The simulation model will give a indication of the performance of the LRU. The simulation model is also used to test the boundaries for the different parts of the algorithm. A simulation model enables the opportunity to do extensive testing of the system on all kinds of different operation situations without actually sailing to all these locations offshore. The model is created based on the following requirements:

- The simulation model can handle different input motions: user generated or from log data gathered offshore.
- The user is able to create 3D shapes that are used as the offshore target.
- The user is able to set the different measurement settings of the LRF.
- The simulation model generates the measurement data of the LRF and IMU as close as possible to the actual measurement data, including noise.

5.1.1. LRF Simulation

The target platform is created by the user. The created example target platform consist of six pillars. three horizontal and three vertical pillars. The vertical an horizontal scanner are both set to a resolution of $0.1667°$and a search is done where the laser scan lines intersect with the target platform. These intersection points are returned as scan points of the LRF. The noise levels specified in the specifications of the LRF are used to add noise to the found points. A step in time is made of 0.25 s and the corresponding position and orientation in time is changed of the LRF. A new scan is made and the intersection points are returned. This process is repeated until the user defined motion is finished. The scanning of the vertical and horizontal scanner to the target is illustrated in figure 5.1. A result of the scan point cloud on one of the pillars is illustrated in figure 5.2.

Generating LRF data of a vessel motion is a computationally expensive process. A motion of 100 s takes a couple of hours to generate the point cloud data. This is due to the expensive find function used in Matlab. If the simulation model is used more extensive it would be wise to use a different approach of finding the intersection points. One could use the information of the model and the distance from the LRF to the target to generate measurement points. This disadvantage of this approach is that the model of the target is no longer easily adjustable. For this research the time the simulation takes is not a problem. Only if more extensive testing by means of simulation is necessary it is advised to make the LRF simulation model more efficient.

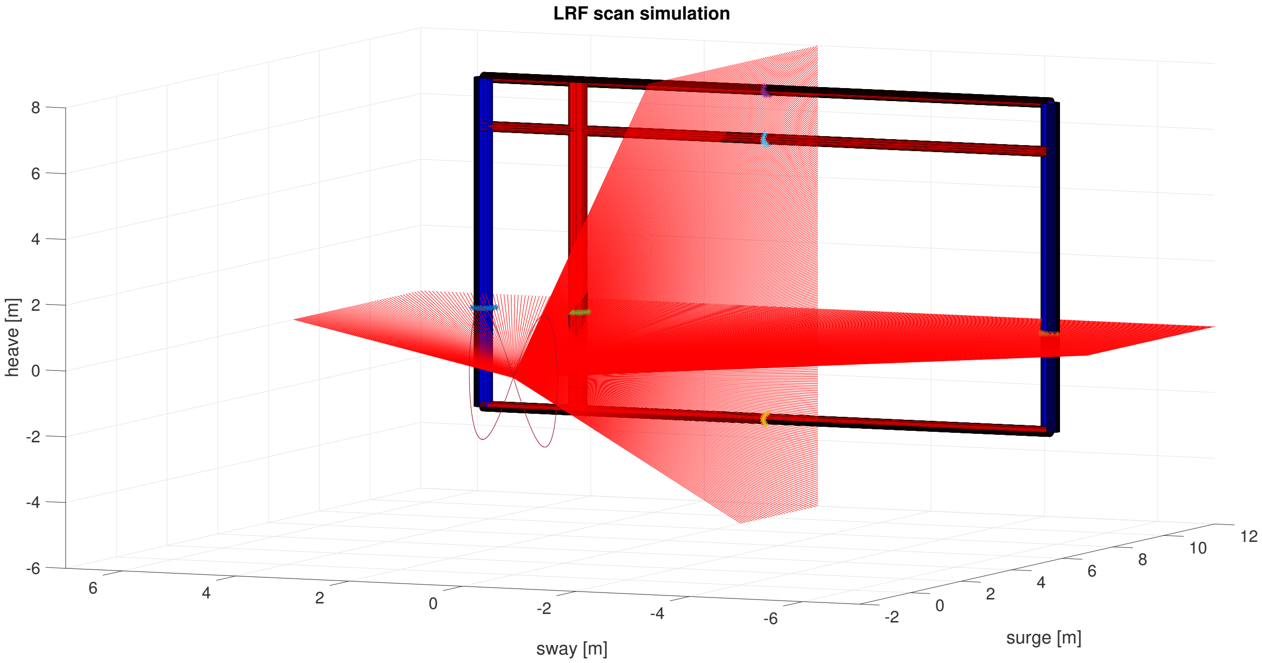

Figure 5.1: A scan of the simulation model. The target consist of three horizontal and three vertical cylinders at a distance of 12 m from the LRF scanners. The input motion that the LRF is following during the simulation is plotted around the origin. The intersection points of the scan are highlighted in the figure with *. The scan lines continue outside the box of the plot, this is not shown in the figure.

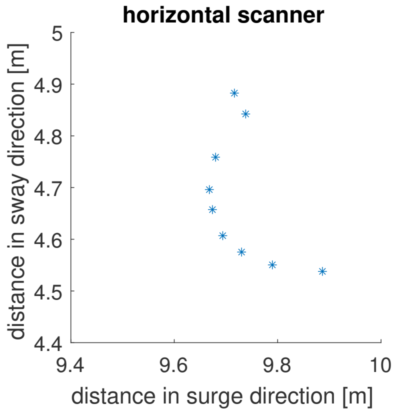

Figure 5.2: The point cloud of single pillar created by the LRF simulation.

5.1.2. IMU Simulation

The IMU sensor output simulation is straight forward. The motion data is differentiated to acquire the angular velocity and the translational accelerations. Noise is added to these motions. The noise levels are determined with a simple test measurement where the BNO055 sensor is in a still position for 60 s. The noise levels are determined based on this measurement and added to the generated motion data.

The most noisy data from the BNO055 is the acceleration measurement as illustrated in figure 5.3. The sensor is not positioned exactly level in the still position, the mean of the signals is subtracted and the standard deviation is computed.

The resolution of the acceleration measurement is bounded by 14bit on a range of $\pm 8\text{g}$. This is clearly visible in the measurement data. The noise factors used can be found in table 5.1. The simulated acceleration in sway direction is compared to the measured acceleration in figure 5.4.

The fused data of the Euler angles by the BNO055 shows no noise while in a still position for 60 s. This is seen in figure 5.5. All the used noise levels during the simulation model for the IMU are shown in table 5.1.

When the IMU measurement data is used for position measuring, drift is a major problem. Due to the noise levels on the acceleration data the position based on dead reckoning drifts in time. While the

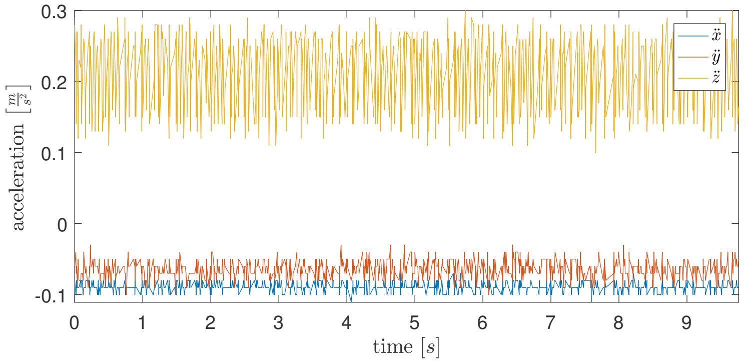

Figure 5.3: The accelerations measured by the BNO055 IMU while laying still for 60 s. Only the first 10 s are shown.

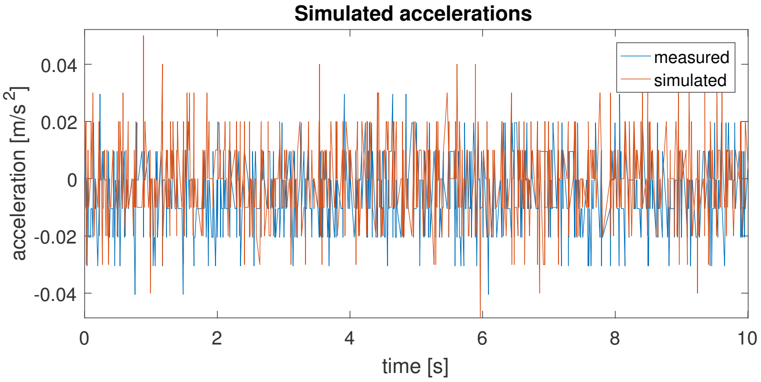

Figure 5.4: The simulated sway accelerations compared to the measured sway accelerations by the BNO055 IMU while laying still for 10 s.

sensor is in a still position. The position after 60 s is almost 1 m off in the sway direction as shown in figure 5.6. The dead reckoning is done using only the accelerometer data of the measured directions, the acceleration data is normalized around zero for this example.

5.1.3. Combining the Simulations

The simulation data is combined and a time vector is added. The IMU data is sampled at 100 Hz and once every four IMU simulation data points the simulated LRF data is added. The simulation model is used with two different motions. The motion and the results are shown in chapter 6.

5.2. Test Set-up

To verify the model results and determine the performance of the LRU two test setup's are proposed.

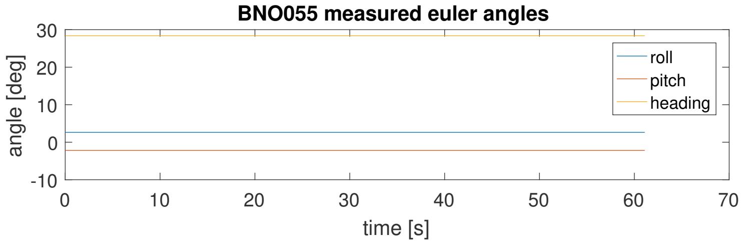

Figure 5.5: The measured Euler angles by the BNO055 IMU while laying still for 60 s.

Table 5.1: IMU noise levels during simulation

noise	value	unit
acc_{surge}	0.0065	$\mathrm{m\,s^{-2}}$
acc_{sway}	0.0131	$\mathrm{m\,s^{-2}}$
acc_{heave}	0.0476	$\mathrm{m\,s^{-2}}$
vel_{roll}	0.0732	$\mathrm{m\,s^{-1}}$
eul_{roll}	0	°
eul_{pitch}	0	°
eul_{yaw}	0	°

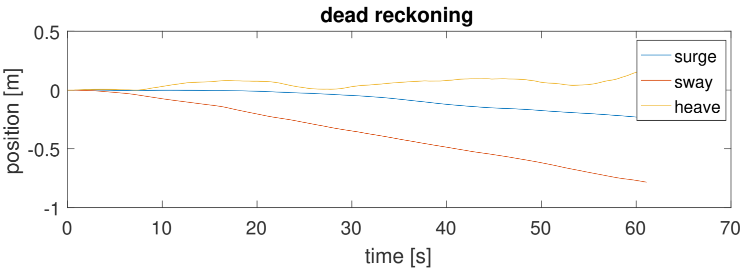

Figure 5.6: Dead reckoning using only the noise levels of the three directions acceleration measurement data of the BNO055 while laying still.

5.2.1. Rotation Swing

The Euler angles measured by the BNO055 are generated by on chip sensor fusion. To get an impression of the measurement data a simple test setup is created. The BNO055 is aligned and glued to a steady baseplate. A box containing the Raspberry Pi to read the sensor data is placed over the sensor on the baseplate. The baseplate contains four holes in the corners. These holes are used to suspended the sensor in the air, via cord connected to the sealing. The sensor is powered via the Raspberry Pi, which is powered by a portable power-bank. This creates a swing, swinging with a frequency for small angles of:

$$f = 2\pi\sqrt{\frac{L}{g}}, \quad g = 9.81\,\mathrm{m\,s^{-2}} \tag{5.1}$$

With g the gravitational acceleration and L the length of the cord. A Python script reads the sensor data at 100 Hz and logs the measurement data in a text file. A protractor is drawn on a whiteboard behind the swing and during testing a video of the test setup is recorded. The swing is actuated by releasing it at an certain angle. This is shown in figure 5.7.

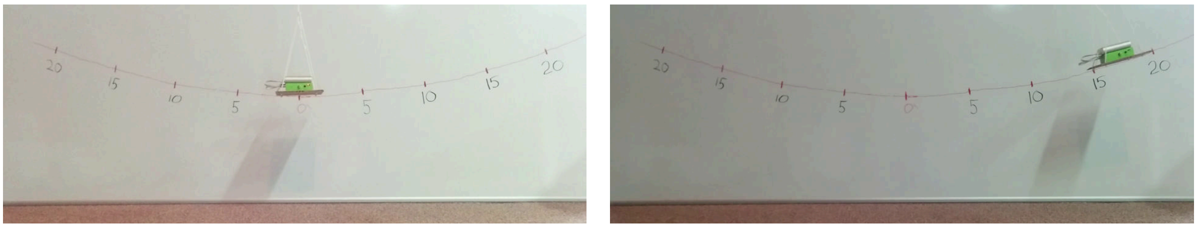

(a) In rest (b) Swinging

Figure 5.7: A swing for rotational testing of the IMU Euler angle results. In (a) the swing is in rest, in (b) the IMU is swinging.

This test setup does not allow for good Euler angle accuracy test, however it does return some interesting results that will be discussed in section 6.2. The IMU uses the gravitational field of the earth as a reference to measure its orientation in roll and pitch rotations. The heading or yaw angle has no reference since the magnetometer is switched of during testing. For this research the pitch and yaw angles are not investigated, but the yaw angle could easily be updated with LRF yaw angle that has the target platform as reference. A link to the movies made during the test measurements can be found in appendix A.3.1.

5.2.2. Translation Sled

The focus for testing is to test the performance of the LRU. The translations require both sensors for an accurate and smooth result. At Ampelmann a start was made, by A.G. Verweij, to create such a translation test bench, showed in figure 5.8. The test setup is able to create a translational motion in a single DoF. The setup is upgraded and prepared in corporation with A.G. Verweij to work with the following test setup requirements:

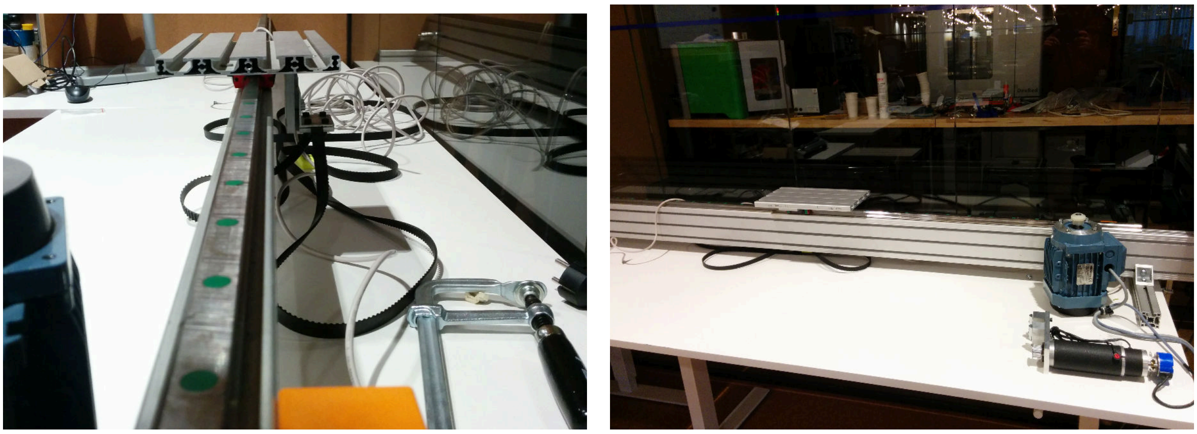

(a) In rest

(b) Swinging

Figure 5.8: A swing for rotational testing of the IMU Euler angle results. In (a) the swing is in rest, in (b) the IMU is swinging.

- The actual position of the sled is known and sent in real time to the user.
- The sled can actuate a user defined translational motion up till a peak-to-peak amplitude of 1.4 m.
- The sled can achieve at least motion with a frequency of 0.3 Hz and a peak-to-peak amplitude of 1.4 m.
- The user defined desired motion can be sent to the translational test bench in real time.
- the test setup is controlled via an easy to use interface.
- An emergency stop button that will stop the sled whatever state it is in.

This list of requirements resulted in a test setup that consists of a straight rail of 2.3 m. On top of this rail is a platform connected via a linear bearing to the rail, called the sled. The sled can move in a straight line across the rail. Connected to the sled is a toothed belt which extends around a bearing at one end and a toothed wheel connected via a gear to a frequency drive actuator at the other end. Close to the toothed wheel is a inductive sensor, used to determine the home position of the sled on start-up. A rotational encoder is used to determine the position of the sled and is connected to the shaft of the toothed wheel. An overview of the test setup is illustrated in figure 5.9.

The actuator, encoder and inductive sensor are connected to a PLC. The PLC is used to control the test bench and act as the communication between the test setup and the user. A state machine is coded on the PLC that controls the states of the measurement setup. The state machine also defines how the test setup change between states. The different states are:

- **Not Homed:** The sled is still and there is no actuation. The PLC does not know where or in what position the sled currently is on the rail. When the test setup is powered on, it will always be in the not Homed state. When the emergency button is used the test setup returns to the Not Homed state as well.

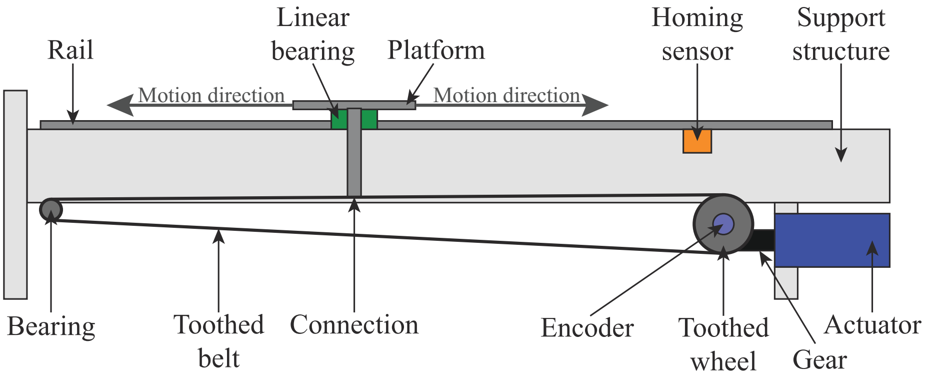

Figure 5.9: Illustration of the translational motion test setup. All the required parts of the setup are pointed out in the figure.

- **Home:** In the Home state the sled is positioned on top of the homing sensor. The current encoder position is taken and translated to a position of the sled. This position is set to −0.7 m in the Home state. The home position is reached by initiating the homing sequence via the sled control panel. When the homing sequence is activated the actuator is given a constant velocity input in the direction of the homing sensor and stops when reaching the homing sensor.
- **Neutral:** In the Neutral state the sled is moved from the Home state to the centre of the rail, corresponding to a position at 0 m. Because the position of the sled is know use is made of a S-curve to get to the neutral position. The S-curve creates a smooth motion where the maximum velocity is reached halfway the start and end position. This allows for a vertical positioning of the test setup, also when heavy sensors are used because the motion is controlled via the feedback loop. The neutral state is reached via a user input on the sled control panel.
- **Engaged:** During the engaged state the sled is actuated to follow the reference motion input. The Neutral to Engaged state is initiated via the control panel. To prevent sudden rapid motions due to a large position difference between the motion reference and the current sled position an S-curve is used during this state transition. The S-curve gradually introduces the reference motion over a time of 10 s.

The measurement setup is controlled by the user via the sled control showed in figure 5.10a. The control panel sends commands to the PLC of the measurement setup when the user pushes the buttons. It is not possible to go from a state to any other state without following the proper route via the necessary states. The required sequence is illustrated in figure 5.10b. The normal sequence is: Home → Neutral → Engaged, do the measurement and go back to Home/Safe via the same route you came. There is one exception the physical emergency stop or E-STOP button and the reset button on the control panel will stop the sled no matter which state its in. The E-STOP or reset action requires the sled to be homed again before use, this is to prevents any damage because the E-STOP is probably used for a reason.

The position of the sled is controlled with a proportional feedback controller on the PLC. The motion reference data contains the required position and velocity of the sled. This reference motion $r(t)$ is sent over Ethernet via the User Datagram Protocol (UDP) to the PLC. The current location of the sled, measured by the encoder on the actuator axis, is subtracted from the reference. The difference between the reference and the current position is the error $e(t)$. The error is used by the proportional feedback controller. The controller outputs a current $u(t)$ which is used by the frequency drive to operate the actuator, which is connected to a gearbox with a ratio of $9:1$ to the sled. The current position of the sled is the read from the rotational encoder $y(t)$. The control loop is illustrated in figure 5.11. The velocity reference signal $\dot{r}(t)$ is only used as feed-forward control.

The LRF and IMU are mounted on the platform of the sled to complete the measurement test setup. A simple target platform is constructed consisting of two pillars and two boxes in the horizontal scanning plane. In the vertical scanning plane the target platform consists of two platforms and three boxes. The complete test setup and the target platform are shown in figure 5.12.

Different motions are simulated during testing: the test setup is placed parallel to the target platform to simulate a sway motion of the vessel. The test setup is rotated $45°$to simulate a combined motion in

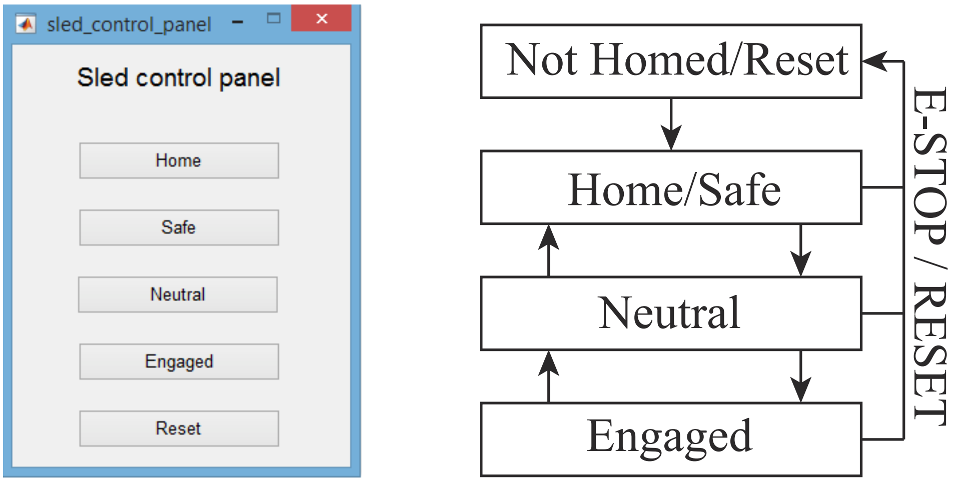

(a) Sled control panel (b) Sled state machine

Figure 5.10: The user input sled control panel of the test setup and the corresponding state machine. (a) The sled control panel is used to sent commands to the measurement setup to switch between the states. (b) The state machines shows the different state of the test setup and the possible ways to get from one state to another.

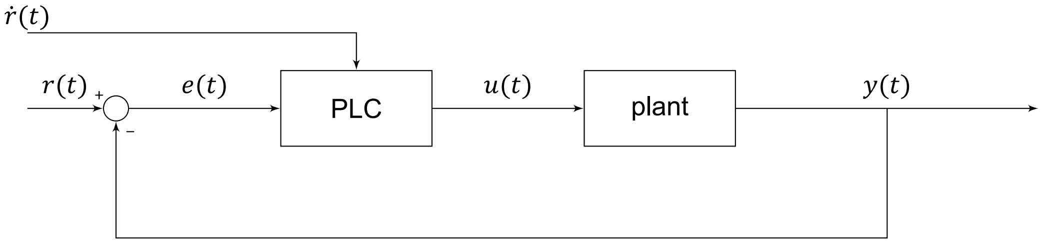

Figure 5.11: The control loop of the translational test setup. The input motion or reference is supplied by a position $r(t)$ and velocity $\dot{r}(t)$. The velocity is used in as feed-forward control for the plant. The reference position $r(t)$ is used in a proportional gain feed-back loop. The plant consist of a current controlled frequency drive connected to a electric AC motor. The motor is connected to a gearbox slowing the rotations with a factor 9. Connected to the gearbox is the toothed wheel driving the belt connected to the sled. The encoder used in the feed-back loop is connected to the axle of the toothed wheel.

the surge and sway direction of the vessel. Due to a limited time no safety limits and smooth stopping of the sled could be integrated in the test setup. To prevent damage and avoid unsafe situations the setup is only used in its level position. Meaning no heave motion could be simulated during testing. A heave motion would imply the LRF to make a scan in the vertical plane while moving. This creates no problem to determine the performance of the system since the measuring process is identical to the horizontal scan plane. The tested motions are mentioned in the results chapter 6. The parts used to create the test setup are listed in table 5.2. Links to movies of the test setup while measuring can be found in appendix A.3.2.

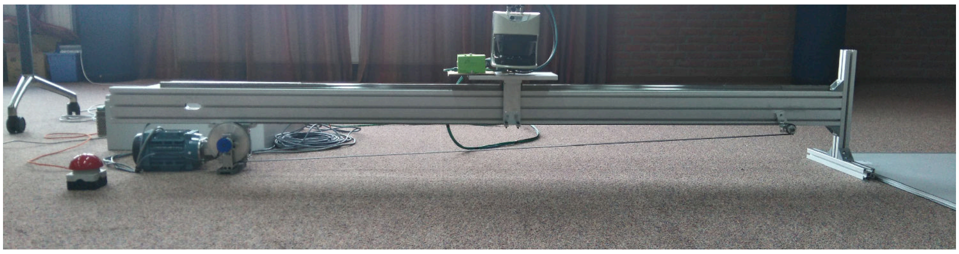

(a) Test setup

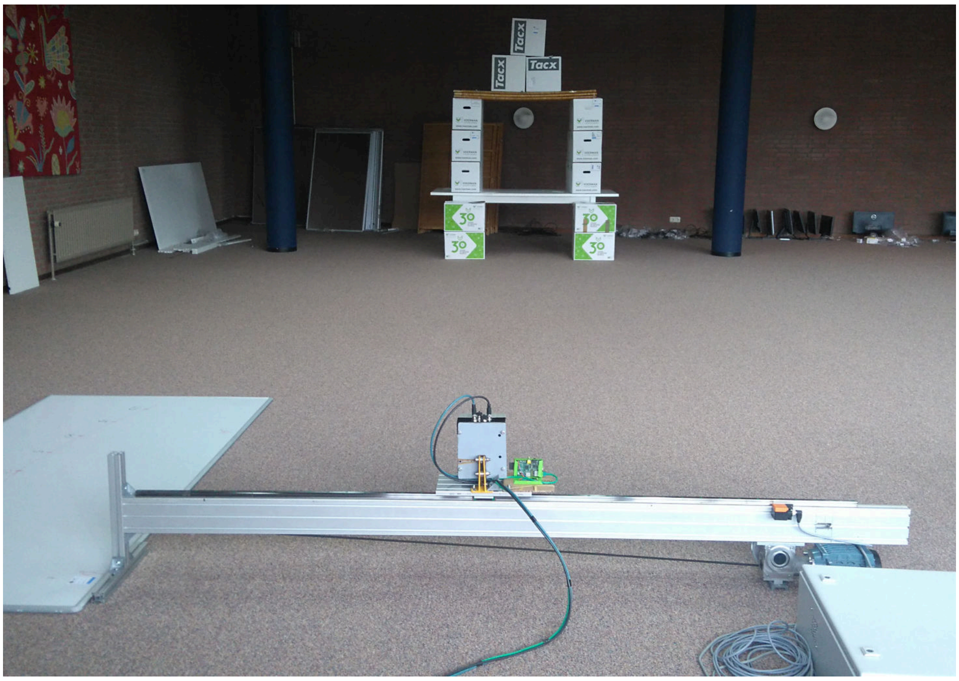

(b) Test setup with target

Figure 5.12: The complete measurement test setup (a) with the sensors on top of the sled platform. (b) the test setup with the target platform at a distance of ≈8.5 m.

Table 5.2: Parts used to create translational test setup.

Manufacturer	Series	Function	serial number
Invertek Drives	Optidrive	variable frequency AC Drive	E2 IP20
ABB Motors	Low voltage AC motors	Actuator	M2VA71A-4
ifm electronic	IM	Inductive sensor	IM5097
Siemens	Simatic	PLC	S7-300 SM317
	Simatic	Analogue output	SM332
	Simatic	Analogue input	SM331
	Simatic	Digital output	SM322
	Simatic	Digital input	SM321
	Simatic	Counter module	SM350
	Simatic	Simatic NET	SM343
Hiwin	Linear guide-ways	Linear guide-ways	HG20
item	MB aluminium profile	aluminium profile Support structure	

6

Results

The measurement results of the two test setups are shown and discussed in this chapter. The test results are compared to the results of the simulation model and the final performance of the LRU is shown and discussed.

6.1. Simulation Model

The results of the simulation model are shown and discussed in this section. The simulation model results are computed using two different input motions.

6.1.1. Simulated Motions

Table 6.1: Components of the simulated sinusoidal input motion for the LRU simulation model.

Direction	**Peak amplitude** [m/°]	**Frequency** [Hz]
Surge	0.5	0.1
Sway	1	0.1
Heave	2	0.2
Roll	10	0.1

Two vessel motions are simulated, the model is designed to apply three translations: surge, sway, heave and a rotation: roll, simultaneously. A simple motion consisting of sinusoidal motions with a different amplitude and frequency per direction. the second motion, the vessel motion created with the AWESOME software for the Damen FCS of section 2.2, is used as input motions in the simulation model. The simple sinusoidal motion is created with the amplitudes and frequency's of table 6.1. The motion describes a rotated figure eight already shown in figure 5.1. Due to the similarity in results of both motions the result of the more interesting vessel motion is showed and discussed in detail. The simulation model results will be concluded with results that combine both measured motions.

6.1.2. Vessel Motion

To see enough detail of the result the motion is only partially shown, from $t = 35$s till $t = 50$s. The result of the ICP output are shown to see how well the LRF algorithm performs in figure 6.1. The output signal of the LRU with Kalman filtering is shown in figure 6.2. The ICP output shows some noise and follows the input motion accurate. The filtered output motion of the LRU is a smooth representation of the input motion.

To compare the results in the remainder of this chapter the difference between the input and output motion is compared. This difference is the error of the LRU. The error is calculated using the absolute peak-to-peak distance between the input and output position at the same moment in time. A clear error peak dominates the first few seconds of the the output motion of the LRU, this is caused by the

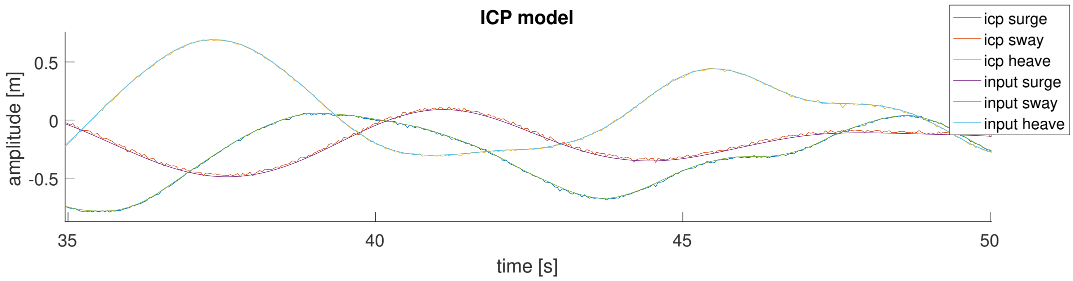

Figure 6.1: The result after matching of the simulation model of the Damen FCS vessel motion from $t = 35$s till $t = 50$s.

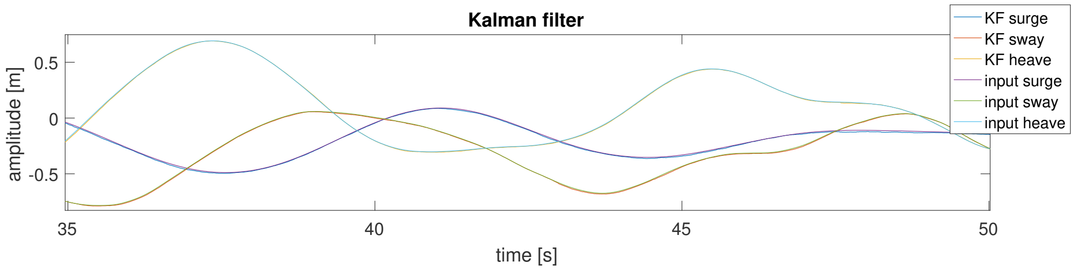

Figure 6.2: The result of the LRU simulation model of the Damen FCS vessel motion from $t = 35$s till $t = 50$s.

Kalman filter. During the first couple of seconds the Kalman gain K_k and the error covariance P_k need to converge in the direction of the measurement update. In the results this convergence area is left out.

6.1.3. Simulation Errors

The results of all simulated and measured motions are summarized in a box-plot. In a box-plot the first quartile splits of the lowest 25% from the highest 75%. The mean cuts the dataset in half and the third quartile splits the highest 25% from the lowest 75%. The explanation of the box-plot can be seen in figure 6.3.

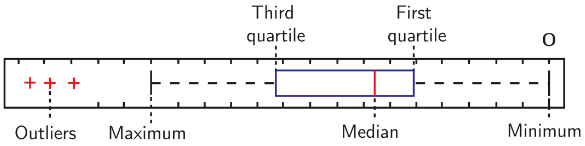

Figure 6.3: meaning of the box-plot parts [43].

All the translational errors of both simulated motions are summarized in figure 6.4. The error for both motions stays below the desired 5 cm.

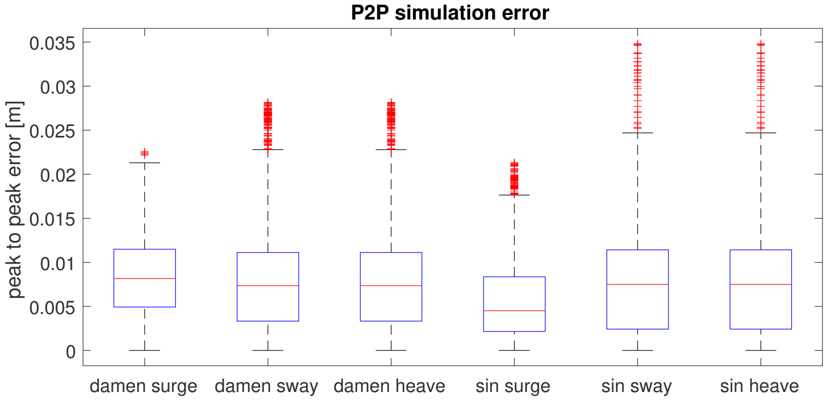

Figure 6.4: The absolute peak-to-peak translation errors of the simulation model of the Damen FCS vessel motions and a sine motion.

6.2. Rotation Swing

The length of the cord is chosen $L = 2.4$ m calculating the frequency of the swing results in $f = 0.321$ Hz. The swing is released at a positive angle of $\approx 15°$. The Euler angles measured and computed by the BNO055 are show in figure 6.5.

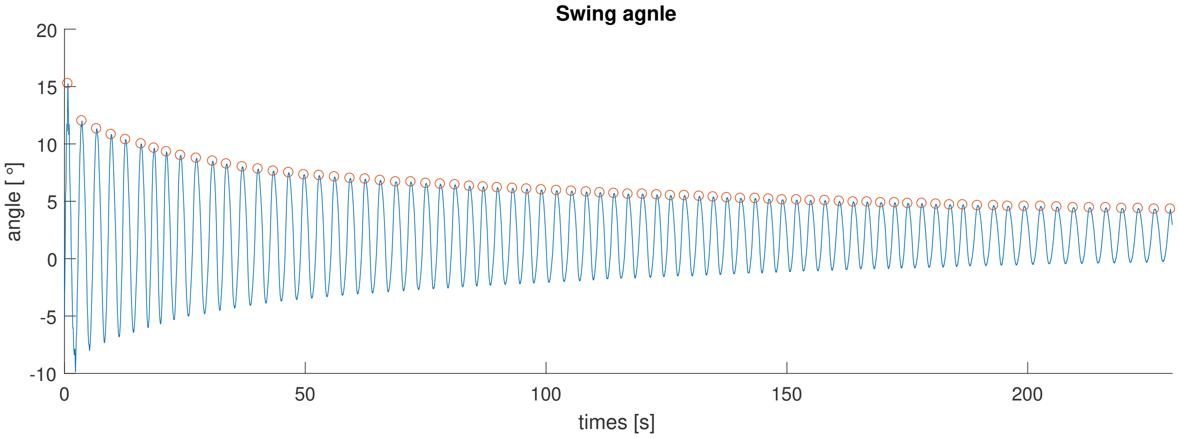

Figure 6.5: The roll angle measured with the BNO055 while swinging on the test setup. The amplitude is as expected decreasing over time. The frequency of the motion is f =0.321 Hz and complies with the expected frequency according to the design of the swing.

The result is in line with the expected trend of a decreasing sinusoidal motion. A PSD of the motion results in a frequency of $f = 0.322$Hz, taken the swing test setup in mind, is as expected. A closer look of the measured angular motion shows a different motion profile than the expected sinusoidal motion shape, visible in figure 6.6. The test setup is suspected to be the cause of this difference in motion profile, perhaps the swing is not aligned correctly resulting in a difference in length of the two cords of the swing. Multiple test where conducted trying different orientations of the swing platform and shifting the centre of gravity and the initial angle of the swing platform. This did not change the motion profile. Results of these tests can be found in appendix A.3.1.

To further investigate the difference in the motion profile, the angular velocity measured by the gyroscope on the BNO055 IMU are plotted in figure 6.6. The angular velocity during the motion does show the correct sinusoidal motion profile. The on chip sensor fusion also outputs the accelerations without the earth gravitational field, called the linear acceleration. The linear acceleration shows the same motion profile as the Euler angles. A conclusion and recommendation on this issue are drawn when then the translational test results are discussed.

The test setup used for rotational testing can only give a estimate of the rotational measurement performance. The strange motion profile found during the rotational tests is not used in the simulation

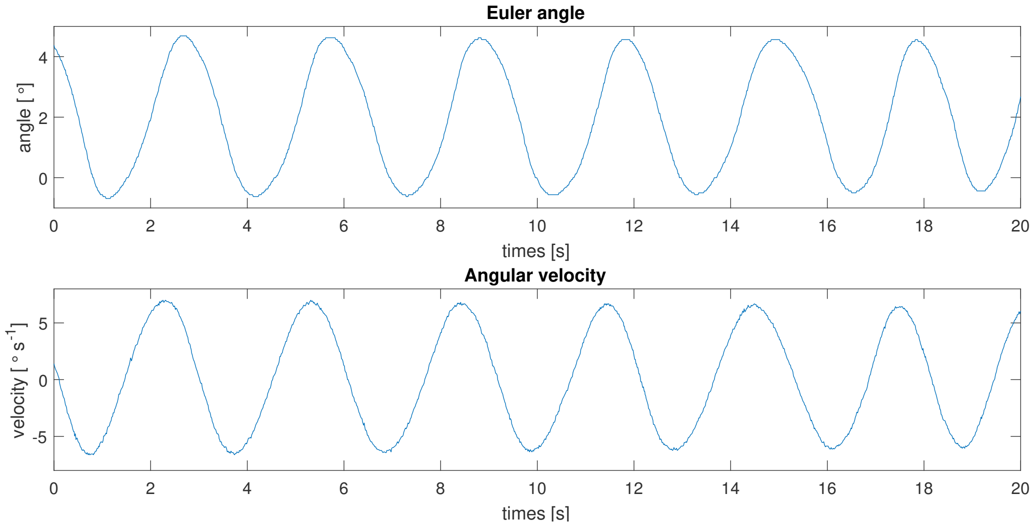

Figure 6.6: A closer look, from $t = 200$s till $t = 220$s of the roll angle from figure 6.5, reveals a unexpected motion profile, while the angular velocity shows the expected motion profile.

model. To verify the rotational outcome of the model and to test if the BNO055 can reach the requirement accuracy of $0.1°$, in combination with the LRF measurement data and the Kalman filter. A test setup is required that can hold both sensors while rotating, combined with accurate rotational position information of the test setup.

6.3. Translation Sled

The translation test setup explained in section 5.2.2 is used to acquire the measurement data for the following results. During testing the linear bearing introduces extra vibrations that are measured by the IMU, especially the acceleration measurements are influenced. The acceleration data of the IMU is therefore filtered using a low-pass filter with a cut-off frequency of 10 Hz.

6.3.1. Motions

The test setup allows for translational motion in one DoF only. By changing the orientation of the test setup with respect to the target a single vessel motion direction can be applied to the LRU or a combined motion. For example: the sway motion of the vessel is achieved by aligning the rail of the test setup parallel to the target platform. The surge motion is achieved by a perpendicular alignment of the test setup rail to the target platform. A combination of these two vessel motion directions is achieved by aligning the rail of the test setup with a defined angle to the target platform. During testing this angle is used to create a combined motion in surge and sway direction with a angle of $45°$, this results in both motions with a reduced amplitude A_{45} of both motions of:

$$A_{45} = \frac{1}{2}\sqrt{2}A_{sled} \tag{6.1}$$

where A_{sled} is the amplitude of the motion of the test setup sled. The motions used during testing are named and numbered, their amplitude, frequency per component are listed in table 6.2. The amplitude values are based on the motion of the sled of the test setup, if the direction is surge and sway one can calculate the amplitude using the above formula. The different components are summed to create the final motion.

These motions are chosen to compare influence of larger versus smaller motions, the influence of frequency of the motion and motion 1 represents a more real-life vessel motion.

6.3.2. Measurement Error

The absolute peak-to-peak error that compares the result of the measurement to the encoder position of the test setup is shown in figure 6.7.

Table 6.2: Names of the motions and their components used during the translational tests. the complete motion used as the reference motion of the sled is the summation of all the components listed per motion.

Name	**direction(s)**	**Comp. 1**	**A** [m/°]	**f** [Hz]	**Comp. 2**	**A** [m/°]	**f** [Hz]	**Comp. 3**	**A** [m/°]	**f** [Hz]
ss 1	surge, sway	sine	0.2	0.15	sine	0.1	0.25	cosine	0.3	0.09
s 1	sway	sine	0.2	0.15	sine	0.1	0.25	cosine	0.3	0.09
ss 2	surge, sway	sine	0.5	0.1						
s 2	sway	sine	0.5	0.1						
ss 3	surge, sway	sine	0.5	0.3						
s 3	sway	sine	0.5	0.3						
ss 4	surge, sway	sine	0.69	0.2						
s 4	sway	sine	0.69	0.2						

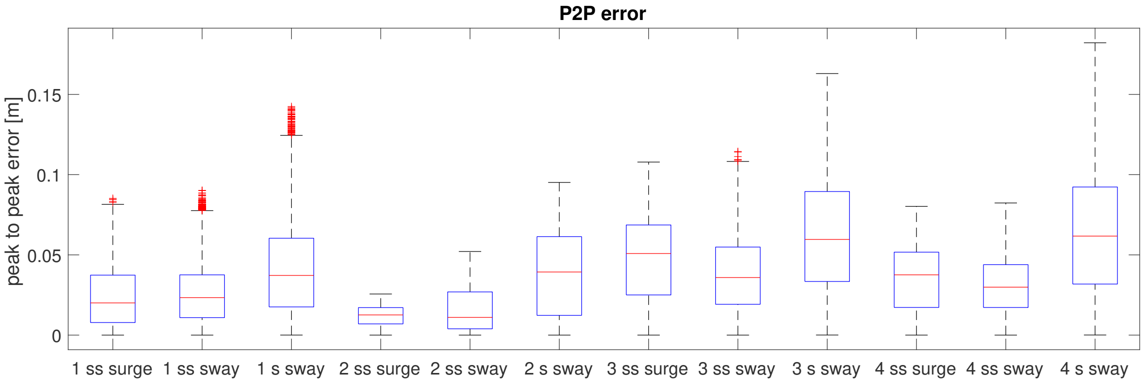

Figure 6.7: The absolute peak-to-peak (P2P) error of the test measurement motions compared in a box-plot. The different motions from table 6.2 illustrate the performance of the LRU.

Motion 2 has the lowest frequency and the smallest amplitude. This results in the lowest error. The larger the amplitude of the motion the greater the error becomes, the same goes for the frequency of the motion. Almost all measurements results in an error higher than the 5 cm claimed by the current MRU used by Ampelmann. the found errors differ from the results found during simulation. To further investigate the origin of the error, motion 1 and 4, both with the largest error are selected for further investigation. Part of the results after the measurement data passed the ICP algorithm are shown in figure 6.8 and the final output of the LRU is shown in figure 6.9.

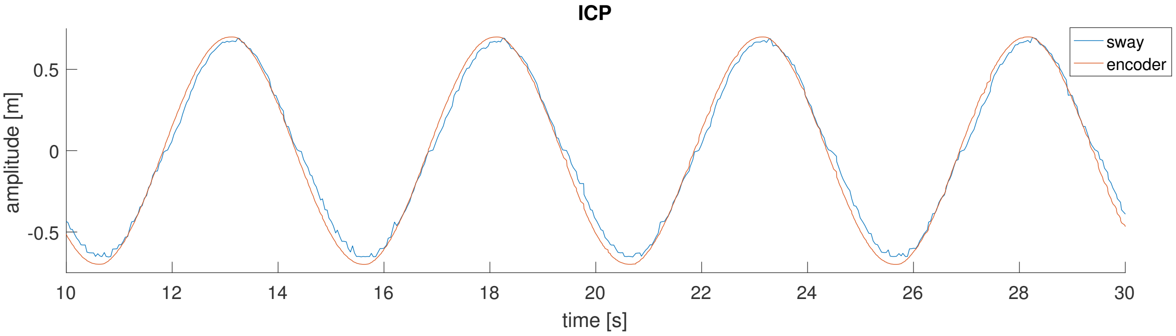

Figure 6.8: The output after the ICP matching algorithm of motion 4 in sway direction. A delay due to the communication buffer or flexibility of the toothed belt of the test setup is clearly visible.

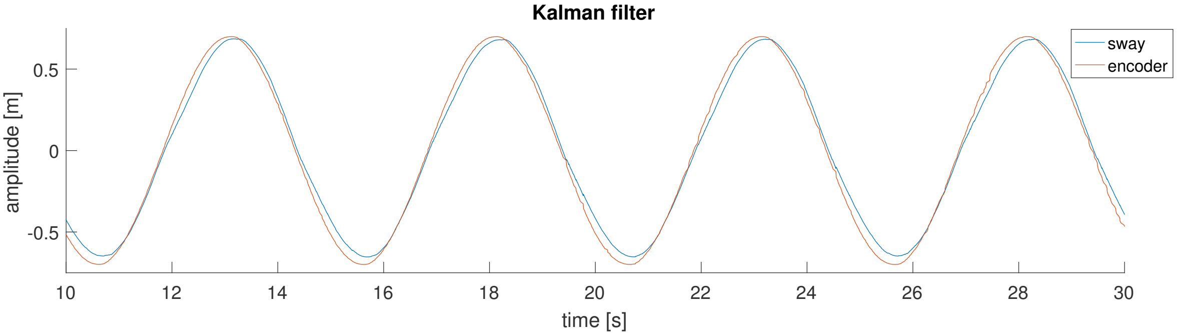

Figure 6.9: The output of the LRU of motion 4 in sway direction. A delay due to communication buffer or flexibility of the toothed belt of the test setup is clearly visible.

A delay is visible between the motion measured by the LRU and the encoder position. The largest peak-to-peak error is a result of the regions where the velocity of the sled is high. This delay can be a result of the communication between the different sensors, because all sensor data is sent via UDP or TCP over Ethernet to a single laptop. The IMU, LRF and test setup encoder data come from different machines and are received by the laptop. If a packet is delayed the laptop waits for the packet and the other measurement packets get buffered until the buffer is full or the packages in the buffer are read. Another cause could be the design of the test setup. The sled of the test setup is driven by a toothed belt, although the belt is pre-tensioned rapid acceleration changes could stretch the belt. The encoder is attached directly to the toothed drive wheel while the sled is connected to a less stiff belt. The position of the sled is determined with the encoder data. To test if the flexibility of the belt causes an additional error on the measurement results the LRF is used to compare the sled position measured by the LRF with the encoder position. To achieve the position measurement of the sled with the LRF a plate is placed at the end of the rail of the test setup, perpendicular to the rail. The scan angle of the LRF is increased, now it measures the target platform and the plate at the end of the rail, at the same time. The mean of all the measurement points on the plate are used to determine the position of the sled. The added plate and the increased scan angle used during these tests are shown in figure 6.10. The results are discussed in the final results at the end of this section.

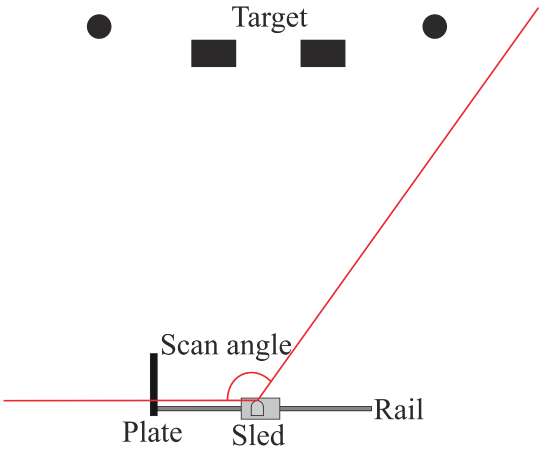

Figure 6.10: test setup approach to use the LRF as a position sensor while still scanning the target. A plate is added perpendicular to the rail and the scan angle of the LRF is increased to scan the plate and the target at the same time.

6.3.3. Obstruction

The RANSAC landmark detection algorithm is used to avoid any of the undesired scan points of the measurement point cloud. This should add to the robustness of the LRU because the landmark detection can also filter unwanted moving people on the target platform. motion 1 and 4 are also measured while a person is walking around the platform. The person is detected by the LRF as shown in figure

6.11b the same motion is scanned without a person obstruction the platform shown in figure 6.11a. In figure 6.11b the person walking around the platform is clearly visible. the RANSAC landmark detection only marks the person 5 times of the 2500 scans made during the measurement. These five points where the person was detected as an arc by the RANSAC algorithm where always close to one of the pillars of the test platform.

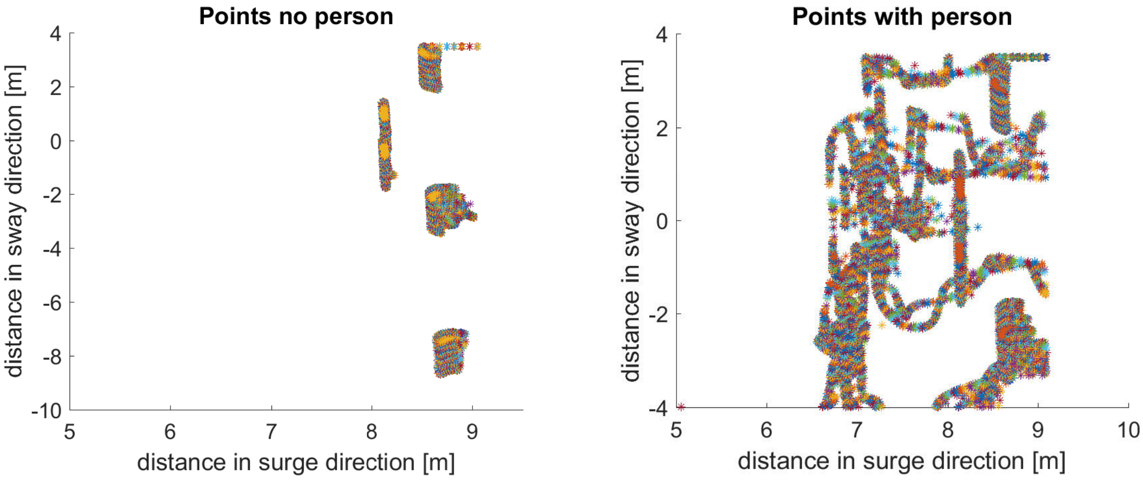

(a) No obstruction

(b) Obstruction

Figure 6.11: A plot of the point cloud of all measured scan points of motion 4 in sway direction with and without obstruction. In (a) there is no person walking around the target platform during measuring while in (b) a person is walking around while measuring.

The results of both measurements, with and without a person of the LRU absolute peak-to-peak error, are shown in figure 6.12. Due to the RANSAC landmark detection combined with the Kalman filter prediction taking over during the moments of detection of the person there is almost no difference in error for both motions with or without a person obstructing the target platform.

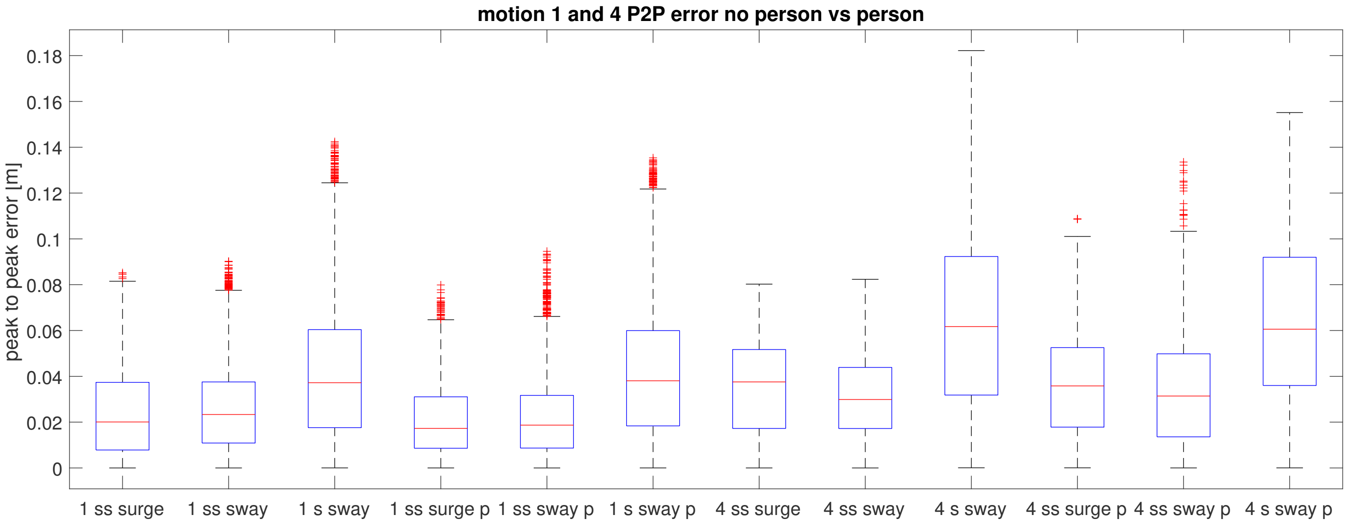

Figure 6.12: The absolute peak-to-peak error of motion 1 and 4 for the measurements with and without a person (p) obstructing the target platform. The results with a 'p' in the name are the results where a person is walking around the platform while measuring.

6.3.4. Final Results

The delay found between the encoder of the test setup and the measured motion by the LRU is investigated with the results of the proposed sled position method using the LRF. Motion 1 and 4 in sway direction are used for this comparison. In figure 4.15c the encoder data of the test setup is shown together with the data of the LRF as encoder and the result of matching with the ICP algorithm.

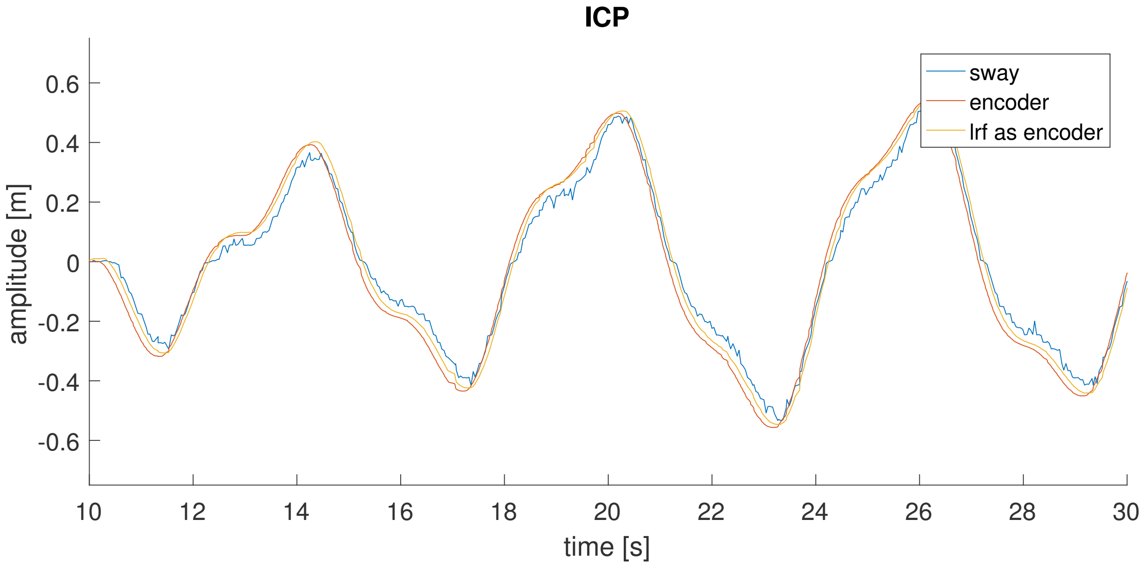

Figure 6.13: The encoder data of the test setup for motion 4 compared to the output of the ICP matching algorithm and the LRF used to determine the sled position. The sled position determined by the LRF is closer to the output of the ICP matching algorithm

The position of the sled using the LRF measurement shows a better result to the motion described by the ICP algorithm after matching. The motion upwards (from a negative to positive sled position) shows a small delay decrease between the encoder position of the sled and the LRF measured position of the sled. The motion downwards shows a larger delay decrease between the encoder and the LRF. This supports the assumption that some of the delay is caused by stretching of the toothed belt. the length of the the toothed belt from sled to the actuator differs per direction, resulting in a longer or shorter path able to stretch. Using the LRF for the position measurement also takes away the measurement delay caused by the data logging construction using multiple ports over Ethernet in combination with Matlab. The output motion of the LRU compared to the sled position measured with the LRF is shown in figure 6.14. the absolute peak-to-peak error for both motions using the two sled position measuring techniques is shown in figure 6.15.

The error has shrunk to a maximum of 10 cm as final result of the LRU. the third quartile even meets the favoured accuracy of 5 cm. Being able to determine the translations of the vessel located $\approx$ 8.5 m away of the target platform, within a accuracy 10 cm while moving $\approx$1.4 m without drift over time is a great result knowing that the error of the Octans for this motion would be %5 of 1.4 m is 7 cm.

6.3.5. Algorithm Compute Time

The LRU should be able to output the measured motions in real time. The computational time required by the algorithm was timed for all the tested motions. This resulted in a mean computation time per algorithm cycle with a new LRF measurement of 12 ms. This is fast enough for the LRU and would be even faster if the algorithm is written in C instead of Matlab.

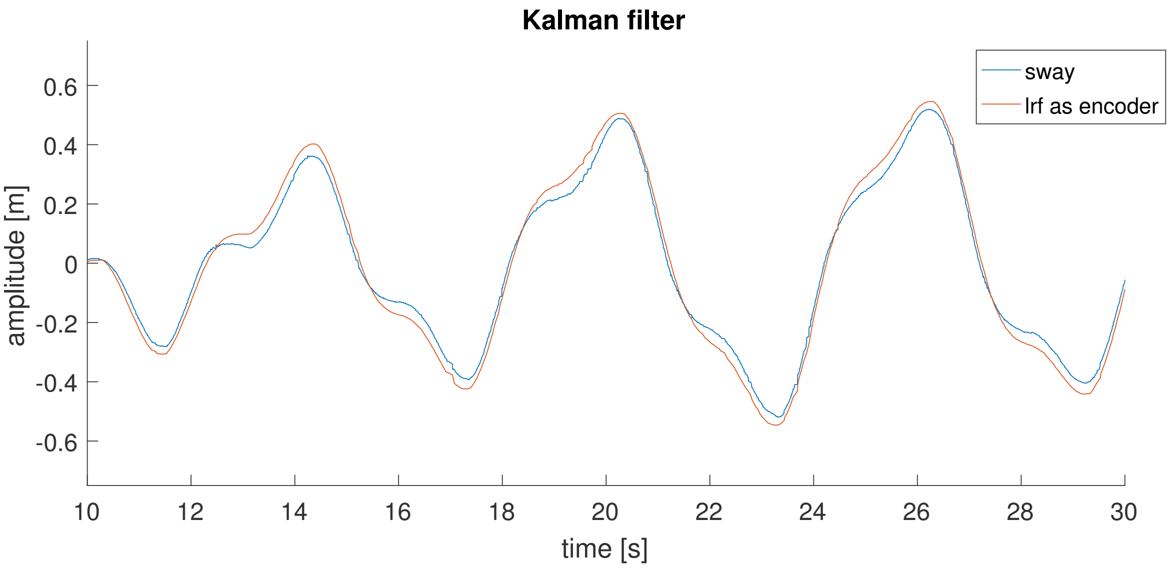

Figure 6.14: The measured output motion of the LRU compared to the position of the sled determined by the LRF. Motion 4 in sway direction is used during this test.

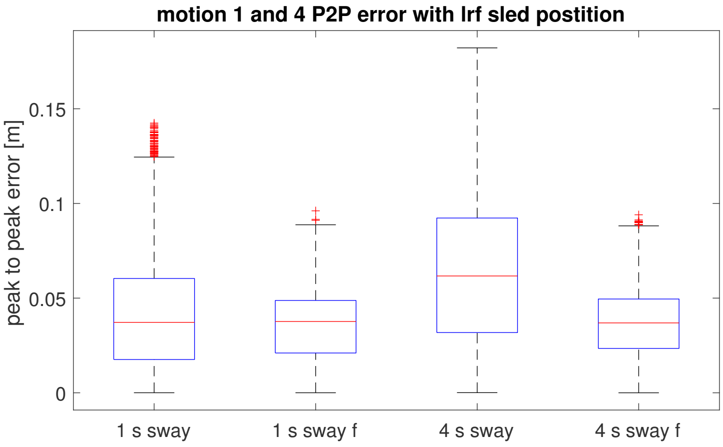

Figure 6.15: Comparison in absolute peak-to-peak error for motion 1 and 4 in sway direction computed with the test setup encoder and the LRF to determine the position of the sled. The final result where the position of the sled is determined with the LRF is indicated with a (f).

7

Conclusions & Recommendations

This thesis research presents the design and testing of a new vessel motion sensing system during people transfer operation, called the LRU, for the Ampelmann L-Type V4 system. The LRU combines measurement data of a reference distance measurement from the vessel to the platform by means of a scanning Laser Range Finder (LRF) and a micro-electromechanical Inertial Measurement Unit (IMU). The IMU enables fast motion measurement output of the LRU. The measurement output of the IMU is noisy and position measurement based on the IMU data alone would be inaccurate and suffer from drift over time. The LRF measurement data is more accurate and does not drift over time but the measurement rate combined with the position extraction algorithm is to slow to be used as a stand alone replacement of the current MRU. The measurement data of the two sensors is combined with a Kalman filter, this results in accurate and fast vessel motion sensing.

The conclusion regarding the goal of this research are summarized in this section. At last recommendations for future work are made.

7.1. Conclusions

- The proposed LRU, consisting of two scanning LRF's and a micro-electromechanical IMU is able to accurately measure the vessel position during people transfer operation. The absolute peak-to-peak error of the translational vessel motions stays below 10 cm while the vessel is moving at a distance from the target platform within the working range during the transfer operation.

- The RANSAC algorithm used to detect landmarks from the point cloud measurement data of the LRF successfully detects arcs and lines. The landmark detection avoids measurement data of unwanted moving people on the target platform removing these points form the point cloud used for matching. The landmark detection also filters out unwanted scan points of small details of the target platform that are not scanned in every consecutive scan.

- The combination of the LRF and IMU sensors fusion results in a high measurement output rate while remaining accurate. The time a measurement update of the LRF algorithm takes is 12 ms, resulting in a algorithm for position and motion extraction for online use.

- Due to the absolute reference measurement from the vessel to the target platform the LRU does not experience drift over time like the current vessel motion sensing used by Ampelmann does.

- The LRU measures its location with regard to the target platform. This target position information can be used in future innovations of the Ampelmann system. Some examples are: The tip force exerted by the actuator of the gangway can be controlled. Automatic landing of the gangway onto the target platform with minimal operator input can be achieved. The LRU could also assist the captain of the vessel to put and keep the vessel in the right place during people transfer operation.

- The LRU can be used to measure all 6 DoF of the vessel motions. The yaw and pitch rotations are measured with the LRF scan measurements in both planes. The ICP matching algorithm already extracts theses rotations and no further adjustments to the ICP algorithm is required. The IMU already measures the pitch and yaw angle. Only additions to the Kalman filter are required to implement the rotations in the vectors and model matrices.

Regarding the goal of this thesis project stated in chapter 1, the following conclusion can be drawn: *A measurement system is developed which is able to measure vessel motions during transfer operation of the Ampelmann system. The test results show a accurate and robust vessel motion measurement system that measures the target position with respect to the vessel. The new system results in less then* %20 *of the cost compared to the current vessel motion sensing system and has the added benefit to enable future innovations. The proposed MRU does not experience drift by measuring with the target platform as a reference.*

7.2. Recommendations

The proposed absolute reference vessel motion measurement system shows promising results. Before the system can be used in a real people transfer operation the following recommendations should be considered and further improvements could be made:

- The on-chip sensor fusion of the BNO055 IMU caused unwanted delays on the output measurement data. Using the raw data of the accelerometer and gyroscope during testing did not show any problems concerning measurement output delay. To measure the angular orientation and the linear accelerations, an off-chip sensor fusion algorithm should be implemented in the LRU algorithm.
- The quality of a match with the ICP algorithm varies largely when landmarks disappear. The output result of the ICP algorithm is based on the centroid of the point cloud. Due to the changed centroid position of the measurement scan when a landmark disappears, compared to the reference point cloud centroid, a large translational displacement will be the output result of the ICP algorithm. Currently these measurements are discarded and the Kalman filter predicts the motion of the vessel until a good match is made. If only the landmarks found in the measurement scan where used in the reference during ICP matching the output of the ICP algorithm will be correct. A solution that would group the corresponding landmarks of all the consecutive scans can be thought of and implemented.
- Extra tests are required to determine the roll measurement performance of the LRU. Offshore testing is required to test the performance of the measurement system during various sea and weather conditions. Before the system is used one should know what the influence of these offshore conditions are on the system, for example sea water spray due to high velocity winds.
- To further reduce the cost of the LRU a optical system could be designed where half of the total scan angle of the LRF is used for the horizontal scan plane and the other half is deflected in a vertical scan plane. Such a system would require a single LRF only.

Bibliography

[1] M.C. Amann, T. Bosch, M. Lescure, R. Myllyla, and M. Rioux. Laser ranging: a critical review of usual techniques for distance measurement. *Optical Engineering*, 40(1):10–19, 2001.

[2] P. Bergström and O. Edlund. Robust registration of point sets using iteratively reweighted least squares. *Comput Optim Appl*, 58:543–561, 2014.

[3] P. Bergström, O. Edlund, and I. Söderkvist. Repeated surface registration for on-line use. *The International Journal of Advanced Manufacturing Technology*, 54(5-8):677–689, may 2011.

[4] Bosch. BNO055 Datasheet, 2015.

[5] F. Caron, E. Duflos, D. Pomorski, and P. Vanheeghe. GPS/IMU data fusion using multisensor Kalman filtering: introduction of contextual aspects. *Elsevier: Information Fusion*, 7:221–230, 2006.

[6] D.J. Cerda Salzmann. *Development of the Access System for Offshore Wind Turbines Thesis*. Delft University of Technology, 2010.

[7] F. Colas and L. Oswald. Studies on Mechatronics Recent development of the Iterative Closest Point algorithm An overview of the years 2008 to 2010. *Tesis, Autonomous Systems Lab, ETH Zürich*, 2010.

[8] Level Developments. HPS-30 Datasheet, .

[9] Level Developments. LCH-A-S Datasheet, .

[10] Level Developments. MAS-360-HA Datasheet, .

[11] Level Developments. SOLAR-30 Datasheet, .

[12] C. Glennie and D Lichti. Static Calibration and Analysis of the Velodyne HDL-64E S2 for High Accuracy Mobile Scanning. *Remote Sensing*, 2(6):1610–1624, jun 2010.

[13] GY-85. MPU-6000 and MPU-6050 Product Specification, 2011.

[14] A. Harrison and P. Newman. High quality 3D laser ranging under general vehicle motion. *2008 IEEE International Conference on Robotics and Automation*, pages 7–12, 2008.

[15] B. Huhle, T. Schairer, A. Schilling, and W. Straßer. 6DoF registration of 2D laser scans. *Proceedings - 2011 International Conference on 3D Imaging, Modeling, Processing, Visualization and Transmission, 3DIMPVT 2011*, pages 148–155, 2011.

[16] IXblue. ixblue product sheet Octans gen v 03-2016, 2016.

[17] Darko Juric. Object Tracking: Kalman Filter with Ease. *Faculty of Electrical Engineering and Computing, University of Zagreb*, 2015.

[18] H.Y. Kim, S.O. Lee, and B.J. You. Robust laser scan matching in dynamic environments. *2009 IEEE International Conference on Robotics and Biomimetics, ROBIO 2009*, pages 2284–2289, 2009.

[19] Kongsberg. MRU2 Datasheet, 2014.

[20] J Kosecka. Model Fitting , RANSAC Fitting. *George Mason University Lecture Notes*, 2014.

[21] LORD. 3DM-GQ4-45 Datasheet, .

[22] LORD. 3Dm-GX3-25 Datasheet, .

[23] R Myllyla, J. Marszalec, J. Kostamovaara, A. Mantyniemi, and G.J. Ulbrich. Imaging distance measurements using TOF lidar. *Journal of Optics-Nouvelle Revue D Optique*, 29(3):188–193, jun 1998.

[24] V. Nguyen, A. Martinelli, N. Tomatis, and R. Siegwart. A Comparison of Line Extraction Algorithms using 2D Laser Range nder for Indoor Mobile Robotics. *Autonomous Systems Laboratory Ecole Polytechnique F´ erale de Lausanne*, 2005.

[25] J.C. Noyer, R. Lherbier, and B. Fortin. Automatic feature extraction in laser rangefinder data using geometric invariance. *Conference Record - Asilomar Conference on Signals, Systems and Computers*, (4):199–203, 2010.

[26] K.E. Peiponen, R. Myllyla, and A.V. Priezzhev. *Optical Measurement Techniques*. Springer, 4 edition, 2009.

[27] Søren Riisgaard and Morten Rufus Blas. SLAM for Dummies. *A Tutorial Approach to Simultaneous Localization and Mapping*, 22(June):1–127, 2004.

[28] A.M. Sabatini and V. Genovese. A sensor fusion method for tracking vertical velocity and height based on inertial and barometric altimeter measurements. *Sensors (Basel, Switzerland)*, 14(8): 13324–13347, 2014.

[29] Scanse. Sweep Datasheet, 2016.

[30] R.M. Schmidt, G. Schitter, A. Rankers, and J. van Eijk. *High Performance Mechatronics*. IOS Press, 2nd edition, 2014.

[31] R. Schnabel, R. Wahl, and R. Klein. Efficient RANSAC for point-cloud shape detection. *Computer Graphics Forum*, 26(2):214–226, 2007.

[32] SICK. LMS5xx Laser Measurement Technology Product Information, 2012.

[33] SICK. LD-MRS Datasheet, 2014.

[34] SignalQuest. SQ-GIX-0200 Datasheet, 2014.

[35] O. Sorkine-Hornung and M. Rabinovich. Least-Squares Rigid Motion Using SVD. *Department of Computer Science, ETH Zurich*, 2017.

[36] James Stewart. *Calculus: early transcendentals*. Thomson, Brooks/Cole, 6th edition, 2008.

[37] X-io Technologies. x-IMU Datasheet, 2013.

[38] S. Thrun, W. Burgard, and D. Fox. *Probabilistic robotics*, volume 1. MIT Press, 2005.

[39] VectorNav. VN-100 Datasheet.

[40] Velodyne. PUCK Datasheet, .

[41] Velodyne. HDL-32E Datasheet, .

[42] Velodyne. HDL-64E Datasheet, .

[43] AG Verweij. Markerless Position Measurement, Thesis. *Delft University of Technology*, (November), 2014.

[44] G. Welch and G. Bishop. An Introduction to the Kalman Filter. *University of North Carolina*, 2006.

[45] O. Wulf and B. Wagner. Fast 3D scanning methods for laser measurement systems. *University of Hannover*, 2003.

[46] J. Xavier, M. Pacheco, D. Castro, A. Ruano, and U. Nunes. Fast Line, Arc/Circle and Leg Detection from Laser Scan Data in a Player Driver. In *Proceedings of the 2005 IEEE International Conference on Robotics and Automation*, pages 3930–3935. IEEE, 2005.

List of Acronyms

2D 2-Dimensional. 14, 23, 30, 35

3D 3-Dimensional. 11, 14, 31, 51

AMPA Asian Marine Professionals. 37, 76

AWESOME Ampelmann Workability Evaluation of ship Orientated Motions and Cylinder Excitations. 16, 17, 59

CoG Centre of Gravity. 16

CVFSAC Corresponding Vector Fitting SAmpling Concensus. 32–34, 76

DoF Degrees of Freedom. iii, 1, 2, 7, 11, 12, 15–17, 22, 23, 25, 55, 62, 70

EIF Extended Information Form. 14, 34

EKF Extended Kalman Filter. 34

FCS Fast Crew Supplier. 15–17, 19, 59–61, 75, 77, 78, 82

FIM Fast Incremental Mapping. 14, 34

HPU Hydrolic Power Unit. 3

IAV Inscribed Angle Variance. 31

ICP Iterative Closest Point. iii, 14, 32–34, 40–43, 47, 49, 59, 63, 66, 70, 76–78, 84–86

IMU Inertial Measurement Unit. iii, viii, 14, 21, 25, 26, 34, 35, 45–48, 51–56, 61, 62, 64, 69, 70, 76–79, 83

LiDAR Light Detection And Ranging. iii, 5

LRF Laser Range Finder. iii, vii, viii, 1, 2, 5–9, 11–14, 18, 21–25, 29–32, 35, 36, 39, 40, 42, 43, 45, 47, 48, 51–53, 55–57, 59, 62, 64, 66, 67, 69, 70, 75–79, 86

LRU LiDAR Reference Unit. iii, 13–15, 19, 21–25, 30–32, 34, 35, 38, 39, 43, 47, 50, 51, 53, 55, 59, 60, 62–67, 69, 70, 75–79

MEMS Micro-Electro-Mechanical Systems. 14, 25

MRU Motion Reference Unit. iii, vii, 1, 12–15, 17, 18, 50, 63, 69, 70, 78, 83–85

PLC Programmable Logic Controller. 3, 5, 30, 55, 56

PSD Power Specrtal Density. 16, 17, 61, 75

RANSAC RANdom SAmple Consesnsus. iii, 14, 30–32, 37–41, 49, 64, 65, 69, 76

RAO Response Amplitude Operator. 16, 17

S2S Ship to Ship. 4, 5, 9, 13

SEIF Sparse Extended Information Filter. 14, 34

SLAM Simultaneous Localization and Mappaing. 14, 29, 30, 34

SVD Singular Value Decomposition. 14, 41–43, 76

TCP Transmission Control Protocol. 35, 64

ToF Time of Flight. 6, 8, 13

UDP User Datagram Protocol. 56, 64

List of Figures

1.1 The Ampelmann system used to safely transfer people from a vessel to a offshore windmill. 1
1.2 The Ampelmann E-Type System. 2
1.3 The six DoF's of a floating vessel. 3
1.4 The Octans fibre optic gyroscope six DoF's motion sensor. 3
1.5 Ampelmann Control Model [43]. 4
1.6 Cargo and lifting additions for the Ampelmann system. 4
1.7 The controllable motions of the Gangway. 5
1.8 Block diagram of a time of flight laser range finder. 6
1.9 Schematic setup of a 1-dimensional measurement. 7
1.10 Schematic setup of a 2-dimensional measurement. 7
1.11 Schematic setup of a 3-dimensional measurement. 7
1.12 time jitter. 8
1.13 Walk. 8
1.14 Data processing pipe-line [43]. 9
1.15 The point of two scans are used to create a histogram to find the translations with the use of a cross correlation. 10
1.16 Rotation an translation optimization algorithm [43]. 10
1.17 A Measuring setup to extract Heave, Sway and Roll motions with a single LRF shown from different angels. 11
1.18 A Measuring setup to extract Heave, Sway, Surge, Yaw, Pitch and Roll motions with a single rotating LRF shown from different angels. 12

2.1 Example setup of the Ampelmann L-type V4 concept transfer operation is done from the stern of the vessel.. 15
2.2 The controllable angles and translation with their mechanical limit's on the L-type V4 concept. 16
2.3 Water surface elevation with 90° impact angle with respect to the vessel and the corresponding frequency's in a PSD. 17
2.4 Examples of a small and large offshore FCS vessel. 17
2.5 Simulated vessel motion. 18
2.6 Vessel PSD. 19
2.7 The normal landing procedure for small FCS vessels for people transfer. 19

3.1 Placement positions for the LRU on the vessel/gangway. 21
3.2 Noise makes it impossible to correctly describe a scanned line with only two points [43]. 22
3.3 Simple example to determine the required resolution of the LRF. 23
3.4 The maximum possible scan angle for the SICK LMS 511 Pro, dark red illustrates a scan range up to 40 m for 10% remission factor and dark red illustrates the maximum range of 80 m. [32] 24
3.5 The SICK LMS 511 PRO can measure up to five echo's making the laser measurement less dependent on weather conditions [32]. 25
3.6 2D example of three scanner orientations: horizontal, vertical and diagonal scan orientations. The red lines indicate the scan lines and the red arrow indicate the motions on the x, y-axis of the different orientations. 26

4.1 Process approach for an algorithm to go from a point cloud to motion measurement, using computer vision. 29

4.2 The RANSAC algorithm illustrated. the initial point cloud is illustrated in (a), two points are randomly selected in (b) a line is drawn through these points and the distance from this line to the other points is computed, below a set limit these points become inlier's in (c). If the line consists of enough inlier's the line is recomputed using the inlier's. In (d) and (e) two different points are selected resulting in the correct line detection. 30

4.3 inscribed angles, with respect to the extremes(P_1, P_4), of an arc are congruent [46]. . . . 31

4.4 The grid matching algorithm. The reference point cloud in red and the scan to be matched in blue. 32

4.5 The ICP algorithm [7]. 32

4.6 The CVFSAC algorithm [18] 33

4.7 An overview based on different research done in the field of point cloud localization and mapping. The chosen algorithm items for the LRU are represented with a thick border/line. 35

4.8 Point Cloud of a pillar with a wall in the background scanned with the SICK LMS 511 from a distance of 10 m. The Scanner is scanning in the horizontal plane and is placed in the origin $(0, 0)$ which is not shown in this plot. 36

4.9 Illustration of a bounding box on the point cloud of a pillar with a wall in the background. In (a) the bounding box is shown in the original plot and in (b) the resulting point cloud,after discarding the points outside the bounding box 36

4.10 Pictures of platforms in the offshore fields of AMPA taken from a vessel with the older L-Type V3 on-board. (a) a cluster of platforms, (b) a close by picture off the people transfer landing point. 37

4.11 RANSAC line algorithm result on the bounded point cloud of a pillar with a wall in the background. 38

4.12 RANSAC arc algorithm result on the bounded point cloud of a pillar with a wall in the background. 41

4.13 A scan by the LRF of a pillar from a distance of 2.2 m to the centre of the pillar. The red lines indicate the maximum line of sight of the LRF on part of the pillar. 42

4.14 Illustration of the single value decomposition on a unit disk. The upper left shows the unit disc in blue together with the two canonical unit vectors. The upper right shows the action of M on the unit disc: it distorts the circle to an ellipse. The SVD decomposes M into three simple transformations: a rotation V^*, a scaling Σ along the coordinate axes and a second rotation U. The SVD reveals the lengths σ_1 respectively σ_2 of the semi-major axis respectively semi-minor axis of the ellipse; they are just the singular values which occur as diagonal elements of the scaling Σ. The rotation of the ellipse with respect to the coordinate axes is given by U [1]. 43

4.15 Iterative closest point algorithm on the example pillar point cloud. The pts_{scan} point cloud is rotated by $10°$counter clockwise around the centroid and translated 0.5 m in the positive x and y direction. In (a) the nearest neighbours in the first iteration step are computed. In (b) the result of the first iteration step transformation are shown. In (c) the final result after matching and transforming is shown, the transformed points lay on top of the reference points. 44

4.16 What the Kalman filter does is propagating and updating Gaussian's and updating their covariances. First the next state is predicted from the provided state transition, then the (noisy) measurement information is incorporated in the correction phase 45

4.17 Operation overview of the Kalman filter. The filter requires the initial estimates and measurement data at each time step to update. The filter outputs the updated state estimate and error covariance. 46

4.18 The Kalman filter in action on simulated sine motion with an amplitude of 0.69 m with a frequency of 0.2 Hz. With added Gaussian noiseon the acceleration and LRF position data. The simulated LRF data is updated with a frequency of 25 Hz the Kalman filter and simulated IMU data predict at a frequency of 100 Hz. In (a) the motion is showed for a duration of 30 s, in (b) a zoomed view of the first 10 s is shown. 48

5.1 A scan of the simulation model. The target consist of three horizontal and three vertical cylinders at a distance of 12 m from the LRF scanners. The input motion that the LRF is following during the simulation is plotted around the origin. The intersection points of the scan are highlighted in the figure with *. The scan lines continue outside the box of the plot, this is not shown in the figure. 52
5.2 The point cloud of single pillar created by the LRF simulation. 52
5.3 The accelerations measured by the BNO055 IMU while laying still for 60 s. Only the first 10 s are shown. 53
5.4 The simulated sway accelerations compared to the measured sway accelerations by the BNO055 IMU while laying still for 10 s. 53
5.5 The measured Euler angles by the BNO055 IMU while laying still for 60 s. 53
5.6 Dead reckoning using only the noise levels of the three directions acceleration measurement data of the BNO055 while laying still. 54
5.7 A swing for rotational testing of the IMU Euler angle results. In (a) the swing is in rest, in (b) the IMU is swinging. 54
5.8 A swing for rotational testing of the IMU Euler angle results. In (a) the swing is in rest, in (b) the IMU is swinging. 55
5.9 Illustration of the translational motion test setup. All the required parts of the setup are pointed out in the figure. 56
5.10 The user input sled control panel of the test setup and the corresponding state machine. (a) The sled control panel is used to sent commands to the measurement setup to switch between the states. (b) The state machines shows the different state of the test setup and the possible ways to get from one state to another. 57
5.11 The control loop of the translational test setup. The input motion or reference is supplied by a position $r(t)$ and velocity $\dot{r}(t)$. The velocity is used in as feed-forward control for the plant. The reference position $r(t)$ is used in a proportional gain feed-back loop. The plant consist of a current controlled frequency drive connected to a electric AC motor. The motor is connected to a gearbox slowing the rotations with a factor 9. Connected to the gearbox is the toothed wheel driving the belt connected to the sled. The encoder used in the feed-back loop is connected to the axle of the toothed wheel. 57
5.12 The complete measurement test setup (a) with the sensors on top of the sled platform. (b) the test setup with the target platform at a distance of ≈8.5 m. 58

6.1 The result after matching of the simulation model of the Damen FCS vessel motion from $t = 35$s till $t = 50$s. 60
6.2 The result of the LRU simulation model of the Damen FCS vessel motion from $t = 35$s till $t = 50$s. 60
6.3 meaning of the box-plot parts [43]. 60
6.4 The absolute peak-to-peak translation errors of the simulation model of the Damen FCS vessel motions and a sine motion. 61
6.5 The roll angle measured with the BNO055 while swinging on the test setup. The amplitude is as expected decreasing over time. The frequency of the motion is f =0.321 Hz and complies with the expected frequency according to the design of the swing. 61
6.6 A closer look, from $t = 200$s till $t = 220$s of the roll angle from figure 6.5, reveals a unexpected motion profile, while the angular velocity shows the expected motion profile. 62
6.7 The absolute peak-to-peak (P2P) error of the test measurement motions compared in a box-plot. The different motions from table 6.2 illustrate the performance of the LRU. . . 63
6.8 The output after the ICP matching algorithm of motion 4 in sway direction. A delay due to the communication buffer or flexibility of the toothed belt of the test setup is clearly visible. 63
6.9 The output of the LRU of motion 4 in sway direction. A delay due to communication buffer or flexibility of the toothed belt of the test setup is clearly visible. 64
6.10 test setup approach to use the LRF as a position sensor while still scanning the target. A plate is added perpendicular to the rail and the scan angle of the LRF is increased to scan the plate and the target at the same time. 64

6.11 A plot of the point cloud of all measured scan points of motion 4 in sway direction with and without obstruction. In (a) there is no person walking around the target platform during measuring while in (b) a person is walking around while measuring. 65
6.12 The absolute peak-to-peak error of motion 1 and 4 for the measurements with and without a person (p) obstructing the target platform. The results with a 'p' in the name are the results where a person is walking around the platform while measuring. 65
6.13 The encoder data of the test setup for motion 4 compared to the output of the ICP matching algorithm and the LRF used to determine the sled position. The sled position determined by the LRF is closer to the output of the ICP matching algorithm 66
6.14 The measured output motion of the LRU compared to the position of the sled determined by the LRF. Motion 4 in sway direction is used during this test. 67
6.15 Comparison in absolute peak-to-peak error for motion 1 and 4 in sway direction computed with the test setup encoder and the LRF to determine the position of the sled. The final result where the position of the sled is determined with the LRF is indicated with a (f). 67

A.1 The peak-to-peak error of the damen FCS vessel motion in the simulation model. 82
A.2 The full 100 s simulation model output and input of the Damen FCS input motion. 82
A.3 The swing test is done with changing cercomstances. The weight of the IMU platform is shifted and the start angle is changed. 83
A.4 Motion 1 ICP surge and sway output. 84
A.5 Motion 1 MRU surge and sway output. 84
A.6 Motion 1 sway new ICP output. 84
A.7 Motion 1 sway new MRU output. 85
A.8 Motion 4 sway ICP output with obstruction by person walking around the platform . Clear mismatches due to blocking of the landmarks are visible. 85
A.9 Motion 4 sway new MRU output. The mismatched data of the ICP algorithm is discarded and the Kalman filter predicts the motion at these points. 85
A.10 Motion 4 sway without person ICP output. The disparaging of landmarks is not only caused when a person blocks the field of view of the LRF. 86
A.11 Motion 1 sway without person ICP output. The disparaging of landmarks is not only caused when a person blocks the field of view of the LRF. The Kalman filter solves most of the mismatches. 86

List of Tables

1.1 Ampelmann systems . . . 3

2.1 iXblue Octans Motion Sensor Specifications [16] . . . 18
2.2 specifications . . . 19

3.1 LRF specifications . . . 24
3.2 LMS 511 PRO LRF specifications [32] . . . 25
3.3 overview of roll sensor specifications. . . . 27

4.1 All user defined algorithm settings used during simulation and testing. . . . 49

5.1 IMU noise levels during simulation . . . 54
5.2 Parts used to create translational test setup. . . . 58

6.1 Components of the simulated sinusoidal input motion for the LRU simulation model. . . . 59
6.2 Names of the motions and their components used during the translational tests. the complete motion used as the reference motion of the sled is the summation of all the components listed per motion. . . . 63

A

Appendix

To reduce paper and add digital media sources some of the content of the appendix is provided in the cloud. A link to the specific folder is provided per section of the appendix. To gain access more easily to the complete cloud stored appen appendix use the following link an password:

`http://stenpas.nl/thesisappendix`

Password: GiantLaser2017

Please keep in mind that this research is marked confidential till 09-05-2022, don't share this link and password with anyone that is not granted access to this document.

A.1. Algorithm code MATLAB

To save the world by printing less paper the m-files of the algorithm m-files can be found online at:

`https://server.stenpas.nl/owncloud/index.php/s/JHtWMM5nI1H38vi`

Password: GiantLaser2017

Please keep in mind that this research is marked confidential till 09-05-2022, don't share this link and password with anyone that is not granted access to this document.

A.2. Simulation model

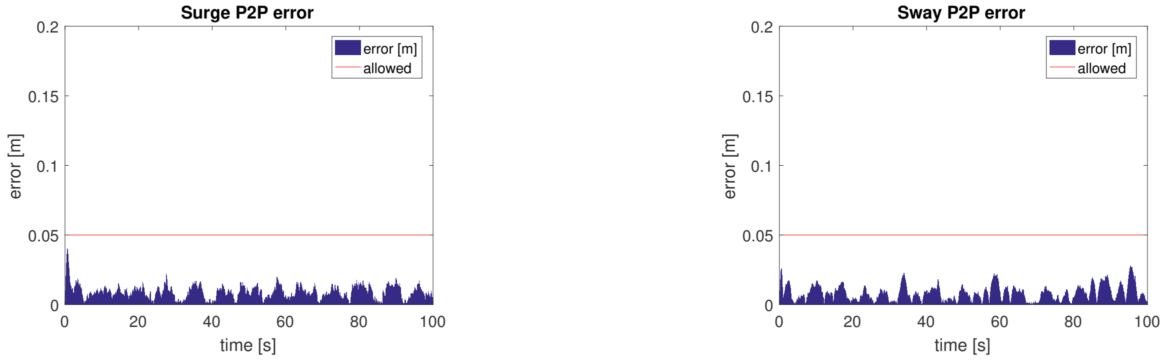

(a) Surge (b) Sway

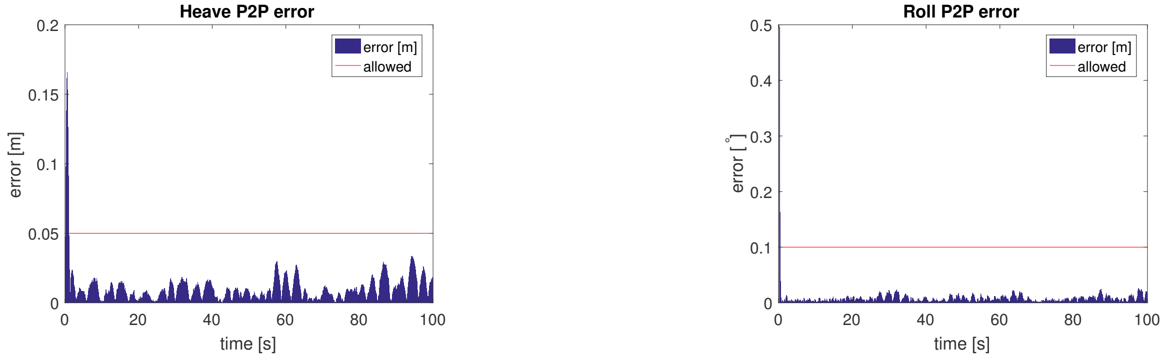

(c) Heave (d) Roll

Figure A.1: The peak-to-peak error of the damen FCS vessel motion in the simulation model.

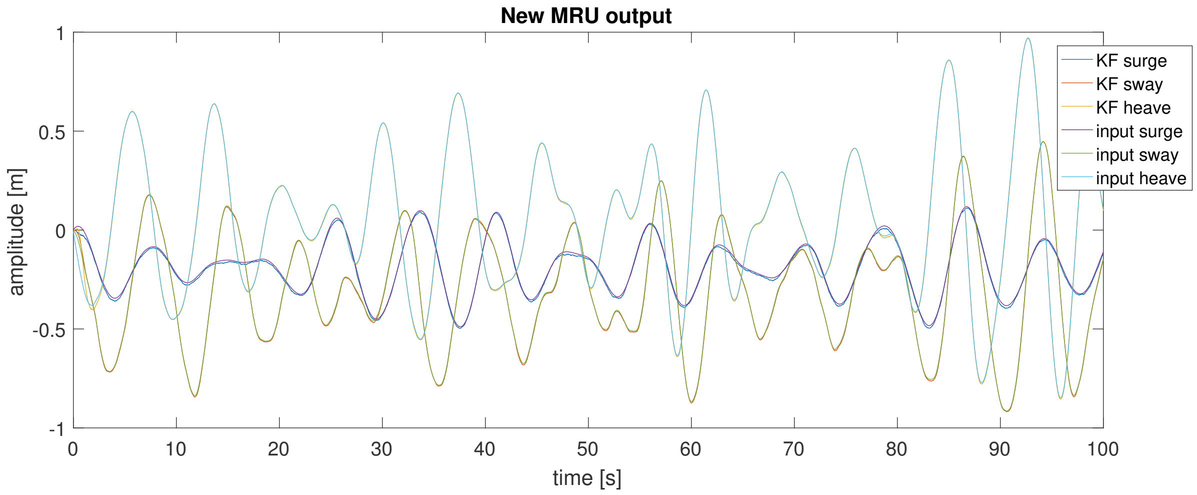

Figure A.2: The full 100 s simulation model output and input of the Damen FCS input motion.

A.3. Test Set-up

A.3.1. Rotational Swing

Different Orientations

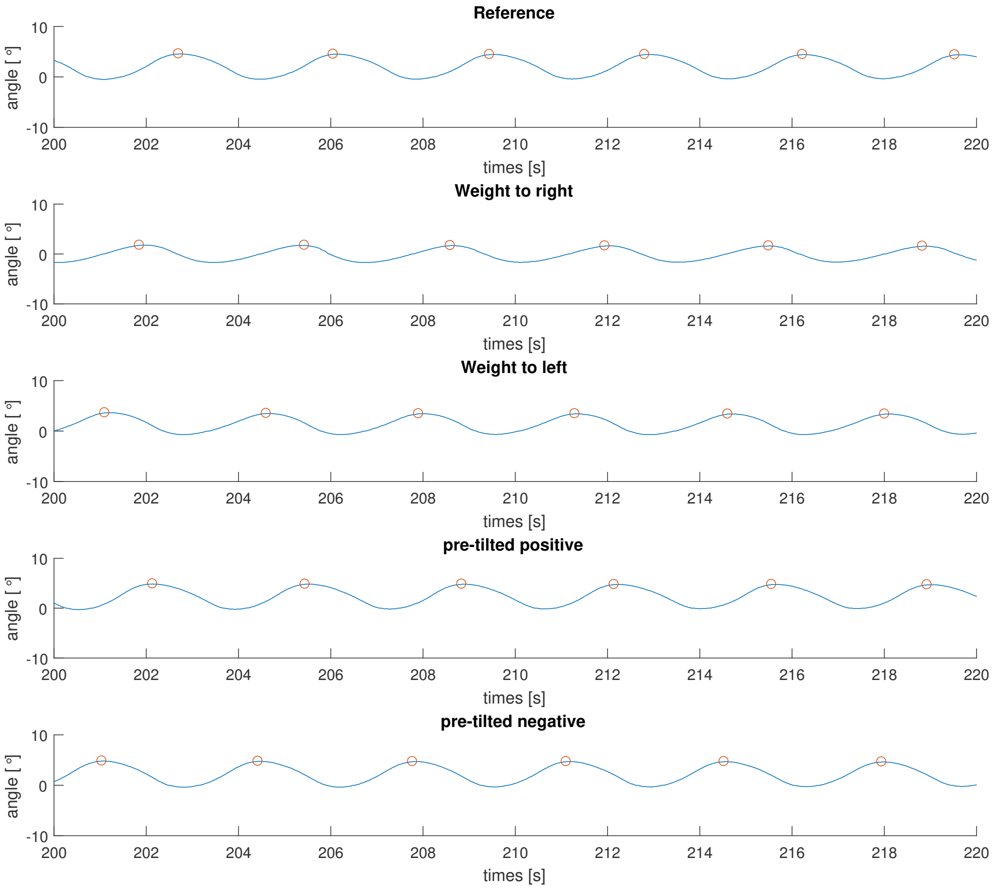

Figure A.3: The swing test is done with changing cercomstances. The weight of the IMU platform is shifted and the start angle is changed.

Testing Movies & Pictures

`https://server.stenpas.nl/owncloud/index.php/s/TyWNJbau3KL8rxd`

Password: GiantLaser2017

Please keep in mind that this research is marked confidential till 09-05-2022, don't share this link and password with anyone that is not granted access to this document.

A.3.2. Translational Sled

Testing Movies & Pictures

`https://server.stenpas.nl/owncloud/index.php/s/6AEOq5JUqA1S2Oo`

Password: GiantLaser2017

Please keep in mind that this research is marked confidential till 09-05-2022, don't share this link and password with anyone that is not granted access to this document.

Results

To get a feeling of the ouptu results of the new MRU additional full motion result plots are given here.

motion 1 surge and sway

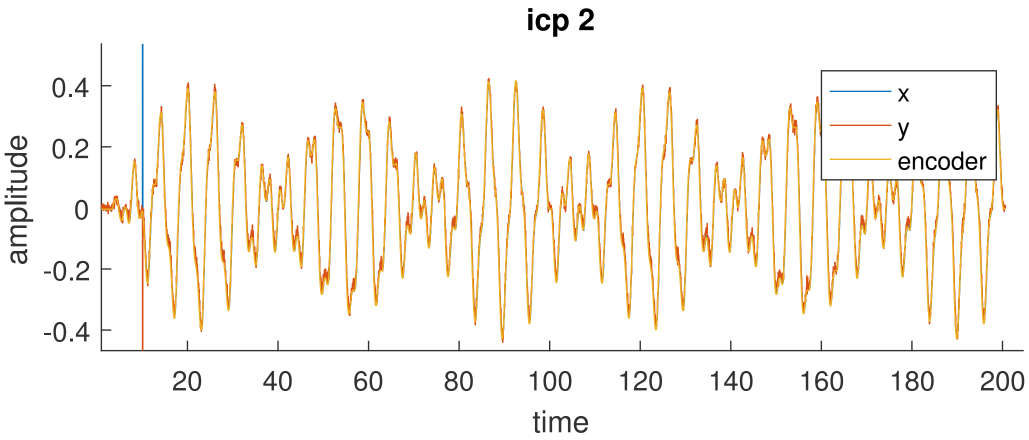

Figure A.4: Motion 1 ICP surge and sway output.

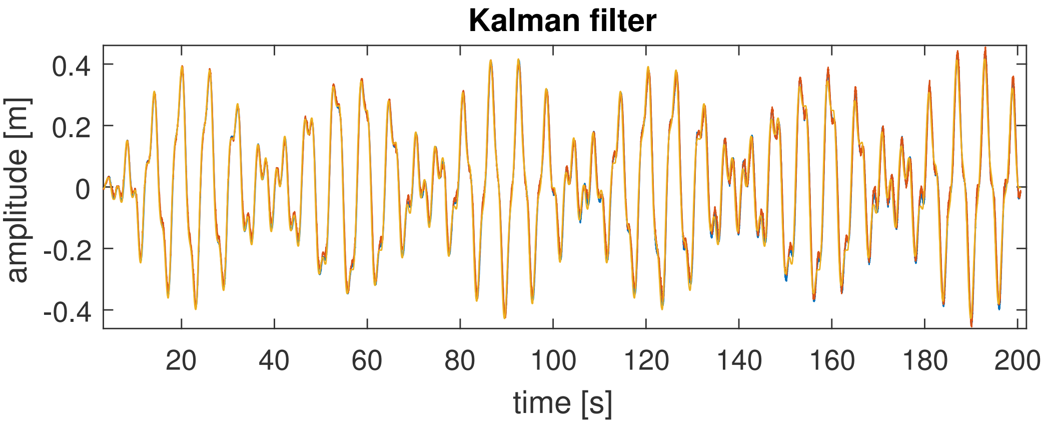

Figure A.5: Motion 1 MRU surge and sway output.

motion 1 sway

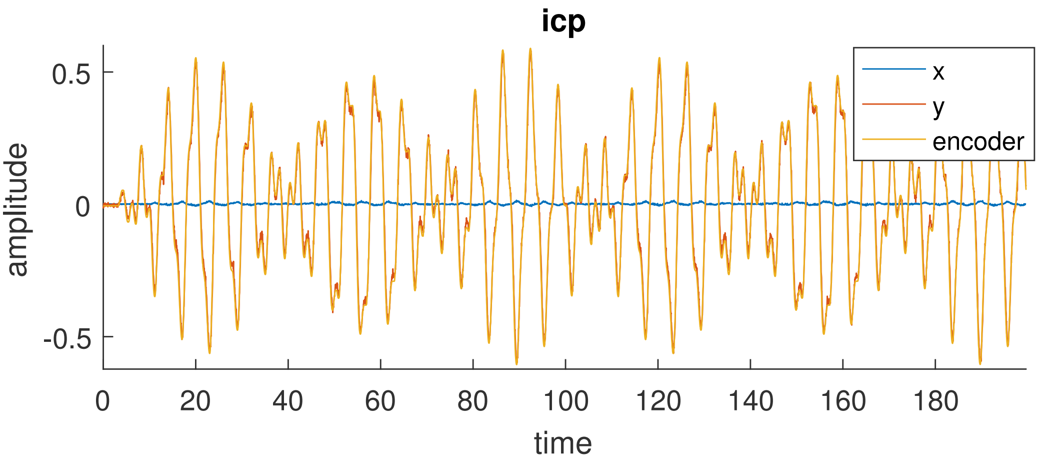

Figure A.6: Motion 1 sway new ICP output.

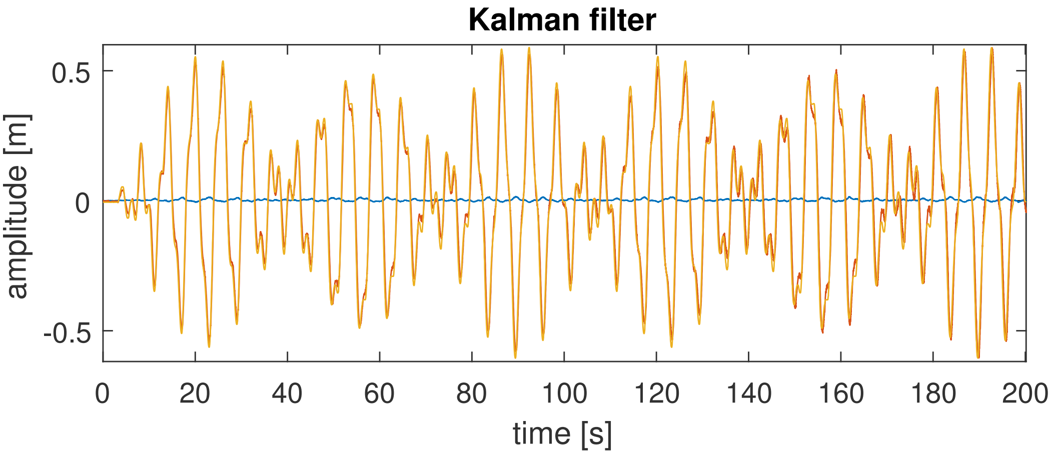

Figure A.7: Motion 1 sway new MRU output.

motion 4 sway with person

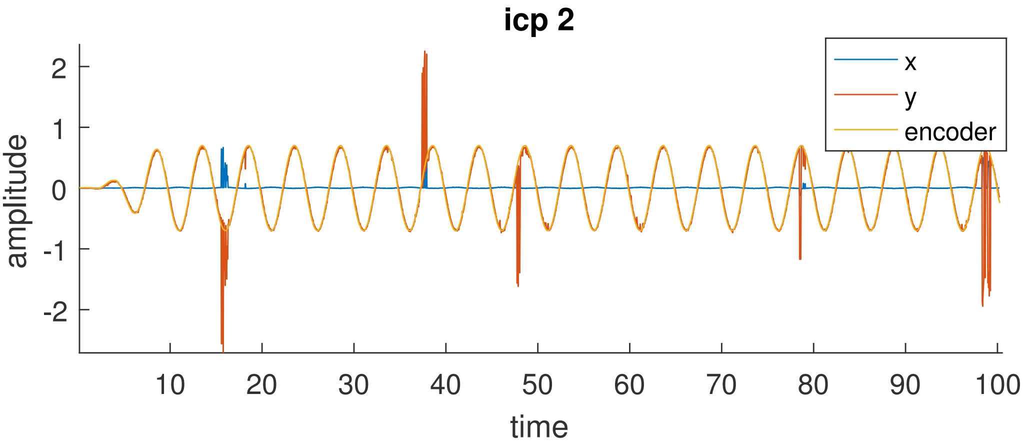

Figure A.8: Motion 4 sway ICP output with obstruction by person walking around the platform . Clear mismatches due to blocking of the landmarks are visible.

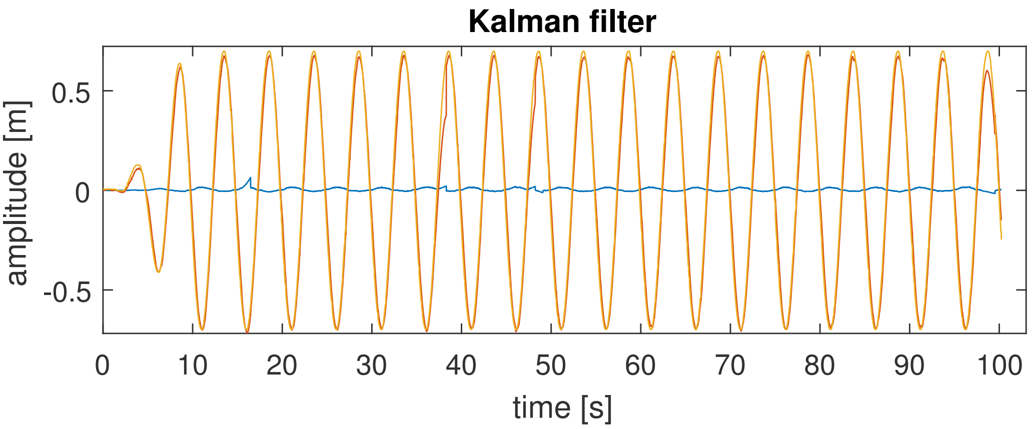

Figure A.9: Motion 4 sway new MRU output. The mismatched data of the ICP algorithm is discarded and the Kalman filter predicts the motion at these points.

motion 4 sway without person

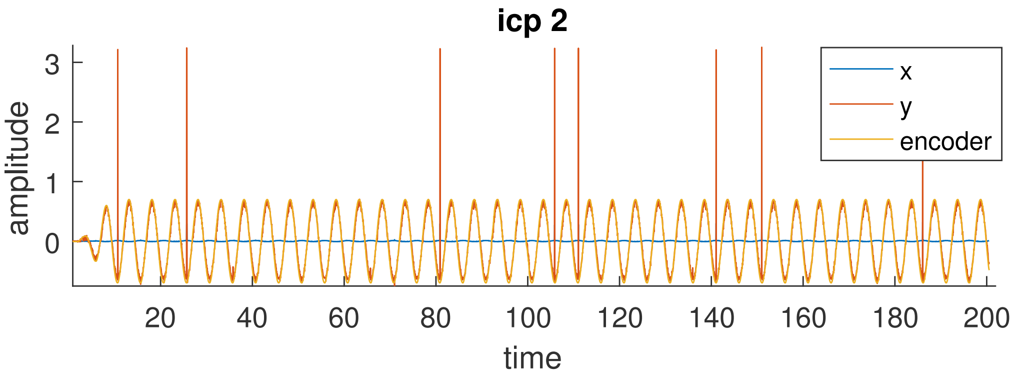

Figure A.10: Motion 4 sway without person ICP output. The disparaging of landmarks is not only caused when a person blocks the field of view of the LRF.

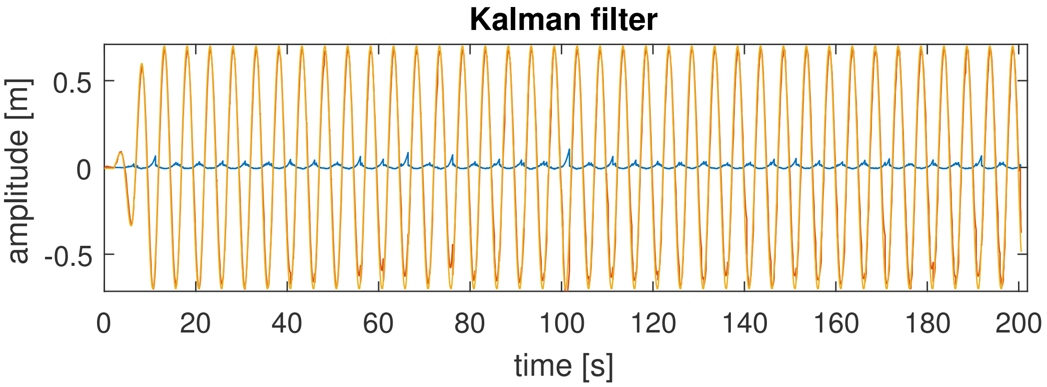

Figure A.11: Motion 1 sway without person ICP output. The disparaging of landmarks is not only caused when a person blocks the field of view of the LRF. The Kalman filter solves most of the mismatches.